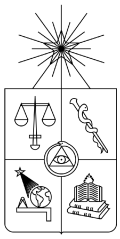

UNIVERSIDAD DE CHILE

FACULTAD DE CIENCIAS FISICAS Y MATEMATICAS

DEPARTAMENTO DE ASTRONOMIA

MOLECULAR CLOUD FRAGMENTATION AND MASSIVE STAR FORMATION IN THE GMC G345.5+1.0

TESIS PARA OPTAR AL GRADO DE DOCTOR EN CIENCIAS
MENCION ASTRONOMIA

Cristian Marcelo López Calderón

SANTIAGO DE CHILE

SEPTIEMBRE 2011

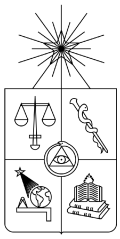

UNIVERSIDAD DE CHILE

FACULTAD DE CIENCIAS FISICAS Y MATEMATICAS

DEPARTAMENTO DE ASTRONOMIA

MOLECULAR CLOUD FRAGMENTATION AND MASSIVE STAR FORMATION IN THE GMC G345.5+1.0

TESIS PARA OPTAR AL GRADO DE DOCTOR EN CIENCIAS
MENCION ASTRONOMIA

Cristian Marcelo López Calderón

PROFESOR GUIA:
Leonardo Bronfman Aguiló

MIEMBROS DE LA COMISION:
Lars-Åke Nyman
Guido Garay Brignardello
Itziar de Gregorio-Monsalvo

SANTIAGO DE CHILE
SEPTIEMBRE 2011

Resumen

Las condensaciones masivas en nubes moleculares gigantes (GMCs) están asociadas con la formación de estrellas de alta masa, las cuales son la principal fuente de elementos pesados y radiación UV, jugando un papel importante en la evolución de las galaxias. Para estudiar este tipo de condensaciones, hicimos dos investigaciones usando observaciones hacia la GMC G345.5+1.0. Esta nube está localizada 1° de latitud sobre el plano galáctico, a una distancia de 1.8 kpc del Sol. De este modo, hay poca superposición de polvo y de estructuras moleculares a lo largo de la línea de visión, minimizando la confusión en la identificación de las condensaciones.

La primera investigación, "Formación de estrellas masivas en la GMC G345.5+1.0: Distribución espacial de la emisión del polvo", tiene como meta hacer un censo de la formación de estrellas masivas en la GMC G345.5+1.0 completa. Observamos la emisión continua a 1.2 mm de la nube completa usando el "SEST Imaging Bolometer Array" (SIMBA) montado sobre el "Swedish-ESO Submillimetre Telescope" (SEST). Las observaciones tienen una resolución espacial de 0.2 pc y cubren $1.^{\circ}8 \times 2.^{\circ}2$ en el cielo, con un ruido de 20 mJy beam^{-1}. Identificamos 201 condensaciones con un diámetro promedio de 0.3 pc, una masa promedio de 61 $M_{\odot}$, y una densidad promedio de 6×10^4 cm^{-3}. La masa total de las condensaciones es 1.2×10^4 $M_{\odot}$, así la eficiencia para formar estas condensaciones es ~0.02, estimada según la razón de la masa total de las condensaciones a la masa total de la GMC. La distribución de las masas de las condensaciones se ajusta bien por una ley de potencia $dN/dM \propto M^{-\alpha}$, con un índice espectral α igual a 1.7±0.1. Dada la distribución de sus masas, estas condensaciones no parecen ser progenitores directos de estrellas individuales. Comparando la emisión continua a 1.2 mm con imágenes infrarrojas tomadas por los satélites "Midcourse Space Experiment" (MSX) y SPITZER, encontramos que a

lo menos el ∼20% de las condensaciones están formando estrellas, y a lo más el ∼80% aun no forman estrellas. Seis regiones de formación de estrellas masivas (MSFRs), que están inmersas en condensaciones y están asociadas con fuente puntuales IRAS, tienen una densidad promedio de $\sim 10^5$ cm^{-3}, luminosidades $>10^3$ L$_\odot$ y distribuciones espectrales de energía que pueden ser modeladas con dos componentes de polvo a diferentes temperaturas. Los valores promedios de estas temperaturas son 28±5 y 200±10 K.

La segunda investigación, "G345.45+1.50: Una estructura en expansión con forma de anillo y con formación de estrellas masivas", tiene como objetivo determinar la condiciones físicas de la estructura con forma de anillo G345.45+1.50, la cual es parte de la GMC G345.5+1.0 y contiene ∼54 condensaciones de polvo con una masa promedio de 75 M$_\odot$ detectadas en la emisión continua a 1.2 mm. Observamos el anillo completo en la línea ^{13}CO(3-2) usando el telescopio "Atacama Pathfinder Experiment" (APEX). Las observaciones cubren 17′×20′ en el cielo, con una resolución angular de 18″ y una temperatura de ruido de ∼1 K a la resolución espectral de 0.1 km s^{-1}. El anillo contiene una masa total de 6.9×10^3 M$_\odot$ y se está expandiendo con una velocidad de 1.4 km s^{-1}. Estimamos un escala de tiempo de la expansión de $\sim 2.4\times10^6$ yr y una energía total de $\sim 1.4\times10^{47}$ erg. Un posible origen del anillo es la explosión de una supernova, ya que una fuente detectada a 35.5 cm, J165920-400424, está cerca del centro del anillo, a ∼90 arcsec, sin tener contraparte en el infrarrojo. En la estructura fragmentada del anillo, identificamos 57 condensaciones con un diámetros promedio de 0.6 pc, una masa promedio de 93 M$_\odot$, y una densidad promedio de 10^4 cm^{-3}. Asumiendo que las condensaciones pueden ser modeladas como esferas de Bonnor-Ebert, para estar en equilibrio hidroestático las condensaciones requieren una presión externa promedio de 7×10^6 K cm^{-3}. En la región, cinco eyecciones de materia molecular son identificadas, las cuales tienen un tamaño promedio de 2.0 pc, un gradiente promedio de rapidez proyectada de 1.7 km s^{-1} pc^{-1}, y una energía proyectada de 8×10^{45} erg. Hemos identificado fuentes infrarrojas como estrellas jóvenes candidatas para impulsar tres de las eyecciones de materia molecular.

Abstract

Massive condensations in giant molecular clouds (GMCs) are linked to the formation of high mass stars, which are the principal source of heavy elements and UV radiation, playing an important role in the evolution of galaxies.

To study these kind of condensations or clumps, we manage two research using observations toward the GMC G345.5+1.0. This cloud is located one degree above the galactic plane and at 1.8 kpc from the Sun, thus there is little superposition of dust and molecular structures along the line-of-sight, minimizing confusion effects in identifying individual clumps.

- First research, "Massive star formation in the GMC G345.5+1.0: Spatial distribution of the dust emission".
  - Aims. We attempt to make a complete census of massive-star formation within all of GMC G345.5+1.0.
  - Methods. We observed the 1.2 mm continuum emission across the whole GMC using the Swedish-ESO Submillimetre Telescope (SEST) Imaging Bolometer Array (SIMBA) mounted on the SEST. Observations have a spatial resolution of 0.2 pc and cover $1.^{\circ}8 \times 2.^{\circ}2$ in the sky with a noise of 20 mJy beam^{-1}.
  - Results. We identify 201 clumps with diameters between 0.2 and 0.6 pc, masses between 3.0 and 1.3×10^3 $M_{\odot}$, and densities between 5×10^3 and 4×10^5 cm^{-3}. The total mass of the clumps is 1.2×10^4 $M_{\odot}$, thus the efficiency in forming these clumps, estimated as the ratio of the total clump mass to the total GMC

mass, is ∼0.02. The clump mass distribution for masses between 10 and 10^3 $M_\odot$ is well-fitted by a power law dN/dM∝$M^{-\alpha}$, with a spectral mass index α of 1.7±0.1. Given their mass distribution, clumps do not appear to be the direct progenitors of single stars. Comparing the 1.2 mm continuum emission with infrared images taken by the Midcourse Space Experiment (MSX) and by the SPITZER satellite, we find that at least ∼20% of the clumps are forming stars, and at most ∼80% are starless. Six massive-star forming regions (MSFRs) embedded in clumps and associated with IRAS point sources have mean densities of $\sim 10^5$ cm^{-3}, luminosities $>10^3$ $L_\odot$, and spectral energy distributions that can be modeled with two dust components at different mean temperatures of 28±5 and 200±10 K.

- Second research, "G345.45+1.50: An expanding ring-like structure with massive star formation".

  – Aims. To determine the physical conditions of the ring-like structure G345.45 +1.50, which contains ∼54 clumps detected in 1.2 mm continuum emission with an average mass of 75 $M_\odot$. The ring is located 1.°5 above the galactic plane at 1.8 kpc from the Sun, thus there is little superposition of molecular structures along the line-of-sight minimizing confusion effects in identifying individual clumps.

  – Methods. We observed the whole ring in the ^{13}CO(3-2) line using the Atacama Pathfinder Experiment (APEX) telescope. The observations cover 17′×20′ in the sky with an angular resolution of 18″ and a rms of ∼1 K at spectral resolution of 0.1 km s^{-1}.

  – Results. The ring contains a total mass of 6.9×10^3 $M_\odot$ and is expanding with a velocity of 1.4 km s^{-1}. We estimate an expanding time scale of $\sim 2.4\times10^6$ yr and a total energy of $\sim 1.4\times10^{47}$ erg. A possible origin of the ring is a supernova explosion, since a 35.5 cm source, J165920-400424, is near to the center of the ring, at 90 arcsec, without an infrared counterpart. In the fragmented structure of the ring, we identify 57 clumps with diameters between 0.3 and 1.0 pc, masses between 7.4 and 8.6×10^2 $M_\odot$, and densities between 2×10^3 and 5×10^4 cm^{-3}. Assuming that clumps can be modeled as Bonnor-Ebert spheres, to be in hydrostatic equilibrium the clumps require an average

external pressures of $7\times10^6\,\mathrm{K\,cm^{-3}}$. In the region, 5 molecular outflows are identified, which have an average size of 2.0 pc, an average projected speed gradient of $1.7\,\mathrm{km\,s^{-1}\,pc^{-1}}$, and an average projected energy of 8×10^{45} erg. We have identified infrared sources good candidates to drive three of the observed molecular outflows.

Acknowledgements

Thank my family, supervisors and teachers for all your help during my Ph.D. thesis.

C.L. acknowledges partial support from the GEMINI-CONICYT FUND, project number 32070020, ESO-University of Chile Student Fellowship, the Chilean Center for Astrophysics FONDAP N° 15010003 and by Center of Excellence in Astrophysics and Associated Technologies PFB 06.

Contents

List of Figures

List of Tables

Chapter 1

Introduction

1.1 Giant molecular clouds

High-mass stars are known to be born in massive and dense clumps embedded within giant molecular clouds (GMCs; Zinnecker & Yorke 2007). These GMCs have typical radii of $\sim$60 pc, masses of 10^6 $M_\odot$ and temperatures of $\sim$10 K, and are found to be concentrated toward the Galactic plane (Grabelsky et al. 1988). This gives rise to spatial and kinematic blending along the line-of-sight. For example, the CO emission, the most frequently used tracer of molecular gas for GMCs, with a low critical density ($\sim 10^2$ cm^{-3}), is often complex with multiple profile components. To overcome these observational difficulties and perform a complete census of massive-star forming regions (MSFRs) in a whole GMC, ideally requires one to study GMCs above and below the Galactic plane using a high density tracer. Recent surveys of dust condensations within whole GMCs have been made toward RCW 106 (Mookerjea et al. 2004), Cygnus X (Motte et al. 2007), and NGC 6334 (Muñoz et al. 2007) using millimeter continuum emission as a high density tracer.

1.2 Clumps in GMCs

Observations in molecular lines (e.g. Bains et al. 2006) and dust continuum emission (e.g. Muñoz et al. 2007) on spatial scales smaller than ~1 pc show that GMCs have a fragmented structure, and these sub-structures have been referred to as clumps (Williams et al. 2000).

Clumps in GMCs have masses from 4 to 10^4 $M_\odot$, diameters from 0.2 to 2 pc, and densities from 10^3 to 10^5 cm^{-3}. The clump mass distribution is consistent with a power law $dN/dM \propto M^{-\alpha}$, where dN/dM is the number of objects by mass interval, M is the mass, and α is the mass spectral index. The derived mass spectral indices range between 1.3 and 1.8 (e.g. Mookerjea et al. 2004; Muñoz et al. 2007), values similar to those found for the mass distribution of molecular clouds as a whole (α=1.5-1.6; Sanders et al. 1985; Solomon et al. 1987; Williams & McKee 1997). The similarity between the spectral mass indices suggests a common origin; however, different mechanisms have been proposed to explain the formation of clumps and GMCs. On the one hand, large-scale gravitational instabilities, in the combined medium of the collisionless stars and the collisional gas, drive spiral density waves (e.g. Li et al. 2005), and are likely to be the main mechanism behind GMC formation. On the other hand, since GMCs are considered turbulent and supersonic, it is expected that the clump formation is, to first order, produced by ram pressures from supersonic flows, which can provide the seeds for a gravitational fragmentation (Ballesteros-Paredes et al. 2006 and 2007; Bonnell et al. 2007; Klessen et al. 1998).

1.3 Massive star formation

MSFRs are embedded in GMCs, generating a high Lyman continuum photon flux ($\gtrsim 2\times10^{45}$ photons sec^{-1}; Panagia 1973) that ionizes the surrounding gas and heats the surrounding dust. These MSFRs can thus be identified by infrared emission from heated dust and/or by radio emission from ionized gas. They can also be identified based on both their molecular lines from high density gas and their millimeter and sub-millimeter continuum emission

from dust.

Bronfman et al. (1996) showed that 60% of the IRAS point sources in the Galactic plane with far infrared (FIR) colors typical of ultra compact (UC) HII regions (Wood & Churchwell 1989) are associated with dense molecular structures seen in the CS(2-1) line ($\gtrsim 10^4$-10^5 cm^{-3}). Hereafter, these sources will be referred to as IRAS-CS sources. From observations in 1.2 mm continuum emission of 146 IRAS-CS sources, Faúndez et al. (2004) showed that MSFRs are associated with condensations of gas and dust. Infrared studies, however, cannot provide a complete census of the birth sites of massive stars, since there are massive condensations that are undetected at infrared wavelengths. For example, Garay et al. (2004) found four clumps with masses between 4×10^2 and 2×10^3 M$_\odot$ and densities of $\sim 2\times10^5$ cm^{-3}, without infrared emission, located close to clumps associated with MSFRs. They suggested that these cold ($\lesssim$17 K), dense, and massive clumps will eventually form high mass stars. Hill et al. (2005) found 113 cold clumps, which have a mean mass of $\sim$800 M$_\odot$, a mean radius of $\sim$0.4 pc, and a mean density of $\sim 10^5$ cm^{-3}. Beltrán et al. (2006) found 95 cold clumps with a mean mass of 96 M$_\odot$, a mean radius of 0.4 pc, and a mean density of 9×10^4 cm^{-3}.

1.4 Ring like and shell like structures in the ISM

Observations in HI, molecules and dust show that the presence of ring like and shell like structures in the interstellar medium (ISM) is ubiquitous (e.g. Churchwell 2008; Heiles 1979; Martín-Pintado et al. 1999; Oka et al. 1998; Schuller et al. 2009; Wong et al. 2008). In the galaxy, these structures range up to 1.2 kpc in radius, 2x10^7 M$_\odot$ in mass and 10^{53} erg in kinetic energy. Their formations have been associated with the energy released by massive stars, as stellar winds, supernova explosions and ionizing radiation, or collisions of high-velocity HI clouds with the galactic disk (Tenorio-Tagle & Bodenheimer 1988). Shells with size less than 100 pc have been correlated with OB associations or stellar clusters in their interiors (Tenorio-Tagle & Bodenheimer 1988), or with hot cores and molecular clumps in their borders (e.g. Martin-Pintado et al. 1999; Wong et al. 2008).

1.5 This thesis

This thesis is based in two research using observations toward the GMC G345.5+1.0 in the 1.2 mm continuum emission and in the ^{13}CO(3-2) line. The determination of physical properties of a sample of clumps belonging to a single GMC is desirable since, in this way, the distance to the GMC is a factor that influences neither the mass distribution or the relationships between physical properties. However, these studies are difficult because of the superposition of dust and molecular structures along the line-of-sight to GMCs in the Galactic plane. The GMC G345.5+1.0 is chosen as our target for two reasons. First, it is located $\sim 1^{\circ}$ above the Galactic plane, so our observations in 1.2 mm continuum emission are roughly free of confusion with background or foreground structures along the line-of-sight. Second, it is at 1.8 kpc from the Sun, near enough to resolve clumps associated with MSFRs, but far enough away to permit a complete coverage of the GMC.

- First research, "Massive star formation in the GMC G345.5+1.0: Spatial distribution of the dust emission".

  To undertake a complete census of dense and massive clumps, including those with and without infrared emission, the whole of GMC G345.5+1.0 is observed in 1.2 mm continuum emission.

  The main characteristics of both the GMC G345.5+1.0 and the clumps within the GMC are determined.

- Second research, "G345.45+1.50: An expanding ring-like structure with massive star formation".

  We observed the whole ring G345.45+1.50 in the ^{13}CO(3-2) line to study the physical conditions for the formation of massive stars. This structure is part of the GMC G345.5+1.0.

  The total mass and the column density of the ring are estimated. We study its kinematic structure, and find that the ring is expanding and contains 5 molecular outflows. Clumps are identified and their masses, sizes and densities are calculated. Their masses are compared with those found in 1.2 mm continuum emission. Infrared observations, from MSX and SPITZER, are compared with the molecular

structure and cold clumps are distinguished.

Chapter 2

Observations

2.1 1.2 mm continuum emission

We observed the whole GMC G345.5+1.0 in continuum emission at 1.2 mm using SIMBA mounted on the SEST. The SEST is a 15-m diameter radio telescope, which operated between 70 and 365 GHz, and SIMBA is a 37-channel hexagonal bolometer, operating at 250 GHz (1.2 mm), with a passband equivalent width of 90 GHz (FWHM). The configuration SEST-SIMBA had a beamsize of 24″, which corresponds to a spatial resolution of ∼0.2 pc at the GMC distance (1.8 kpc).

Observations were made in October 2002 and July 2003, using the fast mapping mode, and consist of 185 images of 15′ (azimuth) ×10′ (elevation) in size. The scans were made in azimuth at a rate of 80″ s^{-1}, and they were separated in elevation by 8″; the total integration time per map was about 25 minutes. Measurements of the atmospheric opacity were made through skydips about every three hours, and values at the zenith ranged between 0.09 and 0.31. Data were reduced using the MOPSI software (developed by Robert Zylka, IRAM, Grenoble, France), and calibrated (in terms of flux density) with observations toward Uranus, one made in October 2002, and an additional eight made in July 2003. Bolometer channels were corrected for the correlated noise by inspecting the sur-

rounding channels. The noise correlation between 1 and 900 arcsec, and between 100 and 900 arcsec inferred an uncertainty/error smaller than 20% in the flux densities of detected sources. The calibration factor has a value of 0.086 Jy counts^{-1} for October 2002, and a mean value of $\sim$0.069$\pm$0.005 Jy counts^{-1} for July 2003. These variations agree with the uncertainty estimated by Faúndez et al. (2004) of 20% in the flux density measurements using SIMBA data.

For the 185 images, we achieved an rms of between 0.023 and 0.080 Jy beam^{-1}, with a median of 0.036 Jy beam^{-1}, for a beam calibration area of $\sim$653 arcsec^2 ("SIMBA Data Reduction Handbook"). The individual maps were combined in a mosaic of $1.^\circ8\times2.^\circ2$ in size, centered at $345.^\circ40$ in Galactic longitude and $+1.^\circ10$ in Galactic latitude, and with a final rms of $\sim$20 mJy beam^{-1}.

2.2 ^{13}CO(3-2) line

We made observations in the ^{13}CO(3-2) line at 330.588 GHz, using the On-The-Fly (OTF) observing mode with the APEX-2A heterodyne receiver mounted on in the APEX[1] telescope. These observations cover the whole ring-like structure G345.45+1.50, with a beam size of 18″, $\sim$0.2 pc at 1.8 kpc from the Sun, and with a spectral resolution of 122 kHz, $\sim$0.1 km s^{-1} at 331 GHz. The bandwidth is 1 GHz with 8192 channels. The size steep was 6 arcsec and the dump integration time was 1.0 sec. These observations were performed on October 17th, 18th, 19th 2005, May 28th 2006, June 24th, 25th, 26th 2006, October 7th, 8th, 9th and 10th 2006. The total time on source is $\sim$14 hrs. The main beam efficiency is estimated to be $\sim$0.73 (Güsten et al. 2006).

Data were reduced using XS software, developed by Per Bergman (APEX team). We created a data cube of $\sim17\times22$ arcmin^2, that consists of 3036 spectra with an averaged rms in the antenna temperature, T_A^*, of $\sim$1 K at a spectral resolution of $\sim$0.1 km s^{-1}.

[1]This research is based on data acquired with the Atacama Pathfinder Experiment (APEX). APEX is a collaboration between the Max-Planck Institut für Radioastronomie, the European Southern Observatory, and the Onsala Space Observatory.

2.3 ^{12}CO(3-2) line

To estimate the gas temperature in the region, we observed 29 peaks of the ^{13}CO(3-2) line emission in the ^{12}CO(3-2) line using the ASTE telescope in the position switching observing mode on August 27th 2010. We tried to observe 57 positions (see Sect. 4.4), however this was impossible by bad weather conditions. Table 4.1 gives the positions of the observed peaks in equatorial coordinates. At the ^{12}CO(3-2) line transition frequency, ~345.796 GHz, the beam size of the ASTE telescope is ~22″, ~0.2 pc at 1.8 kpc from the Sun. We used the CATS-345 GHz receiver, integrating between 20 and 30 seconds on source. Data have a spectral resolution of 125 KHz, ~0.1 km s^{-1} at the ^{12}CO(3-2) line transition frequency. The bandwidth is 128 MHz with 1024 channels. ASTE team estimate a main beam efficiency of ~0.7.

Data were reduced using NEWSTAR software, resulting 29 spectra with a rms of ~0.2 K (antenna temperature) at 0.1 km s^{-1}.

2.4 ^{12}CO(1-0) line survey of the Southern Galaxy

To estimate the properties of the GMC 345.5+1.0, we utilize the Columbia University - Universidad de Chile ^{12}CO(1-0) line survey of the Southern Galaxy (Bronfman et al. 1989). It was the first out-of-plane CO survey of the southern Milky Way, completed in 1984 using the 1.2 m Columbia Southern Millimeter-Wave Telescope at Cerro Tololo, Chile. The Survey covers a strip 4° thick in Galactic latitude, from b=-2° to 2° , and extends from 300° to 348° in longitude. Observations were made with a sampling interval of $0.^{\circ}125$ for $|b| \leq 0.^{\circ}75$ and of $0.^{\circ}25$ for $|b| \geq 2.^{\circ}0$, an angular resolution of $0.^{\circ}147$, and sensitivity of 0.1 K (antenna temperature) at a spectral resolution of 1.3 km s^{-1}. The main beam efficiency was 0.82. Necessary data was directly acquired from Bronfman.

2.5 CS(2-1) line survey toward MSFRs

To associate 1.2 continuum emission with the GMC, we use observation made toward MSFRs in the CS(2-1) line (Bronfman et al. 1996). Survey toward the Southern Galaxy was made with SEST, between 1989 and 1992. The 15 m SEST has a beamwidth of 50″ at the CS(2 – 1) line frequency (~97.981 GHz). Observations have a spectral resolution of 0.13 km s^{-1}, but were smoothed in velocity by a factor of 4, to obtain a rms noise of 0.1 K in the spectra at a velocity resolution of 0.52 km s^{-1}. Necessary data was directly acquired from Bronfman.

2.6 Online archives

To analyze clumps identified in 1.2 mm continuum emission and in ^{13}CO(3-2) line, we include online data from four archives, IRAS observations, MSX observations, SPITZER (IRAC) observations and MGPS observations.

2.6.1 IRAS observations

InfraRed Astronomical Satellite (IRAS) was a mission started in 1983 during 11 months, observing the all sky in four bands, 12, 25, 60 and 100 μm. Resolutions for the instruments are ~0.5, 0.5, 1.0 and 2.0 arcmin, for 12, 25, 60 and 100 μm, respectively. However, resolutions for data is determined by the size of detectors, ~1′×5′, 1′×5′, 2′×5′ and 4′×5′, for 12, 25, 60 and 100 μm, respectively. Necessary data was acquired from IRSA server (http://irsa.ipac.caltech.edu/), trough of both the IRAS Point Source Catalog (IRAS PSC; version 2.0, 1986) and the IRAS Sky Survey Atlas (ISSA).

2.6.2 MSX observations

Midcourse Space Experiment (MSX) is a satellite that observed at 8.28 μm (Band A), 12.13 μm (Band C), 14.65 μm (Band D) and 21.3 μm (Band D) all galactic longitude between -5° and 5° galactic latitude between 1996 and 1997. Resolution of observations is 18.3″ for all bands, and is determined by the size of detectors. Necessary data was acquired from IRSA server (http://irsa.ipac.caltech.edu/), trough of both the MSX Point Source Catalog (MSX PSC; version 2.3, 2003) and the MSX Data Atlas.

2.6.3 SPITZER (IRAC) observations

Spitzer Space Telescope is a satellite equipped with the Infrared Array Camera (IRAC), which detect at 3.6, 4.5, 5.8 and 8.0 μm. This satellite was lunched in 2003, and is still active. IRAC Bands have resolutions of 1.6″, 1.6″, 1.8″ and 1.9″ at 3.6, 4.5, 5.8 and 8.0 μm bands, respectively (Fazio et al. 2004). Necessary data was acquired from IRSA server (http://irsa.ipac.caltech.edu/), trough of the Galactic Legacy Infrared Midplane Survey Extraordinaire (GLIMPSE) Atlas.

2.6.4 MGPS observations

Molonglo Galactic Plane Survey (MGPS) was carried out with the Molonglo Observatory Synthesis Telescope at frequency of 843 MHz (35.6 cm) and with a restoring beam of 45″×45csc(|δ|)″ (Murphy et al. 2007). The survey covers |b|<10° and 245°<l<365°. Necessary data was acquired trough of mosaics (http://www.astrop.physics.usyd.edu.au/mosaics/) and trough of The Molonglo Galactic Plane Survey (MGPS-2) Compact Source Catalogue (http://www.astrop.physics.usyd.edu.au/mgpscat/mgpscat.Aug-15-2007).

Chapter 3

Massive star formation in the GMC G345.5+1.0: Spatial distribution of the dust emission

3.1 GMC G345.5+1.0

The GMC G345.5+1.0 was first observed as part of the Columbia University - Universidad de Chile ^{12}CO(1-0) Survey of the Southern Galaxy (Bronfman et al. 1989). It is located approximately between 344.°5 and 346.°5 in Galactic longitude, and between 0.°2 and 2.°0 in Galactic latitude. Figure 3.1 shows the spectrum of the ^{12}CO(1-0) line emission integrated over the area of the GMC. The emission of the GMC is between -33 and -2 km s^{-1} (LSR velocities) with a peak at -13.6 km s^{-1}.

We estimate the kinematic distance using the rotation curve determined by Alvarez et al. (1990), with a Galactocentric solar distance of 8.5 kpc and a solar LSR velocity of 220 km s^{-1}. Considering a Galactic longitude of 345.°5 and LSR velocity of -13.6 km s^{-1}, the GMC is within the solar circle with two possible kinematic distances: ∼1.8 and 15 kpc. Thus, the GMC is ∼31 or 262 pc above the Galactic plane, a factor 0.5 or 4.4 of the HWHM

Table 3.1: Summary of main characteristics of G345.5+1.0.

Distance	1.8 kpc
Total mass	$6.5\text{x}10^5$ $M_\odot$
Radius	34 pc
[a]Density	70 cm^{-3}
[a]Column density	10^{22} cm^{-2}
LSR velocity	-13.6 km s^{-1} (between -33 and -2 km s^{-1})

[a] The density and the column density are computed assuming a mean molecular weight of μ=2.29.

of the molecular Galactic disk (~60 pc; Bronfman et al. 2000), respectively. Therefore, 1.8 kpc is the most probable kinematic distance to the GMC.

Physical properties of the GMC are estimated using the ^{12}CO(1-0) line observations. The ^{12}CO(1-0) line emission integrated over the full spatial and spectral extension of the GMC is 192 K km s^{-1} deg^2. Using a ratio of H_2 column density to integrated ^{12}CO(1-0) line emission N_{H_2}/W_{co} equal to $1.56\text{x}10^{20}$ cm^{-2} (K km s^{-1})$^{-1}$ (Hunter et al. 1997), the total mass of the GMC is $6.3\text{x}10^5$ $M_\odot$, corrected by a factor of 1.3 to account for 25% of helium. Since its angular size is $2.^\circ0\text{x}1.^\circ8$, the GMC has a mean radius of ~34 pc, mean column density of ~10^{22} cm^{-2} and mean density of ~70 cm^{-3}, where the depth of the cloud has been assumed to be same as its radius. Table 3.1 summarises the main characteristics of this GMC. The derived physical properties confirm that the most probable distance to the GMC is ~1.8 kpc. If at the far kinematic distance (15 kpc), the GMC would have a mean radius of 280 pc and a total mass of $4.4\text{x}10^7$ $M_\odot$, values much higher than the typical value of 60 pc in radius and 10^6 $M_\odot$ in mass (Dame et al. 1986); Williams & McKee (1997) found that the molecular cloud mass distribution within the solar circle has an upper mass limit of 6×10^6 $M_\odot$.

3.2 1.2 mm continuum emission

Figure 3.2 presents the 1.2 mm emission image of the whole GMC G345.5+1.0. The total flux density of the GMC G345.5+1.0 is ~365 Jy, which is estimated by integrating the

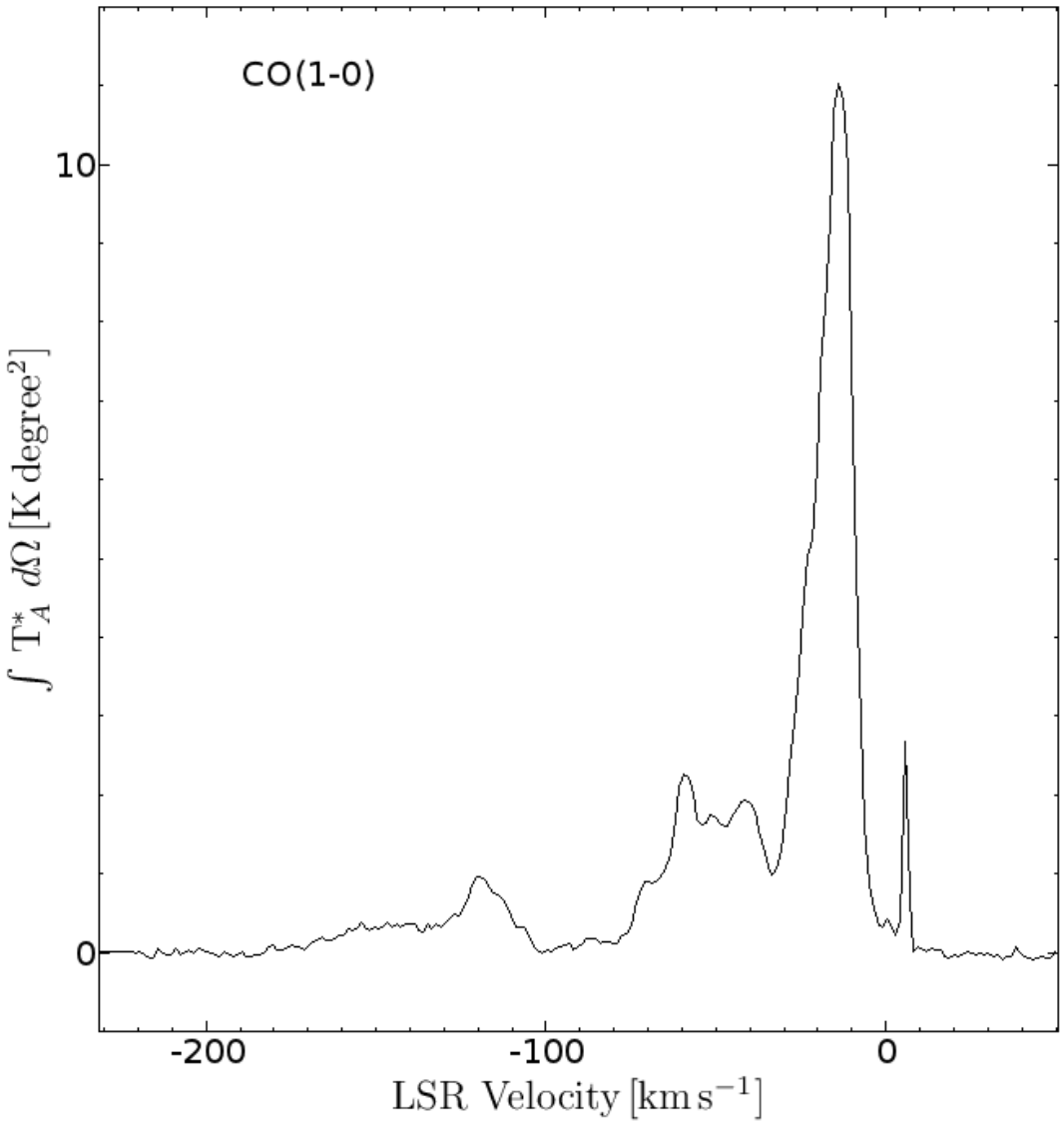

Figure 3.1: Spectra of the ^{12}CO(1-0) line emission integrated over the whole area of the GMC G345.5+1.0 (between 344.°5 and 346.°5 in Galactic longitude and between 0.°2 and 2.°0 in Galactic latitude; Bronfman et al. 1989). Emission from the GMC under study is between -33 and $-2\,\mathrm{km\,s^{-1}}$ with a peak at $-13.6\,\mathrm{km\,s^{-1}}$.

intensity over the whole area of the cloud.

As can be seen in the integrated spectrum of the ^{12}CO(1 – 0) line (Fig. 3.1), across GMC G345.5+1.0 (LSR velocity between −33 and −2 km s^{-1}), there are additional molecular gas components along the line-of-sight, particularly in the ranges −170 to −100 km s^{-1}, −75 to −33 km s^{-1}, and 0 to 5 km s^{-1}. Hence, the question arises as to whether the 1.2 mm continuum emission only traces dust condensations within GMC G345.5+1.0? To examine the association of the GMC with 1.2 mm continuum emission, Fig. 3.3 shows images of the velocity-integrated ^{12}CO(1 – 0) emission in three velocity ranges (−200 to −33 km s^{-1}, −33 to −2 km s^{-1}, and −2 to 50 km s^{-1}) superimposed with contours of the 1.2 mm continuum emission. Figure 3.3 shows that most of the emission detected in 1.2 mm is associated with the GMC. About 1% of the total observed area might also be associated with gas at velocities <-33 km s^{-1} (Fig. 3.3, top), localized mainly in the region of the IRAS point sources 17008-4040 (G345.499+0.354) and 17009-4042 (G345.490+0.311).

From the survey of Bronfman et al. (1996), we find that there are eight IRAS-CS sources within the region and two IRAS point sources that are not detected in the CS(2-1) line (see Table 3.2). As is shown in both the ^{12}CO(1-0) maps (Fig. 3.3) and the 1.2 mm continuum emission map (Fig. 3.4), these MSFRs, or IRAS-CS sources, are associated with the GMC and have a counterpart in 1.2 mm. They correspond to the most dense and massive dust condensations (see Table 3.3). The two IRAS point sources not detected in the CS(2-1) line were also not detected in the continuum (see Fig. 3.4). The eight IRAS-CS sources include the IRAS point sources 17008-4040 and 17009-4042. Line profiles toward these two objects in the ^{12}CO(1-0) and CS(2-1) lines are shown in Fig. 3.5. Gas components with velocities <-33 km s^{-1} observed in the ^{12}CO(1-0) line are not observed in the CS(2-1) line, suggesting that they correspond to regions of low density gas. Since 1.2 mm continuum emission traces high densities (e.g. Faúndez et al. 2004), it should not be detected in these clouds. In summary, from observations in the ^{12}CO(1-0) and CS(2-1) lines, we conclude that the 1.2 mm continuum emission is associated only with the GMC.

Table 3.2: List of IRAS point sources along the line-of-sight to the GMC G345.5+1.0 observed in the CS(2-1) line by Bronfman et al. (1996).

IRAS name	Galactic coord.		LSR velocity[1]	FWHM[1]
	longitude	latitude	[km s^{-1}]	[km s^{-1}]
16533-4022	344.845	1.646	undetected	
16571-4029	345.208	1.028	-15.6	4.9
16577-4028	345.286	0.933	undetected	
16575-4023	345.332	1.014	-14.5	2.8
16561-4006	345.393	1.399	-11.9	3.5
16557-4002	345.395	1.512	-12.4	3.1
17009-4042	345.490	0.311	-16.7	6.0
16562-3959	345.494	1.468	-11.6	5.5
17008-4040	345.499	0.354	-16.4	4.8
16596-4012	345.717	0.817	-11.5	4.9

[1] Values from Bronfman et al. (1996).

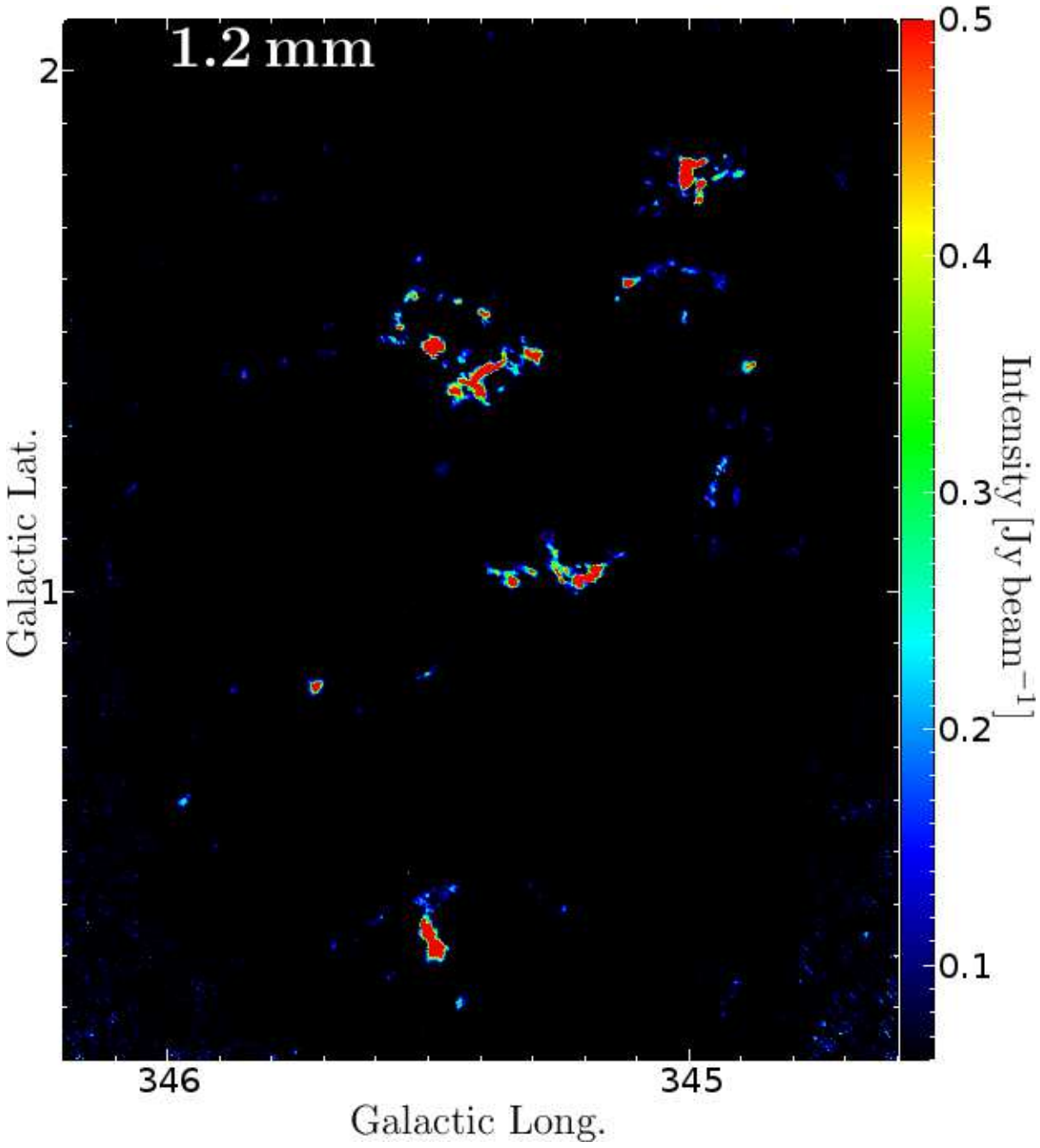

Figure 3.2: Map of the GMC G345.5+1.0 in 1.2 mm continuum emission. Observations were made using SIMBA, with a spatial resolution of 0.2 pc. They cover $1.^{\circ}8 \times 2.^{\circ}2$ in the sky, with an rms of 20 mJy beam^{-1}.

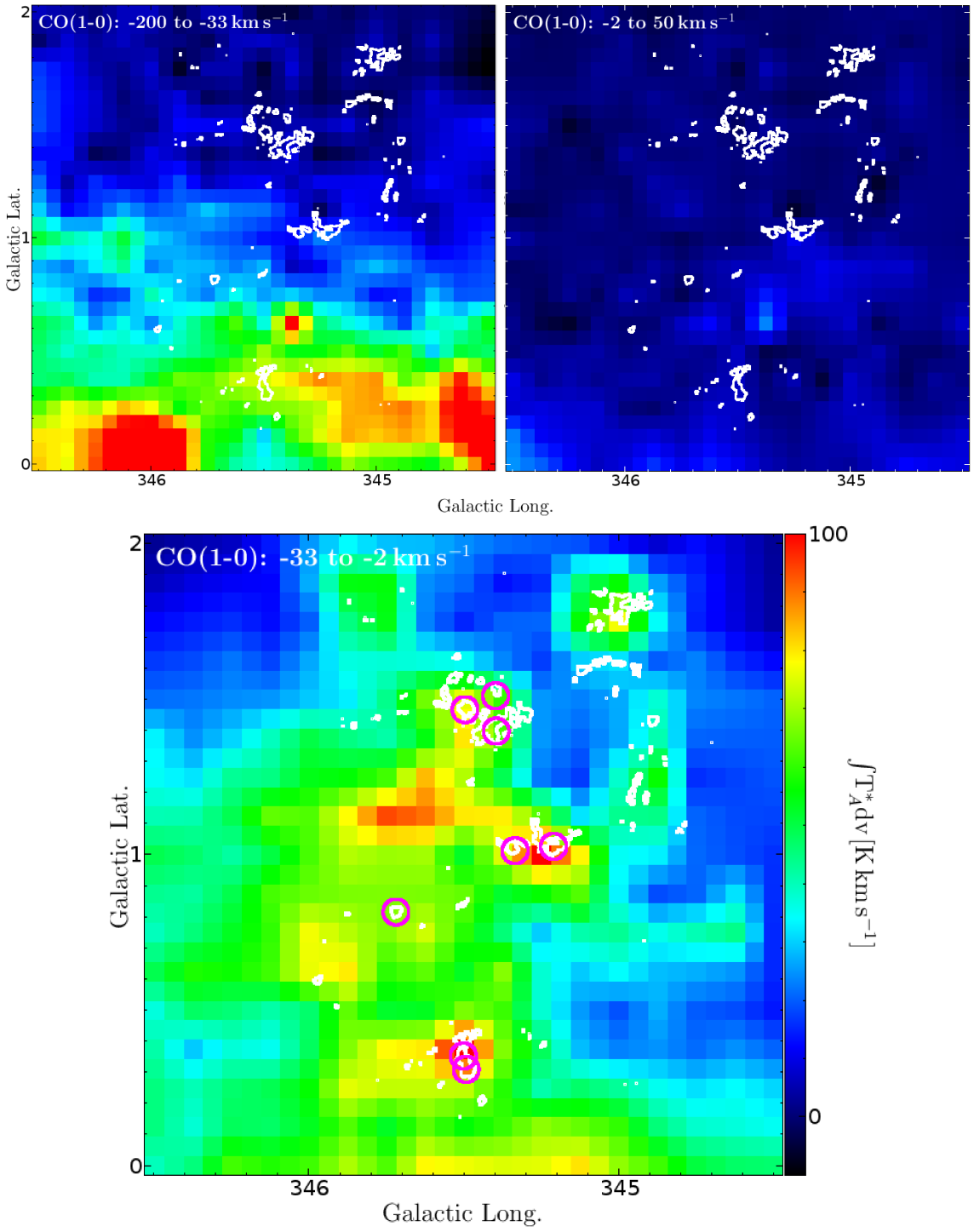

Figure 3.3: Integrated ^{12}CO(1-0) emission toward GMC G345.5+1.0 in different LSR velocity ranges (Bronfman et al. 1989). Top-left: from −200 to −33 km s^{-1}. Top-right: from −2 to 50 km s^{-1}. Bottom: from −33 to −2 km s^{-1}. Magenta circles mark spatial and spectral positions of detections in the CS(2-1) line toward MSFRs (Table 3.2). Contours represent 1.2 mm continuum emission at 5 times rms, ∼0.1 Jy beam^{-1}.

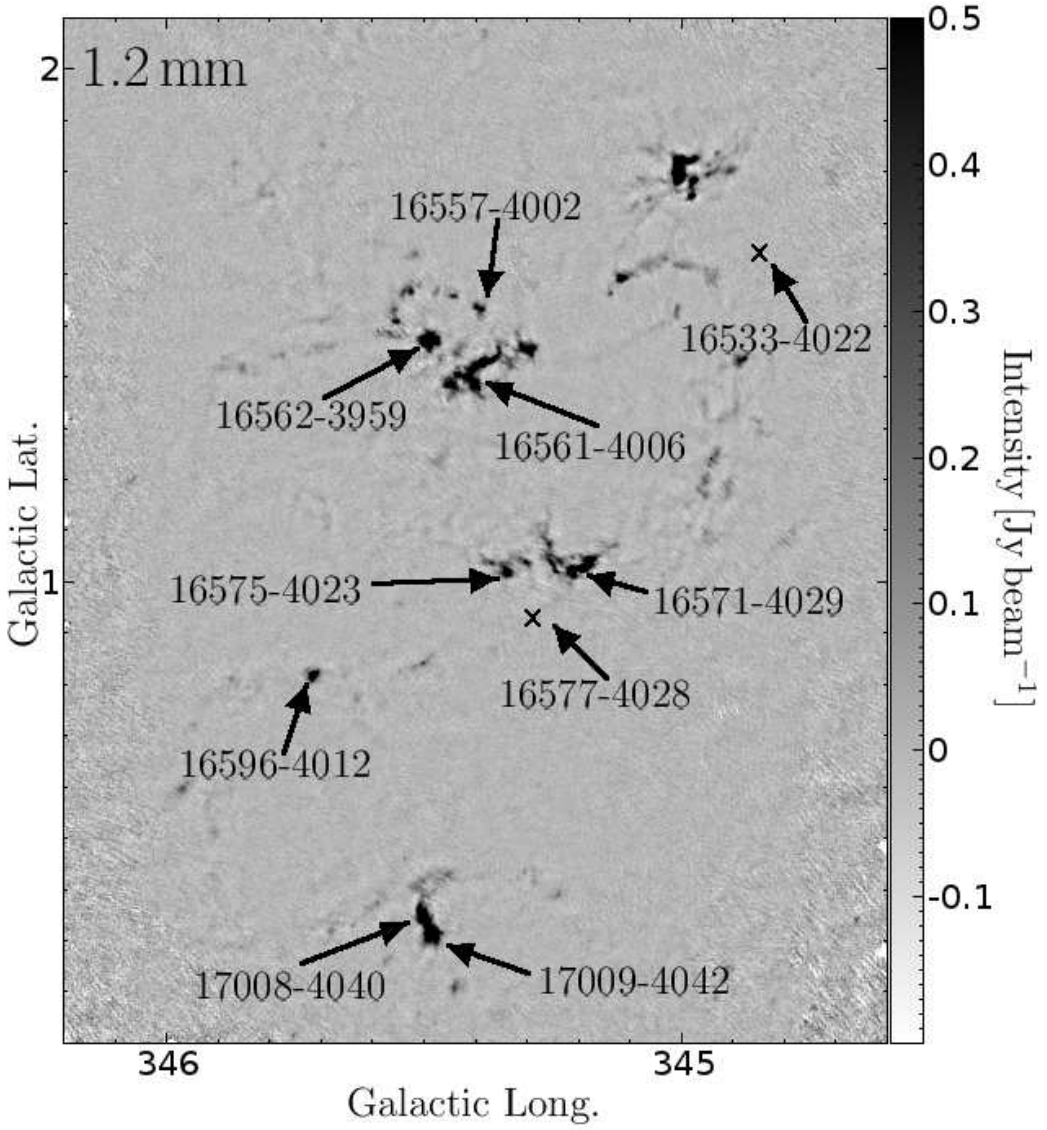

Figure 3.4: IRAS point sources along the line-of-sight of the GMC G345.5+1.0 observed in the CS(2-1) line (Bronfman et al. 1996). Gray scale represents 1.2 mm continuum emission. Arrows mark CS(2-1) line observations, and crosses indicate observations without detection (see Table 3.2).

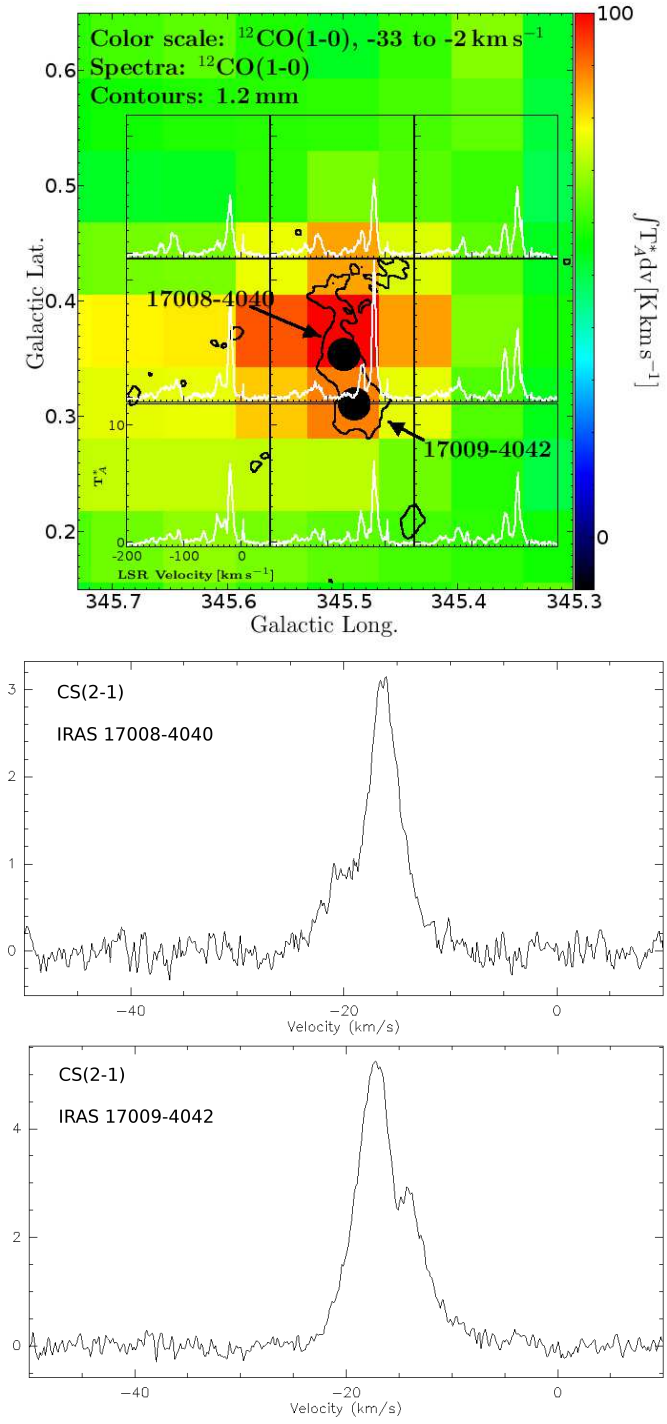

Figure 3.5: Line profiles toward the IRAS point sources 17008-4040 and 17009-4042: top image, ^{12}CO(1-0) line profiles (Bronfman et al. 1989), over a map of their integrated emissions (color scale) and with contours of 1.2 mm continuum emission; middle and bottom images, CS(2-1) line profiles (their observing positions are indicated as black dots in the top image; Bronfman et al. 1996).

3.3 Identification of clumps

The structure of the GMC observed in 1.2 mm continuum emission (Fig. 3.2) is fragmented, and it is possible to distinguish several clumps.

To identify clumps we utilize CLUMPFIND[1] (Williams et al. 1994), which creates contours over data, searches for peaks of emission to locate clumps, and follows them down to the lower intensity contour.

CLUMPFIND finds 201 clumps in the 1.2 mm continuum emission map of the GMC, containing ∼100% of the total emission above 3σ. We used a lower intensity contour of three rms, ∼0.06 Jy beam^{-1}, and a contouring interval equal to twice the rms noise, ∼0.04 Jy beam^{-1}. To delete fictitious structures, we imposed two conditions on the CLUMPFIND output, that the angular size of the emission and the emission peak of clumps had to be greater than the beam size, $\sim 24'' \times 24''$, and five times rms, ∼0.1 Jy beam^{-1}, respectively. The angular size is defined to be the angular area inside the lowest intensity contour (three rms). The 201 identified clumps have areas between ∼0.18 and 7.3 arcmin^2, emission peaks between 0.1 and 9 Jy beam^{-1}, and flux densities between 0.089 and 40 Jy.

Table 3.3 shows the characteristics of each clump calculated in this section, Sect. 3.4 and Sect. 3.5. Column 1 gives clump names; columns 2 and 3, Galactic coordinates of peaks in 1.2 mm continuum emission; column 4, 1.2 mm flux densities; column 5, diameters (deconvolved FWHM sizes); column 6, masses; column 7, densities; column 8, column densities; and column 9, if clumps have (”Y”) or do not have (”N”) an infrared counterpart from MSX and SPITZER observations.

[1] http://www.ifa.hawaii.edu/users/jpw/clumpfind.shtml

Table 3.3: Properties of identified clumps in the GMC G345.5+1.0. Column 1 gives clump names; columns 2 and 3, galactic coordinates of peaks in 1.2 mm continuum emission; column 4, 1.2 mm flux densities; column 5, diameters; column 6, masses; column 7, densities; column 8, column densities; and column 9, if clumps are detected in all infrared MSX and SPITZER-IRAC bands ("Y") or not ("N"). The densities and the column densities are computed assuming a mean molecular weight of μ=2.29.

Name	Galactic coord. long.	lat.	$S_{1.2mm}$ Jy	Diameter pc	Mass $M_\odot$	Density cm^{-3}	Column density cm^{-2}	Infrared counterpart
1	345.490	1.471	40	0.5	1.3×10^3	2.9×10^5	3.2×10^{23}	Y
2	345.488	0.316	38	0.6	1.3×10^3	2.3×10^5	2.7×10^{23}	Y
3	345.006	1.795	32	0.5	1.1×10^3	3.9×10^5	3.6×10^{23}	Y
4	345.506	0.347	22	0.6	7.2×10^2	1.4×10^5	1.6×10^{23}	Y
5	345.193	1.026	11	0.3	3.5×10^2	3.3×10^5	2.3×10^{23}	Y
6	345.385	1.428	9.8	0.3	3.3×10^2	3.3×10^5	2.2×10^{23}	Y
7	345.006	1.820	12	0.4	4.1×10^2	2.4×10^5	1.9×10^{23}	Y
8	345.179	1.043	9.1	0.5	3.0×10^2	8.2×10^4	8.4×10^{22}	Y
9	345.213	1.022	9.4	0.4	3.1×10^2	1.6×10^5	1.3×10^{23}	Y
10	344.992	1.821	10	0.5	3.4×10^2	8.0×10^4	8.6×10^{22}	Y

Continued on next page

Table 3.3 – continued from previous page

Name	Galactic coord. long.	lat.	$S_{1.2mm}$ Jy	Diameter pc	Mass $M_\odot$	Density cm^{-3}	Column density cm^{-2}	Infrared counterpart
11	345.115	1.592	6.6	0.5	2.2×10^{2}	7.4×10^{4}	7.0×10^{22}	Y
12	345.716	0.818	7.2	0.5	2.4×10^{2}	7.5×10^{4}	7.3×10^{22}	Y
13	345.337	1.018	7.2	0.5	2.4×10^{2}	8.3×10^{4}	7.8×10^{22}	Y
14	344.976	1.783	5.7	0.4	1.9×10^{2}	9.3×10^{4}	7.8×10^{22}	N
15	344.980	1.752	3.5	0.3	1.2×10^{2}	9.6×10^{4}	6.8×10^{22}	N
16	345.367	1.434	3.8	0.3	1.2×10^{2}	1.3×10^{5}	8.5×10^{22}	Y
17	345.296	1.452	10	0.6	3.4×10^{2}	4.4×10^{4}	5.8×10^{22}	Y
18	345.401	1.419	4.7	0.4	1.6×10^{2}	1.1×10^{5}	8.1×10^{22}	N
19	345.418	1.401	2.9	0.3	95	1.9×10^{5}	1.0×10^{23}	N
20	345.395	1.380	4.5	0.5	1.5×10^{2}	4.0×10^{4}	4.1×10^{22}	Y
21	345.411	1.406	2.9	0.3	96	1.9×10^{5}	1.0×10^{23}	Y
22	345.434	1.405	2.8	0.3	94	1.1×10^{5}	7.0×10^{22}	N
23	345.443	1.387	3.5	0.4	1.2×10^{2}	7.9×10^{4}	6.0×10^{22}	N
24	345.453	1.386	3.2	0.4	1.1×10^{2}	7.4×10^{4}	5.5×10^{22}	N
25	345.406	1.394	2.9	0.3	95	1.3×10^{5}	7.6×10^{22}	Y
26	345.389	1.531	2.0	0.3	66	1.2×10^{5}	6.5×10^{22}	Y

Continued on next page

Table 3.3 – continued from previous page

Name	Galactic coord. long.	lat.	$S_{1.2mm}$ Jy	Diameter pc	Mass $M_\odot$	Density cm^{-3}	Column density cm^{-2}	Infrared counterpart
27	345.554	1.508	1.7	0.2	58	1.4×10^{5}	7.0×10^{22}	N
28	345.398	1.538	1.7	0.2	55	1.4×10^{5}	6.7×10^{22}	N
29	345.244	1.021	1.8	0.3	58	9.9×10^{4}	5.5×10^{22}	N
30	345.301	1.040	1.8	0.3	60	1.2×10^{5}	6.3×10^{22}	Y
31	345.525	1.567	1.8	0.3	59	6.4×10^{4}	4.1×10^{22}	N
32	345.396	1.389	1.5	–	49	–	–	Y
33	345.251	1.038	2.1	0.3	68	1.1×10^{5}	6.3×10^{22}	N
34	344.878	1.437	3.9	0.5	1.3×10^{2}	4.1×10^{4}	4.0×10^{22}	Y
35	345.353	1.448	2.5	0.5	82	3.1×10^{4}	2.8×10^{22}	Y
36	345.236	1.040	2.1	0.4	70	5.3×10^{4}	3.9×10^{22}	N
37	344.946	1.796	1.6	0.4	54	3.7×10^{4}	2.8×10^{22}	N
38	345.442	1.558	1.2	0.2	41	1.1×10^{5}	5.3×10^{22}	N
39	345.257	1.073	1.6	0.3	54	7.4×10^{4}	4.4×10^{22}	Y
40	345.368	1.036	1.6	0.5	53	1.9×10^{4}	1.8×10^{22}	Y
41	344.942	1.241	0.55	–	18	–	–	N
42	345.539	1.567	1.5	0.3	49	4.5×10^{4}	3.1×10^{22}	N

Continued on next page

Table 3.3 – continued from previous page

Name	Galactic coord. long.	lat.	$S_{1.2mm}$ Jy	Diameter pc	Mass $M_\odot$	Density cm^{-3}	Column density cm^{-2}	Infrared counterpart
43	345.254	1.052	1.9	0.4	64	5.2×10^{4}	3.7×10^{22}	N
44	344.904	1.803	1.9	0.4	62	4.3×10^{4}	3.3×10^{22}	N
45	345.502	0.842	0.88	0.3	29	4.4×10^{4}	2.6×10^{22}	N
46	345.559	1.531	0.85	0.3	28	5.2×10^{4}	2.8×10^{22}	N
47	345.360	1.389	0.80	0.2	26	6.2×10^{4}	3.1×10^{22}	Y
48	345.441	0.206	1.8	0.5	61	2.2×10^{4}	2.0×10^{22}	Y
49	345.137	1.564	0.61	0.2	20	5.7×10^{4}	2.7×10^{22}	Y
50	345.312	1.046	0.95	0.3	31	5.0×10^{4}	2.9×10^{22}	Y
51	345.445	1.371	1.3	0.5	42	1.5×10^{4}	1.4×10^{22}	N
52	345.334	1.428	1.5	0.4	49	3.6×10^{4}	2.6×10^{22}	Y
53	345.563	1.486	1.1	0.3	35	6.3×10^{4}	3.5×10^{22}	N
54	344.929	1.836	0.50	–	17	–	–	N
55	345.335	1.434	1.1	0.5	36	1.1×10^{4}	1.1×10^{22}	Y
56	345.434	1.445	1.00	0.3	33	7.5×10^{4}	3.8×10^{22}	N
57	345.211	1.049	0.55	0.3	18	3.7×10^{4}	2.0×10^{22}	N
58	345.968	0.598	1.5	0.4	49	3.0×10^{4}	2.3×10^{22}	N

Continued on next page

Table 3.3 – continued from previous page

Name	Galactic coord. long.	lat.	$S_{1.2mm}$ Jy	Diameter pc	Mass $M_\odot$	Density cm^{-3}	Column density cm^{-2}	Infrared counterpart
59	344.945	1.229	0.43	–	14	–	–	N
60	345.006	1.532	1.1	0.4	36	2.5×10^{4}	1.9×10^{22}	Y
61	345.265	1.085	1.2	0.3	39	3.6×10^{4}	2.5×10^{22}	N
62	344.952	1.195	0.88	0.3	29	6.6×10^{4}	3.3×10^{22}	N
63	345.337	1.037	0.99	0.4	33	1.7×10^{4}	1.4×10^{22}	Y
64	345.436	1.418	0.67	0.3	22	4.0×10^{4}	2.2×10^{22}	N
65	345.501	0.418	0.66	0.2	22	5.4×10^{4}	2.7×10^{22}	N
66	345.457	0.428	0.81	0.3	27	3.6×10^{4}	2.2×10^{22}	N
67	344.933	1.251	0.73	0.2	24	7.1×10^{4}	3.3×10^{22}	N
68	345.064	1.747	0.57	0.2	19	6.0×10^{4}	2.7×10^{22}	N
69	345.501	0.389	1.3	0.5	42	1.2×10^{4}	1.2×10^{22}	N
70	345.468	1.431	0.33	–	11	–	–	Y
71	345.558	1.522	0.40	–	13	–	–	N
72	345.010	1.764	0.60	0.3	20	1.7×10^{4}	1.2×10^{22}	N
73	345.590	1.491	0.19	–	6.2	–	–	N
74	344.932	1.231	0.23	–	7.5	–	–	N

Continued on next page

Table 3.3 – continued from previous page

Name	Galactic coord. long.	lat.	$S_{1.2mm}$ Jy	Diameter pc	Mass $M_\odot$	Density cm^{-3}	Column density cm^{-2}	Infrared counterpart
75	344.927	1.806	0.82	0.3	27	3.0×10^{4}	1.9×10^{22}	N
76	344.947	1.813	0.48	0.4	16	1.1×10^{4}	8.3×10^{21}	N
77	344.955	1.170	0.72	0.2	24	6.2×10^{4}	3.0×10^{22}	N
78	344.936	1.245	0.30	–	10	–	–	N
79	345.384	1.038	0.68	0.3	23	3.5×10^{4}	2.0×10^{22}	N
80	345.548	1.480	0.34	–	11	–	–	Y
81	345.513	0.407	0.82	0.3	27	4.6×10^{4}	2.6×10^{22}	N
82	345.563	1.526	0.36	0.2	12	3.2×10^{4}	1.5×10^{22}	N
83	345.450	1.364	0.34	–	11	–	–	N
84	345.429	1.455	0.88	0.3	29	3.7×10^{4}	2.3×10^{22}	N
85	345.010	1.617	0.45	–	15	–	–	N
86	345.001	1.615	1.2	0.5	41	1.3×10^{4}	1.3×10^{22}	N
87	345.319	1.484	0.68	0.4	22	1.8×10^{4}	1.3×10^{22}	Y
88	345.519	1.639	0.71	0.3	24	4.9×10^{4}	2.5×10^{22}	N
89	345.133	1.069	1.3	0.6	42	7.0×10^{3}	8.4×10^{21}	N
90	345.396	1.519	0.42	–	14	–	–	Y

Continued on next page

Table 3.3 – continued from previous page

Name	Galactic coord. long.	lat.	$S_{1.2mm}$ Jy	Diameter pc	Mass $M_\odot$	Density cm^{-3}	Column density cm^{-2}	Infrared counterpart
91	345.033	1.632	0.76	0.3	25	3.7×10^{4}	2.2×10^{22}	N
92	345.476	1.568	0.31	–	10	–	–	N
93	344.966	1.181	0.41	–	14	–	–	N
94	345.240	0.390	0.49	–	16	–	–	N
95	345.524	0.404	0.46	0.2	15	3.8×10^{4}	1.9×10^{22}	N
96	345.590	0.374	0.40	–	13	–	–	Y
97	345.031	1.781	0.56	0.4	19	9.6×10^{3}	8.0×10^{21}	N
98	345.451	0.435	0.39	–	13	–	–	N
99	345.078	1.786	0.64	0.3	21	1.9×10^{4}	1.3×10^{22}	N
100	345.854	1.415	0.47	–	16	–	–	N
101	345.217	0.999	0.51	0.3	17	1.8×10^{4}	1.2×10^{22}	N
102	344.936	1.596	0.44	–	15	–	–	N
103	345.065	1.615	1.3	0.5	44	1.7×10^{4}	1.5×10^{22}	N
104	345.338	1.463	0.73	0.5	24	8.8×10^{3}	8.2×10^{21}	N
105	345.585	1.484	0.41	0.2	14	3.9×10^{4}	1.8×10^{22}	N
106	345.854	1.421	0.29	–	9.5	–	–	N

Continued on next page

Table 3.3 – continued from previous page

Name	Galactic coord. long.	lat.	$S_{1.2mm}$ Jy	Diameter pc	Mass $M_\odot$	Density cm^{-3}	Column density cm^{-2}	Infrared counterpart
107	345.062	1.842	0.53	0.2	18	5.3×10^{4}	2.4×10^{22}	N
108	345.477	1.563	0.22	–	7.2	–	–	N
109	345.454	1.358	0.16	–	5.4	–	–	N
110	345.959	0.608	0.33	–	11	–	–	N
111	344.949	1.213	0.27	–	8.8	–	–	N
112	344.942	1.589	0.45	–	15	–	–	N
113	345.539	1.488	0.29	0.3	9.5	1.2×10^{4}	7.4×10^{21}	N
114	345.576	0.258	0.26	–	8.5	–	–	N
115	345.681	0.318	0.43	–	14	–	–	N
116	345.330	1.049	0.45	0.2	15	3.9×10^{4}	1.9×10^{22}	N
117	345.776	1.445	0.34	–	11	–	–	N
118	345.511	1.578	0.40	0.3	13	1.6×10^{4}	9.8×10^{21}	N
119	344.909	1.182	0.65	0.3	22	2.6×10^{4}	1.6×10^{22}	N
120	345.518	0.835	0.34	–	11	–	–	N
121	345.873	0.811	0.30	–	10	–	–	N
122	345.489	0.430	0.23	–	7.7	–	–	N

Continued on next page

Table 3.3 – continued from previous page

Name	Galactic coord. long.	lat.	$S_{1.2mm}$ Jy	Diameter pc	Mass $M_\odot$	Density cm^{-3}	Column density cm^{-2}	Infrared counterpart
123	344.951	1.096	0.37	0.2	12	3.7×10^{4}	1.7×10^{22}	N
124	344.906	1.196	0.38	0.2	13	4.5×10^{4}	2.0×10^{22}	N
125	345.092	1.733	0.36	–	12	–	–	N
126	345.261	1.108	0.42	0.3	14	2.1×10^{4}	1.2×10^{22}	N
127	345.467	0.419	0.45	0.2	15	4.8×10^{4}	2.2×10^{22}	N
128	344.801	1.082	0.27	–	8.9	–	–	N
129	345.482	1.233	0.23	–	7.5	–	–	N
130	345.464	1.443	0.21	–	7.0	–	–	Y
131	344.849	1.312	0.24	–	7.9	–	–	N
132	345.484	0.856	0.17	–	5.5	–	–	N
133	345.304	0.435	0.12	–	3.9	–	–	N
134	344.945	1.600	0.64	0.3	21	2.1×10^{4}	1.4×10^{22}	N
135	344.950	1.587	0.22	–	7.3	–	–	N
136	345.272	1.051	0.36	0.3	12	1.7×10^{4}	9.8×10^{21}	N
137	345.060	1.727	0.37	–	12	–	–	N
138	345.479	0.400	0.26	–	8.7	–	–	N

Continued on next page

Table 3.3 – continued from previous page

Name	Galactic coord. long.	lat.	$S_{1.2mm}$ Jy	Diameter pc	Mass $M_\odot$	Density cm^{-3}	Column density cm^{-2}	Infrared counterpart
139	344.846	1.293	0.21	–	7.1	–	–	N
140	345.909	0.514	0.36	0.2	12	3.4×10^{4}	1.6×10^{22}	N
141	345.812	1.756	0.26	–	8.5	–	–	N
142	344.957	1.188	0.24	–	7.9	–	–	N
143	345.320	1.417	0.29	0.4	9.6	7.6×10^{3}	5.5×10^{21}	Y
144	345.869	1.820	0.21	–	6.8	–	–	N
145	345.278	1.112	0.35	0.2	12	2.7×10^{4}	1.4×10^{22}	N
146	345.634	0.770	0.33	0.2	11	3.5×10^{4}	1.6×10^{22}	N
147	345.044	1.618	0.32	0.3	11	2.4×10^{4}	1.2×10^{22}	N
148	344.809	1.075	0.12	–	3.8	–	–	N
149	345.683	1.459	0.30	0.3	9.9	2.2×10^{4}	1.1×10^{22}	N
150	345.566	0.267	0.17	–	5.7	–	–	N
151	344.925	1.316	0.33	–	11	–	–	N
152	345.699	1.508	0.18	–	5.9	–	–	N
153	345.286	0.412	0.14	–	4.6	–	–	N
154	345.611	0.365	0.27	–	8.8	–	–	N

Continued on next page

Table 3.3 – continued from previous page

Name	Galactic coord. long.	lat.	$S_{1.2mm}$ Jy	Diameter pc	Mass $M_\odot$	Density cm^{-3}	Column density cm^{-2}	Infrared counterpart
155	344.916	1.826	0.17	–	5.5	–	–	N
156	345.472	0.412	0.22	–	7.2	–	–	N
157	345.038	1.848	0.28	0.2	9.2	2.9×10^{4}	1.3×10^{22}	N
158	345.792	1.757	0.17	–	5.7	–	–	N
159	345.254	1.012	0.089	–	3.0	–	–	N
160	345.708	1.456	0.24	–	8.0	–	–	N
161	345.472	1.231	0.71	0.4	24	1.3×10^{4}	1.1×10^{22}	N
162	345.497	1.437	0.19	0.3	6.4	8.0×10^{3}	5.0×10^{21}	N
163	344.783	1.105	0.28	–	9.3	–	–	N
164	345.638	0.330	0.11	–	3.7	–	–	N
165	345.699	1.853	0.21	–	7.1	–	–	N
166	344.986	1.109	0.10	–	3.4	–	–	N
167	345.018	1.762	0.17	–	5.7	–	–	Y
168	344.893	1.335	0.45	0.4	15	1.0×10^{4}	7.8×10^{21}	N
169	344.956	1.348	0.47	0.4	16	6.2×10^{3}	5.6×10^{21}	N
170	345.948	0.723	0.14	–	4.5	–	–	N

Continued on next page

Table 3.3 – continued from previous page

Name	Galactic coord. long.	lat.	$S_{1.2mm}$ Jy	Diameter pc	Mass $M_\odot$	Density cm^{-3}	Column density cm^{-2}	Infrared counterpart
171	344.891	1.345	0.20	–	6.6	–	–	N
172	344.924	1.824	0.19	–	6.4	–	–	N
173	344.929	1.610	0.15	–	5.0	–	–	N
174	345.247	0.385	0.18	–	5.9	–	–	N
175	345.547	0.960	0.13	–	4.4	–	–	N
176	344.892	1.847	0.25	–	8.3	–	–	N
177	345.888	1.414	0.26	0.2	8.6	2.3×10^{4}	1.1×10^{22}	N
178	345.510	0.159	0.095	–	3.2	–	–	N
179	345.418	1.469	0.15	0.2	4.8	1.7×10^{4}	7.5×10^{21}	N
180	344.920	1.419	0.17	–	5.5	–	–	N
181	345.079	1.847	0.12	–	4.1	–	–	N
182	345.236	1.000	0.20	–	6.6	–	–	N
183	345.375	1.571	0.14	–	4.7	–	–	N
184	345.684	1.516	0.14	–	4.7	–	–	N
185	345.532	1.634	0.13	–	4.3	–	–	N
186	345.697	1.459	0.19	–	6.1	–	–	N

Continued on next page

Table 3.3 – continued from previous page

Name	Galactic coord. long.	lat.	$S_{1.2mm}$ Jy	Diameter pc	Mass $M_\odot$	Density cm^{-3}	Column density cm^{-2}	Infrared counterpart
187	345.501	1.415	0.23	0.3	7.5	1.6×10^{4}	8.2×10^{21}	N
188	345.816	1.765	0.23	–	7.5	–	–	N
189	345.086	1.611	0.32	0.4	11	5.2×10^{3}	4.4×10^{21}	N
190	345.043	1.838	0.21	0.3	7.0	1.4×10^{4}	7.5×10^{21}	N
191	345.442	1.572	0.11	–	3.8	–	–	N
192	345.468	1.225	0.13	–	4.2	–	–	N
193	344.951	1.082	0.34	0.3	11	9.6×10^{3}	6.7×10^{21}	N
194	345.482	0.431	0.27	0.3	8.8	1.9×10^{4}	9.8×10^{21}	N
195	344.913	1.165	0.13	–	4.4	–	–	N
196	344.933	1.820	0.17	–	5.7	–	–	N
197	345.458	1.559	0.13	0.2	4.5	1.1×10^{4}	5.3×10^{21}	N
198	345.792	1.440	0.096	–	3.2	–	–	N
199	345.098	1.726	0.11	–	3.7	–	–	N
200	345.293	1.093	0.14	–	4.5	–	–	N
201	344.991	1.150	0.11	–	3.8	–	–	N

3.4 Physical properties of clumps

First, we estimate the minimum gas column density that can be detected given the rms noise of our observations. Assuming that 1.2 mm continuum emission is optically thin and produced by dust, the column density N is (Hildebrand 1983)

$$N = \frac{S_{1.2\,mm}\, R_{gd}}{\Omega\, \mu\, m_H\, k_{1.2\,mm}\, B_{1.2\,mm}(T_{dust})}, \tag{3.1}$$

where Ω is the beam solid angle, $S_{1.2\,mm}$ is the flux density at 1.2 mm, μ is the mean mass per particle, equal to ~2.29 for an H_2 cloud with a 25% contribution of helium (Evans 1999), m_H is the hydrogen atom mass, $k_{1.2\,mm}$ is the dust absorption coefficient at 1.2 mm, equal to ~1 $cm^2\ g^{-1}$ for protostellar cores (Ossenkopf & Henning 1994), $B_{1.2\,mm}(T_{dust})$ is the Planck function at both 1.2 mm and a dust temperature T_{dust}, equal to ~30 K for regions of massive-star formation (Faúndez et al. 2004), and R_{gd} is the ratio of gas to dust mass, ~100 (Hildebrand 1983). For a solid angle limit of 24″×24″ and an intensity limit of five rms, ~0.1 Jy $beam^{-1}$, the minimum flux density is ~88 mJy and the minimum column density that can be detected is ~4x10^{21} cm^{-2}, which corresponds to a visual extinction of 4 mag, assuming that $N_{H_2}/A_V \sim 10^{21} cm^{-2}\ mag^{-1}$ (Bohlin et al. 1978).

Masses of clumps, M_c, are estimated as

$$M_c = \int \mu\, m_H N dA = \frac{S_{1.2\,mm}\, R_{gd}\, d^2}{B_{1.2\,mm}(T_{dust})\, k_{1.2\,mm}},$$

where dA is the differential element of area (dA= d^2 dΩ) and d is the distance to the GMC (~1.8 kpc). Since we insist that identified clumps have intensities and dimensions greater than 0.1 Jy $beam^{-1}$ and 24″×24″ respectively, the lower limit to their masses is ~2.9 $M_\odot$. The derived masses of clumps range from 3.0 to 1.3×10^3 $M_\odot$, with a total mass of 1.2x10^4 $M_\odot$ (see Tables 3.4 and 3.3). The efficiency in forming these clumps, estimated as the ratio of the total clump mass to the total GMC mass, is thus ~0.02.

The clump mass distribution (CMD) is shown in Fig. 3.6, plotted as $dN/d\log(M/M_\odot)$ versus mass, where $dN/d\log(M/M_\odot)$ is approximated by the number of clumps, ΔN, within a logarithmic mass interval $\Delta\log(M/M_\odot)$. In this figure, $\Delta\log(M/M_\odot)$ is constant,

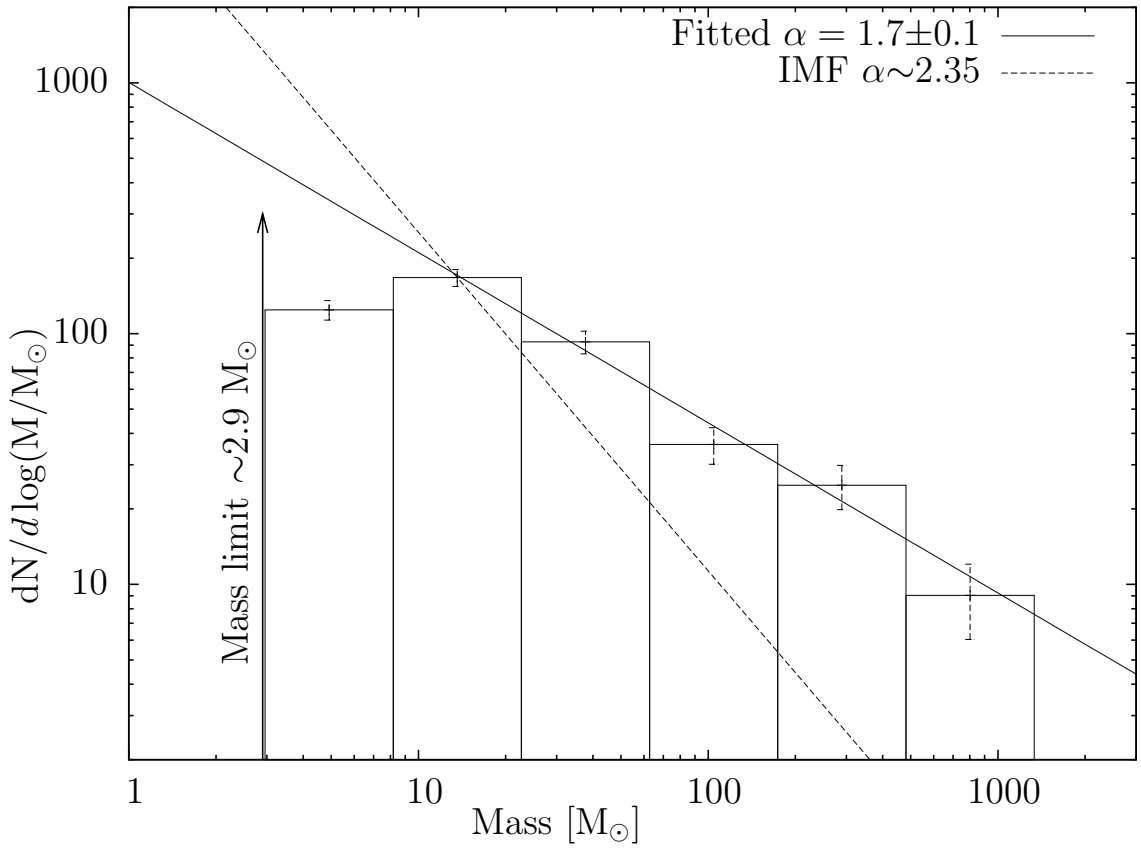

Figure 3.6: Mass distribution of identified clumps in G345.5+1.0, plotted as dN/dlog(M/$M_\odot$) versus mass, where dN/dlog(M/$M_\odot$) is approximated by the number of clumps ΔN within a logarithmic mass interval $\Delta\log(M/M_\odot)$. Here, $\Delta\log(M/M_\odot)$ is constant,~0.44. Error bars are estimated by $\sqrt{\Delta N/\Delta\log(M/M_\odot)}$. The arrow shows the clump mass limit, ~2.9 $M_\odot$. The continuous line represents the mass distribution fit with $dN/d\log(M/M_\odot)\propto M^{1-\alpha}$, where the spectral mass index α is 1.7±0.1 for masses between ~10 and 1.3x10^3 $M_\odot$. The dashed line displays the spectral mass index for the stellar initial mass function (IMF) of the solar neighborhood for stellar masses greater than 0.5 $M_\odot$ (e.g. Kroupa 2002); the line is forced to pass through the peak of the clump mass distribution.

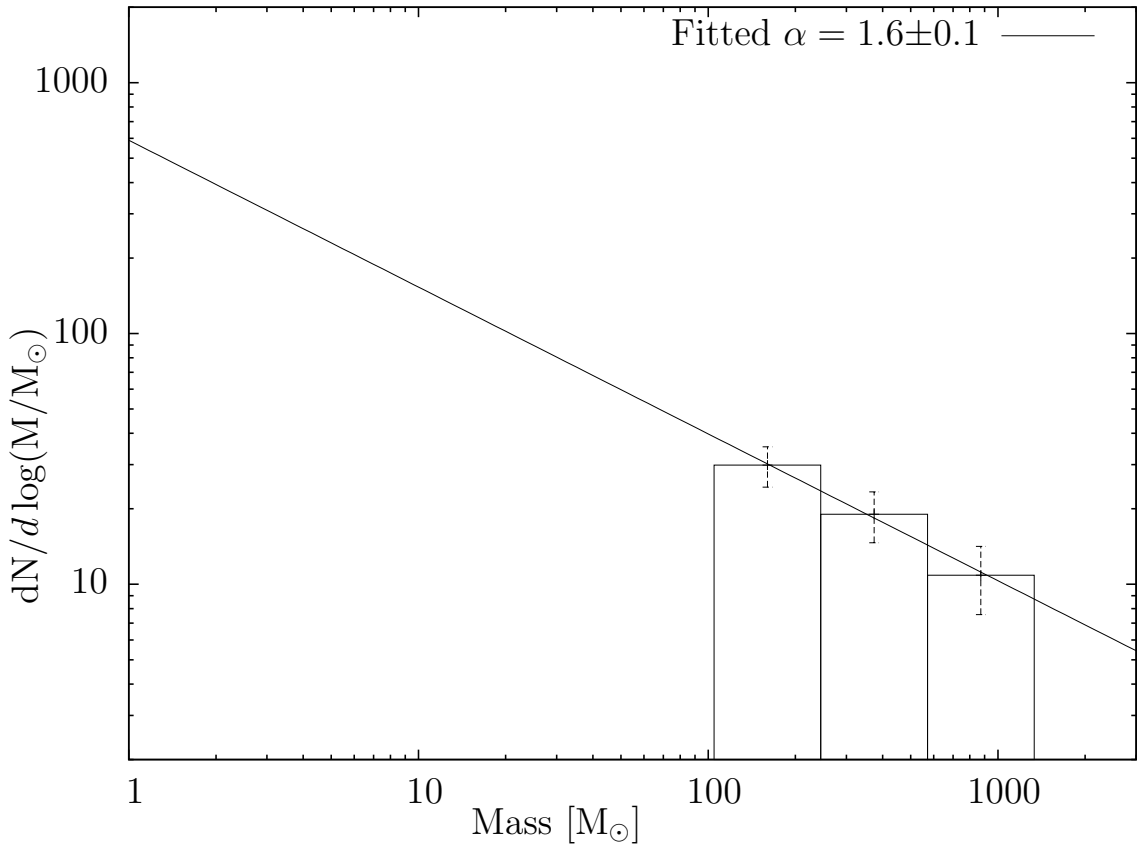

Figure 3.7: Mass distribution of identified clumps in G345.5+1.0 with masses higher than 100 $M_\odot$, plotted as dN/dlog(M/$M_\odot$) versus mass, where dN/dlog(M/$M_\odot$) is approximated by the number of clumps ΔN within a logarithmic mass interval Δ log(M/$M_\odot$). Here, Δ log(M/$M_\odot$) is constant,~0.37. Error bars are estimated by $\sqrt{\Delta N/\Delta \log(M/M_\odot)}$. The continuous line represents the mass distribution fit with $dN/d\log(M/M_\odot) \propto M^{1-\alpha}$, where the spectral mass index α is 1.6±0.1 for masses between ~100 and 1.3x10^3 $M_\odot$.

at a value of ~0.44. The CMD is well-fitted by a power law $dN/d\,log(M) \propto M^{-\alpha+1}$, which can be expressed as $dN/dM \propto M^{-\alpha}$, with the spectral mass index, α, equal to 1.7±0.1 for masses between ~10 and 1.3x10^3 $M_\odot$. The correlation coefficient of the fit is 0.993. Between 10 $M_\odot$ and 1.3x10^3 $M_\odot$, bin size variations of $\Delta \log(M/M_\odot)$ between 0.18 and 1.1 result in values of α consistent with 1.7±0.1. Since α is 1.7, the population is dominated by clumps with low masses, but the total mass is dominated by the most massive clumps; for example, 50% of the population is between 10 and 27 $M_\odot$, but contains only 10% of the total mass. The turnover below ~10 $M_\odot$ is produced by an incompleteness of the clump catalog caused by the combination of the spatial resolution and flux density limit of the survey. However, observations of higher spatial resolution ($\lesssim$0.01 pc) could result in a spectral mass index of ~2.35, resolving core structures (e.g. Motte et al. 1998). Beltrán et al. (2006) studied a sample of IRAS sources associated with MSFRs in 1.2 mm continuum and found a spectral mass index of 1.5 for clumps with masses between ~10 $M_\odot$ and 10^2 $M_\odot$ and 2.1 for clumps with masses between ~10^2 and 10^4 $M_\odot$. For clumps identified here with masses higher than 100 $M_\odot$, we find a spectral mass index of 1.6±0.1, as is shown in Fig. 3.7, in agreement with the previous fit considering clumps with masses between 10 and 1.3×10^3 $M_\odot$. It is necessary to observe more whole GMCs to confirm these results.

Clump diameters, D_c, are estimated from the deconvolved FWHM size of their emissions. We used the FWHM size θ_{FWHM} estimated by CLUMPFIND algorithm, thus

$$D_c = \sqrt{\theta^2_{FWHM} - \theta^2_{beam}},$$

where θ_{beam} is the beam-size. Considering a distance of 1.8 kpc to the GMC and clumps that have a reliable D_c, i.e. $D_c \geq \theta_{beam}$, clumps have diameters between 0.2 and 0.6 pc.

From the masses and sizes, and assuming a spherical and homogeneous density distribution, we estimate mean clump densities, using the expression

$$\rho = \mu\, m_H\, n,$$

where ρ is the mass density and n is the particle density. Densities of clumps are between

Table 3.4: Summary of the physical properties of the identified clumps.

	$S_{1.2\,mm}$ Jy	Diameters pc	Masses $M_\odot$	[a]Densities cm^{-3}
Range	0.089-40	0.2-0.6	3.0-1.3×10^3	5×10^3-4×10^5
Total	3.7×10^2		1.2×10^4	

[a] The densities are computed assuming a mean molecular weight of μ=2.29.

5×10^3 and 4×10^5 cm^{-3}. Mean column densities of clumps, N_c, are estimated as

$$N_c \sim \frac{M_c}{\mu\, m_H\, \pi (D_c/2)^2},$$

and range between 4×10^{21} and 4×10^{23} cm^{-2}. Tables 3.4 and 3.3 show physical properties for each clump and a summary of them, respectively.

Figure 3.8 shows a plot of mass versus diameter for the clumps detected toward GMC G345.5+1.0 with reliable diameters. The dotted lines indicate constant densities at 10^3, 10^4, 10^5, and 10^6 cm^{-3}. The majority of clumps have densities between 10^4 and 10^5 cm^{-3}.

The physical properties of detected clumps are similar to those found in other GMCs (e.g. Mookerjea et al. 2004).

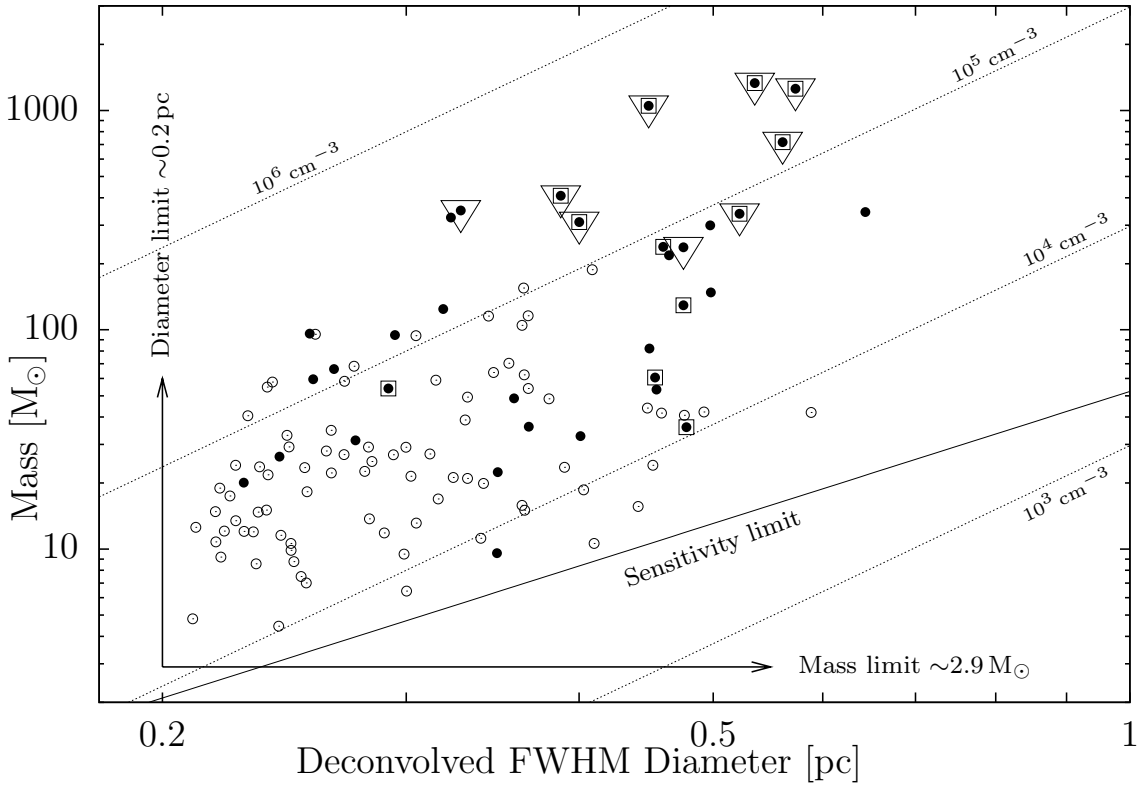

Figure 3.8: Mass versus diameter for the clumps detected toward the GMC G345.5+1.0 in 1.2 mm continuum emission with reliable diameters. Filled circles indicate clumps detected in infrared MSX and SPITZER bands. Open circles indicate clumps that do not have an infrared counterpart. Triangles indicate clumps associated with MSFR-IRAS sources, which have luminosities $>10^3\,L_\odot$. Boxes indicate clumps associated with MSX sources that satisfy MYSO candidate criterion (Lumsden et al. 2002). Arrows mark detection limits for masses (~2.9 $M_\odot$) and diameters (~0.2 pc). The continuous line indicates the detectable mass as a function of diameter (sensitivity limit), considering an intensity limit of five rms (~0.1 Jy beam^{-1}). Dotted lines indicate mean densities at 10^3, 10^4, 10^5 and 10^6 cm^{-3}. The densities are computed assuming a mean molecular weight of μ=2.29.

3.5 Association with infrared emission (IRAS - MSX - SPITZER)

Stars form in clumps, heating their surrounding dust, which re-radiates at infrared wavelengths. This is illustrated in Fig. 3.9 that shows a strong spatial correlation between the 1.2 mm continuum emission and infrared emission at 21.34 μm (from MSX observations). To quantify the correlation, we searched for infrared emission inside clump emission areas, using MSX[2] images at 8.28, 12.13, 14.65, and 21.34 μm and SPITZER[3] (IRAC) images at 3.6, 4.5, 5.8, and 8.0 μm. We find that ~20% of all clumps have an infrared counterpart in all MSX and SPITZER bands (see Table 3.3). The rest of the clumps, ~80%, are not detected in all MSX and SPITZER bands, particularly not in 12.13, 14.65, and 21.34 μm. Since 8.0 μm MSX band and SPITZER IRAC bands are sensitive to the polycyclic aromatic hydrocarbon (PAH) emission and the photospheric emission from stars (e.g. Chavarría et al. 2008), clump not detected in all MSX and SPITZER bands are considered to have no counterpart at infrared wavelengths. Since both the MSX and SPITZER bands have sensitivity limits, the percentage of detections is a lower limit to the number of clumps that are forming stars, and the percentage of failed detections is an upper limit to the number of clumps that are not forming stars.

Nine clumps are associated with six IRAS point sources classified as MSFRs with luminosities $\gtrsim 10^3$ $L_\odot$ (see Sect. 3.6 and Table 3.5). As Fig. 3.8 shows, these clumps have densities of $\sim 10^5$ cm^{-3}, suggesting that there is a threshold density above which massive stars can form. These values are consistent with the typical density of clumps associated with MSFRs ($\sim 10^5$ cm^{-3}; Faúndez et al. 2004).

As Fig. 3.8 shows, clumps that emit detectable infrared emission tend to be more massive than remaining clumps. Clumps without infrared emission (cold or starless clumps) have a mean mass of 21 $M_\odot$, and clumps with an infrared counterpart have a mean mass of 2.1×10^2 $M_\odot$. Furthermore, all clumps with masses higher than ~200 $M_\odot$ have an infrared counterpart.

[2] http://irsa.ipac.caltech.edu/
[3] http://irsa.ipac.caltech.edu/

MSX point sources associated with clumps within the GMC G345.5+1.0 have mid-infrared colors S_{21}/S_8 from 0.9 to 30, S_{14}/S_8 from 0.4 to 8, and S_{12}/S_8 from 0.7 to 4, where S_8, S_{12}, S_{14}, and S_{21} are the flux densities at 8.28, 12.13, 14.65, and 21.34 μm, respectively. These ratios cover those of massive young stellar objects (MYSOs; Lumsden et al. 2002): $S_{21}/S_8 > 2$ and $S_{21} > S_{14} > S_8$. About 7% of the clumps contain MSX sources that satisfy this criterion, and these clumps have masses $\gtrsim$36 $M_\odot$ (see Fig. 3.8).

The existence of clumps with and without infrared emission suggests that clumps in the GMC are at different evolutionary stages. Cold clumps have masses between 3.0 and 1.9×10^2 $M_\odot$, where the most massive ones are possible progenitors of MSFRs. For example, we estimate that the least massive clump associated with a MYSO has a mass of $\sim$36 $M_\odot$, and we identify seven cold clumps with densities $\gtrsim10^5$ cm^{-3} and masses $\gtrsim$36 $M_\odot$, which will eventually collapse to form high-mass stars.

Do clumps form single stars? One way to assess this is to compare the slope of the clump mass distribution with that of the stellar initial mass function (IMF) (e.g. Motte et al. 1998; Lada et al. 2007). Equal slopes would indicate that the origin of the stellar IMF has its direct roots in the origin of the clump mass distribution. The spectral mass index α of the clump mass distribution determined here is consistent with that of other investigations (e.g. Muñoz et al. 2007), but differs from that estimated for the stellar IMF of the solar neighborhood for stellar masses higher than 0.5 $M_\odot$ ($\alpha\sim$2.35; e.g. Kroupa 2002). This suggests that the detected clumps do not directly form stars, and other processes are necessary to determine the stellar initial masses, such as the fragmentation of clumps, mainly of the most massive ones. Figure 3.6 compares the IMF spectral mass index with the clump mass distribution.

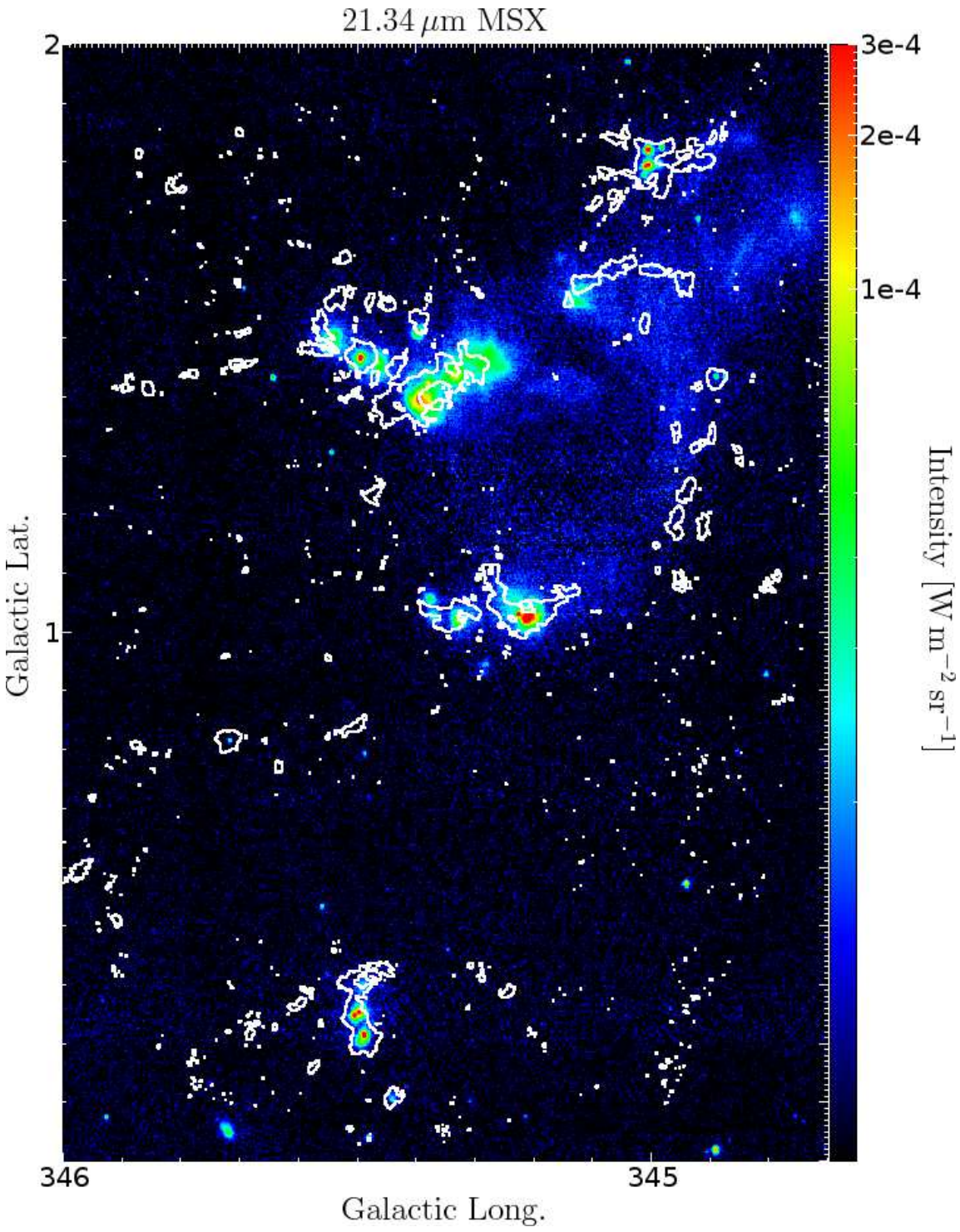

Figure 3.9: Image in 21.34 μm from MSX observations toward GMC G345.5+1.0 with contours of 1.2 mm continuum emission at three times rms, ~0.06 Jy beam^{-1}.

3.6 Dust properties of massive star forming regions associated with clumps and IRAS point sources

Regions of massive star formation are embedded in massive clumps, and the intense Lyman flux produced by them heats the surrounding dust, which re-emits mainly at far infrared wavelengths with characteristic colors. To study the physical properties of dust in these regions, we examine the spectral energy distributions (SEDs) of MSFRs associated with IRAS point sources and clumps detected here, assuming that their emissions are from dust.

Within the GMC, there are eight MSFRs associated with IRAS-CS sources (Table 3.2). We added one more source, IRAS 16533-4009, which is embedded in 1.2 mm continuum emission, has a high luminosity, $\sim 9\times10^4$ $L_\odot$, and increasing IRAS flux densities from 12 to 100 μm; however it does not satisfy the far-infrared color criterion defined by Wood & Churchwell (1989), since its flux density in 25 μm is an upper limit. Figure 3.10 shows 8.0 μm images from SPITZER data with contours of 1.2 mm continuum emission for all these sources. For six of these objects, the SPITZER emission is embedded within 1.2 mm continuum emission. For more reliable estimates in our SED study, we only consider these six sources: IRAS 16533-4009, IRAS 16562-3959, IRAS 16571-4029, IRAS 16596-4012, IRAS 17008-4040, and IRAS 17009-4042.

Figure 3.11 displays the six SEDs constructed using our observations in 1.2 mm continuum emission, infrared data at 12, 25, 60, and 100 μm from the IRAS Point Source Catalog (version 2.0), and at 8.3, 12.1, 14.7 and 21.3 μm from the MSX Point Source Catalog (version 2.3). Because observations were performed using different beam sizes, for IRAS $\sim$300″, for MSX $\sim$20″, and for 1.2 mm 24″, we consider all emission within the IRAS beam; thus, two SEDs are associated with more than one 1.2 mm clump.

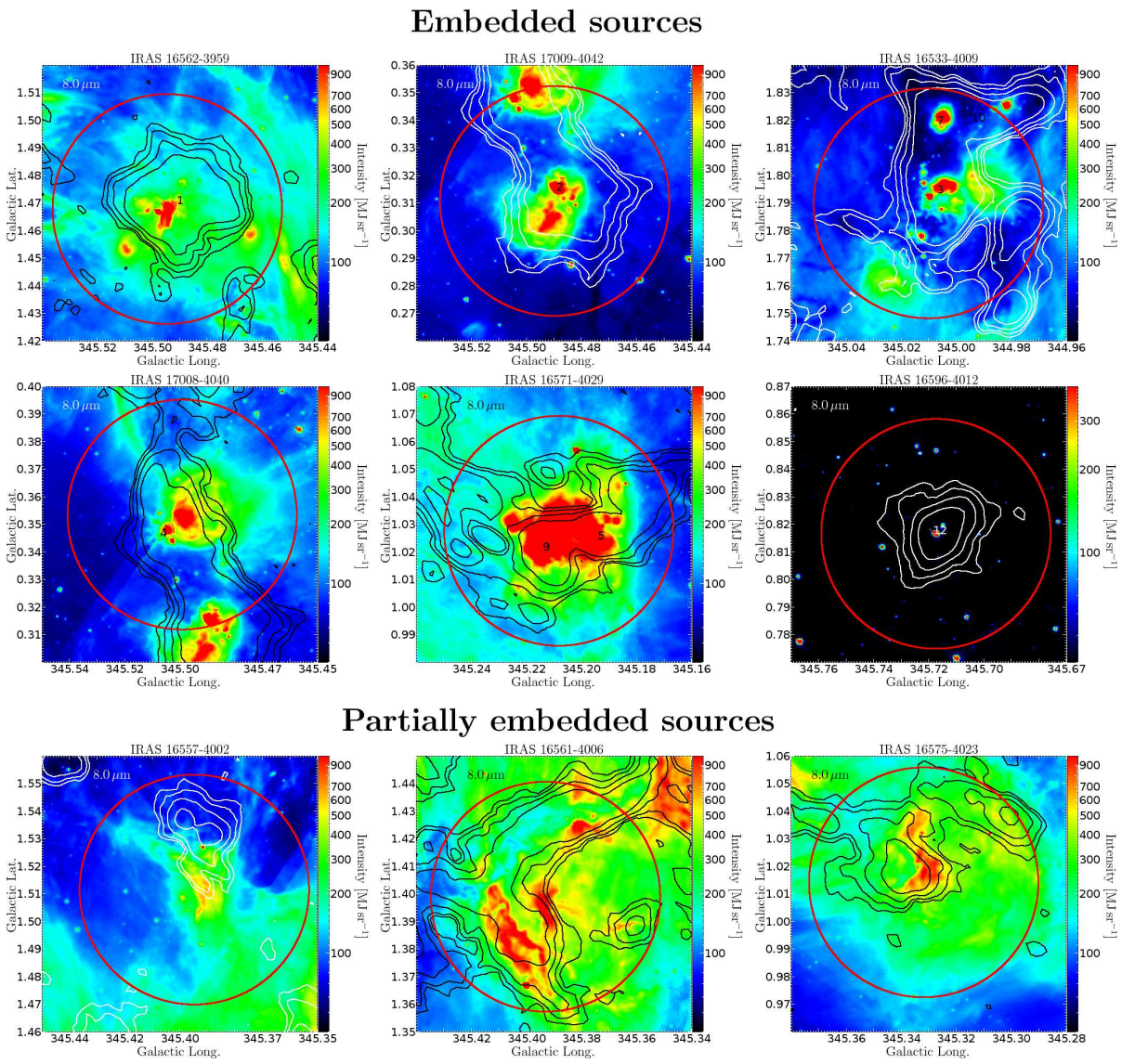

Figure 3.10: Images of 8.0 μm emission (SPITZER data) toward clumps detected in 1.2 mm continuum emission and associated with IRAS point sources. Contours represent 1.2 mm continuum emission at 0.06, 0.12, 0.24, and 0.48 Jy beam^{-1} (rms is 0.02 Jy beam^{-1}). IRAS source names are given at the top of each image, and clump numbers are indicated at the peak of 1.2 mm continuum emission. Red circles are centered on the coordinates of IRAS point sources, with diameters of 5′ (an approximation of the angular resolution of IRAS observations at 100 μm).

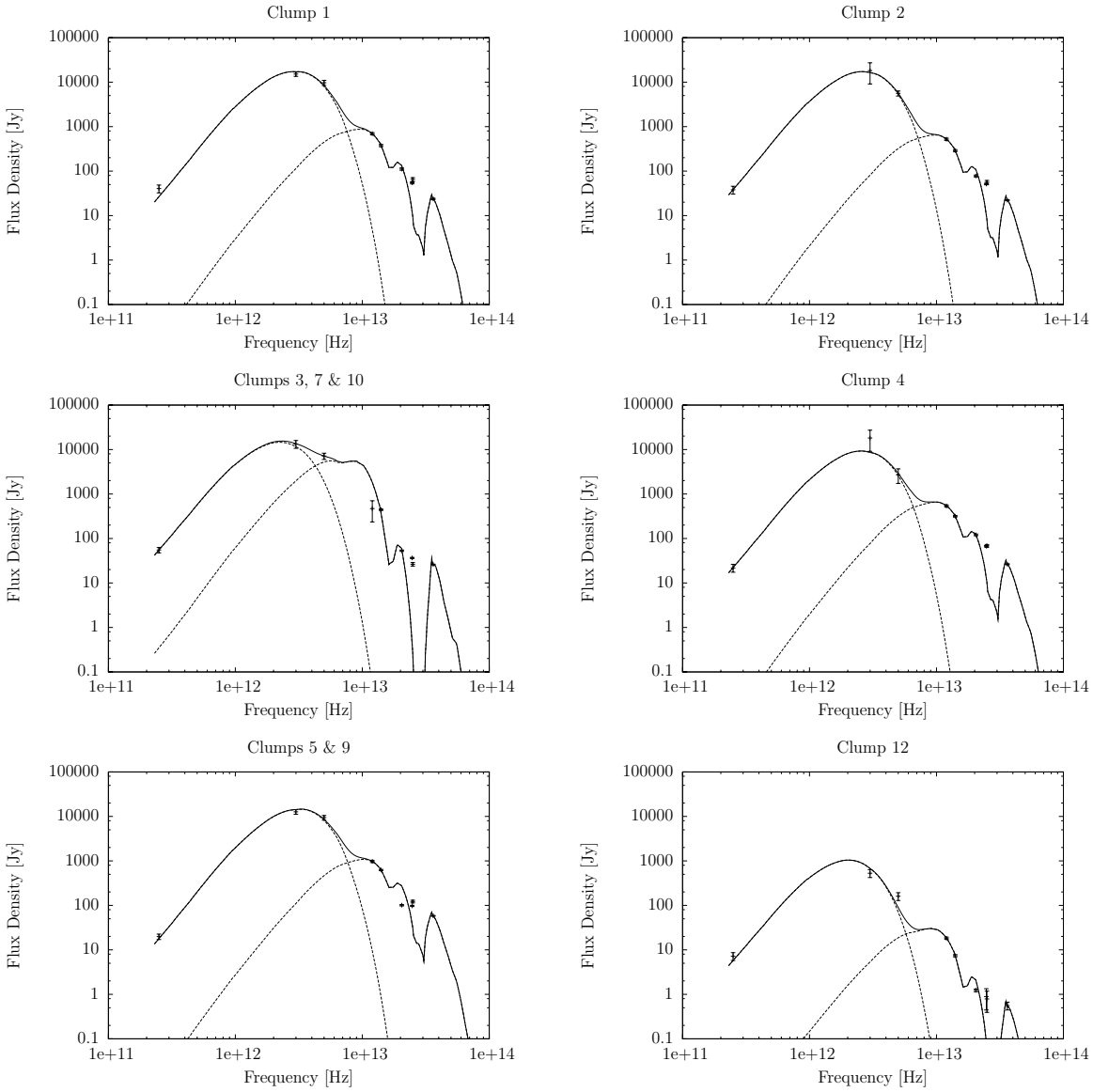

Figure 3.11: The SEDs of massive-star forming regions associated with massive clumps detected in 1.2 mm continuum emission; top labels show names of the clumps. Dots with error bars are flux densities estimated from SIMBA, IRAS, and MSX observations. Each SED is modeled with two dust components at different temperatures (physical parameters for each model are in Table 3.5); drawn lines are the total flux density of the two dust components, and dashed lines are the contributions of each dust component.

The SEDs of MSFRs can be modeled as several dust components at different temperatures (e.g. Faúndez et al. 2004; Morales et al. 2009). Because of the shape of the six SEDs, we model them as two dust components at different temperatures, cold and warm components, including the absorption of the radiation by assuming that the warm component is embedded in the cold one. The total flux density, S_ν^{total}, at frequency ν is approximated by

$$S_\nu^{total} \sim S_\nu^{cold} + S_\nu^{warm},$$

where

$$S_\nu^{cold} = \Omega^{cold} B_\nu(T_{dust}^{cold})(1 - \exp(-\tau_\nu^{cold}))$$

and

$$S_\nu^{warm} = \Omega^{warm} B_\nu(T_{dust}^{warm})(1 - \exp(-\tau_\nu^{warm})) \exp(-\tau_\nu^{cold}/2).$$

The parameters S_ν^{cold}, Ω^{cold}, T_{dust}^{cold}, and τ_ν^{cold} are the flux density, the solid angle, the dust temperature, and the optical depth of the cold component, respectively, and S_ν^{warm}, Ω^{warm}, T_{dust}^{warm}, and τ_ν^{warm} are the flux density, the solid angle, the dust temperature, and the optical depth of the warm component, respectively. In addition, $B_\nu(T_{dust}^{cold})$ and $B_\nu(T_{dust}^{warm})$ are the Planck function at dust temperatures T_{dust}^{cold} and T_{dust}^{warm}, respectively. For both components, Ω can be expressed as

$$\Omega = \pi\,(\theta/2)^2\,,$$

where θ is the angular diameter. The optical depths are given by (e.g. Evans 1999)

$$\tau_\nu^{cold} = N_{dust}^{cold}\, k_\nu \quad and \quad \tau_\nu^{warm} = N_{dust}^{warm}\, k_\nu,$$

where N_{dust}^{cold} and N_{dust}^{warm} are the dust column densities in $\mathrm{g\,cm^{-2}}$ for the cold and warm components, and k_ν is the dust opacity. We use dust opacities estimated by Ossenkopf & Henning (1994) for protostellar cores. They computed opacities considering the Mathis-Rumpl-Nordsieck (MRN) distribution for the diffuse interstellar medium (Draine & Lee 1984) as the initial size distribution for dust, without and with ice (thin and thick), and without and with coagulation (after 10^5 years for densities between 10^5-$10^8\,\mathrm{cm^{-3}}$). In the case of regions with ice depletion produced by the heating of central sources, they recommended opacities for the model with thin ice mantles and coagulation for a density of $10^5\,\mathrm{cm^{-3}}$. These dust opacities are shown in Fig. 3.12, for frequencies between $\sim 2.3\times10^{11}$ and 10^{14} Hz.

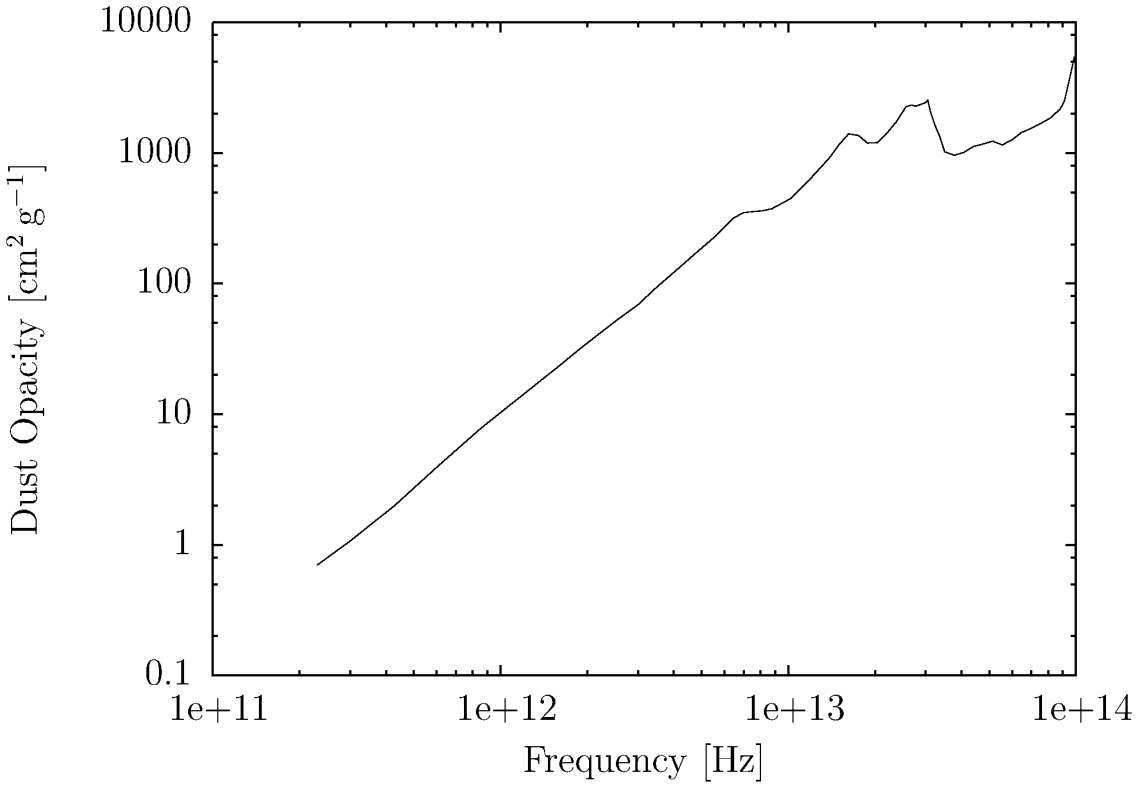

Figure 3.12: Dust opacity spectrum utilized in the SED models. It was estimated by Ossenkopf & Henning (1994)[a], assuming a Mathis-Rumpl-Nordsieck initial size distribution with thin ice mantles and 10^5 yr of coagulation at a gas density of 10^5 cm^{-3}.

[a] http://vizier.u-strasbg.fr/viz-bin/VizieR, J/A+A/291/943/table1

Thus, in our SED model, each dust component has three values to fit of T_{dust}, θ, and N_{dust}. However, the dust column density of the warm component, N_{dust}^{warm}, is difficult to estimate, because it is more sensitive to the emission in the Rayleigh-Jeans part of the spectrum ($h\nu << k\,T_{warm}$), where the emission is dominated by the cold component. To overcome this problem, we assume that the two components have equal densities, thus

$$N_{dust}^{warm} \sim \frac{\theta_{dust}^{warm}}{\theta_{dust}^{cold}} N_{dust}^{cold}.$$

Given the simplicity of the SED model and the poor sensitivity of the data to N_{dust}^{warm}, a more realistic density distribution is unnecessary.

To enable a more reliable comparison, angular diameters are converted into spatial

diameters, and dust column densities to gas column densities. Thus

$$D_{dust}^{cold} = d\,\theta_{dust}^{cold},$$

$$D_{dust}^{hot} = d\,\theta_{dust}^{warm},$$

and

$$N_{gas}^{cold} = \frac{N_{dust}^{cold} R_{gd}}{\mu\, m_H},$$

where θ_{dust}^{cold} and θ_{dust}^{warm} are in radians. In this way, our model has five variables: dust temperatures and sizes for the two components, and gas column density for the cold component.

Table 3.5 and Fig. 3.11 display the results of the fits. The mean dust temperatures of each component are 28±5 K (cold) and 200±10 K (warm). The sizes and column densities of the cold component agree with those estimated by 1.2 mm continuum: sizes vary by a factor of 0.7-1.5 and column densities vary by a factor of 0.5-3. Estimates of luminosities, from the integration of SED models, are $>10^3\,L_\odot$. Given the sizes and column densities, the total mass is dominated by the cold component (~99% of the total mass), and is similar to that estimated from the 1.2 mm continuum emission, varying by a factor of 0.8-1.6.

Dust characteristics of clumps associated with MSFRs estimated in this paper are consistent with previous works (e.g. Faúndez et al. 2004; Molinari et al. 2000; Molinari et al. 2008), where the cold dust temperature in regions of massive star formation is ~30 K.

The SED models have a discrepancy with data in ~12 μm bands (see Fig. 3.11), which can be produced by not considering the PAH emission in the SED models (e.g. van Dishoeck 2004), or by an excess in the dust opacities utilized at these wavelengths, affecting the modeled radiation from the hot component that is absorbed by the cold one.

The dependence of SED models on variations in the fitted parameters is shown in Fig. 3.13, which displays the SED for clump 1, or IRAS 16562-3959, with the best-fit model and models with variations in the fitted parameters T_{dust}^{cold}, D_{dust}^{cold}, T_{dust}^{warm}, D_{dust}^{warm}, and N_{gas}^{cold}. For each dust component, variations in its temperature affect both its peak emission frequency and its luminosity, both values increasing as the temperature increases. Variations in either D_{dust}^{cold} or N_{gas}^{cold} affect the luminosities of the two components; when D_{dust}^{cold}

or N_{gas}^{cold} increases, the luminosity of the cold dust component increases, whereas radiation absorption of the warm component also increases, reducing its luminosity. When D_{dust}^{warm} increases, the luminosity also increases.

Table 3.5: SED models for MSFRs associated with IRAS point sources and massive clumps detected in 1.2 mm continuum emission. Each model consists of two dust components with equal densities at different temperatures (cold and warm components). Column 1 shows names of IRAS point sources; Column 2, names of clumps; in Columns 3 to 8, we show the fitted physical parameters: dust temperature, diameter, and column density, respectively, for the cold (Cols. 3-5) and warm (Cols. 6-8) components; Column 9, masses of the cold component; and Column 10, total luminosities.

IRAS	Clumps	Cold			Warm			Cold mass	Luminosity
		T_{dust}	D_{dust}	N_{gas}	T_{dust}	D_{dust}	N_{gas}		
		K	pc	10^{23} cm^{-2}	K	pc	10^{22} cm^{-2}	10^3 M$_\odot$	10^4 L$_\odot$
16562-3959	1	32	0.67	1.6	194	0.03	0.69	1.0	5.3
17009-4042	2	29	0.86	1.6	202	0.03	0.51	1.7	4.7
16533-4009	3, 7, 10	25	0.79	3.2	205	0.07	2.7	2.8	9.4
17008-4040	4	28	0.68	1.5	205	0.03	0.57	1.0	2.9
16571-4029	5, 9	34	0.58	1.3	209	0.03	0.65	0.64	5.3
16596-4012	12	22	0.34	2.2	203	0.008	0.49	0.36	0.22

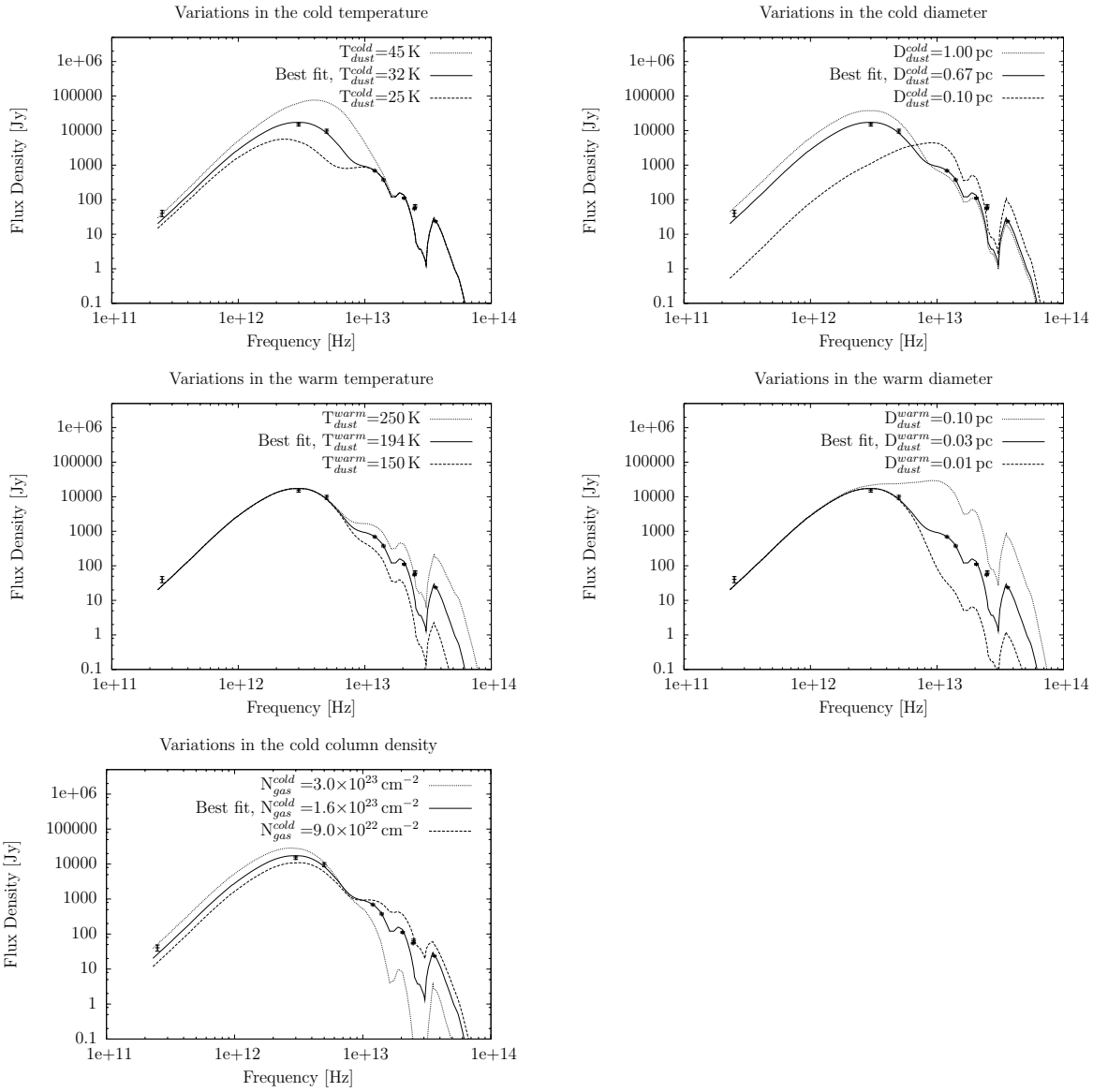

Figure 3.13: Dependence of the SED model on variations in the fitted parameters. Plots show the SED for clump 1 with the best-fit model (see Table 3.5) and variations in each parameter, for T^{cold}_{dust}, D^{cold}_{dust}, T^{warm}_{dust}, D^{warm}_{dust} and N^{cold}_{gas}, when increasing and decreasing the best-fit value.

Chapter 4

G345.45+1.50: An expanding ring-like structure with massive star formation

4.1 ^{13}CO(3-2) line emission

Figure 4.1 shows the average spectrum of the ^{13}CO(3-2) line toward the ring. The emission is concentrated between -30 and -2 km s^{-1}, with two gas components; the strongest one peaks at -12.4 km s^{-1} and the weakest one peaks at -25 km s^{-1}. The velocity range of the ^{13}CO(3-2) line emission is in agreement with the ring being part of the GMC G345.5+1.0, which is defined between -33 and -2 km s^{-1}. The two velocity components observed in the ^{13}CO(3-2) line where previously identified in ^{12}CO(1-0) line (Bronfman et al. 1989), and the strongest one in the CS(2-1) line (Bronfman et al. 1996).

The spatial distribution of the velocity integrated ^{13}CO(3-2) line is shown in Fig. 4.2 through of the two components, integrating between -26 and -24 km s^{-1}, and between -22 and -2 km s^{-1}. The spatial structure of the strongest component, which contains the majority of the emission, is composed by several condensations that form the ring-like shape. The weakest component corresponds to a condensation.

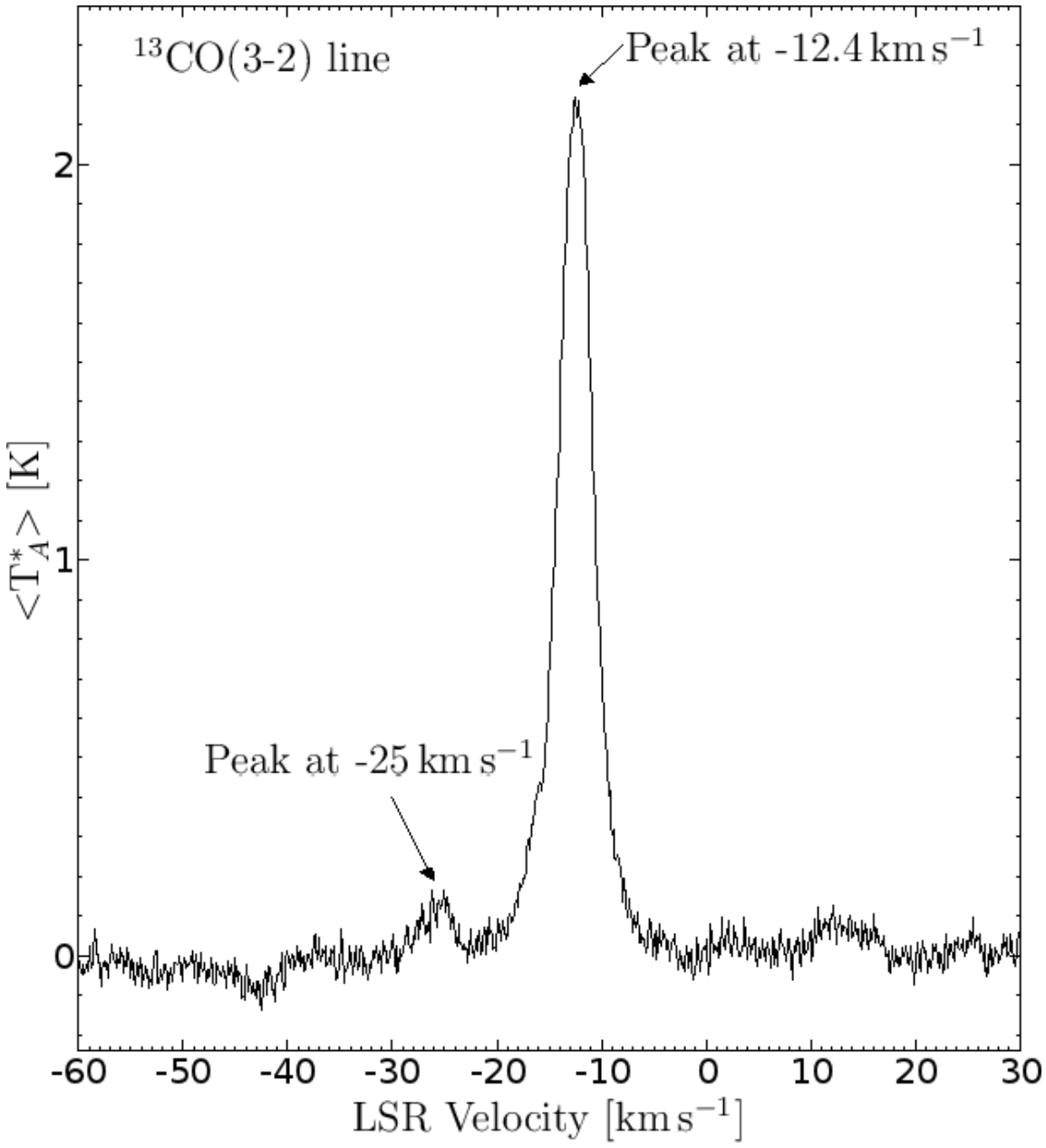

Figure 4.1: Average spectrum of the ^{13}CO(3-2) line toward the ring-like structure G345.45+1.50. Arrows indicate the two peaks in the emission.

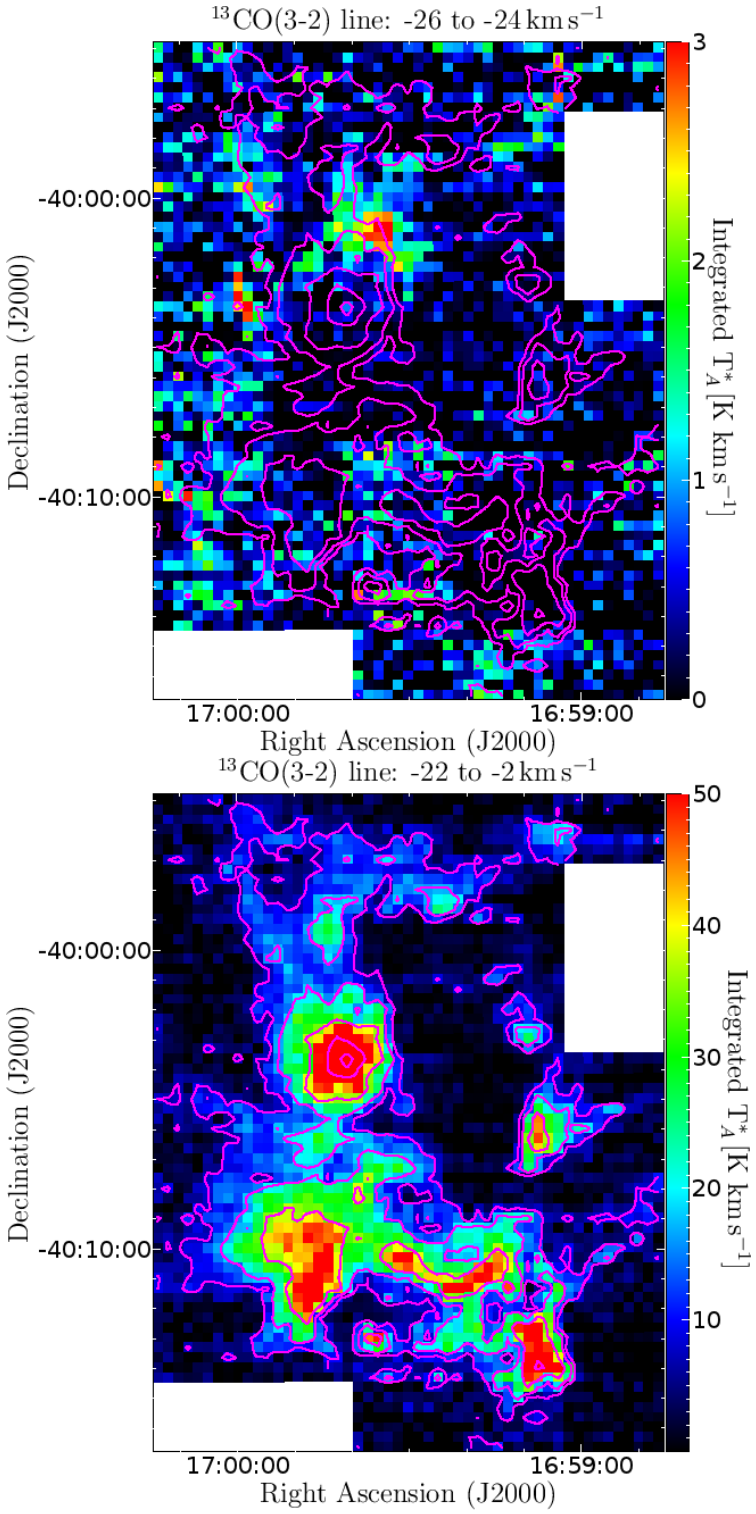

Figure 4.2: Integrated velocity ^{13}CO(3-2) line emission from the ring G345.50+1.50 between -26 and -24 km s^{-1} (top image), and between -22 and -2 km s^{-1} (bottom image). Contours show the emission integrated between -30 and -2 km s^{-1} with levels of 9, 18, 36, 72 and 144 K km s^{-1}.

It is possible to distinguish different stages in the process to form stars along the ring comparing the ^{13}CO(3-2) line with 1.2 mm continuum emission, SPITZER, MSX and Molonglo Galactic Plane Survey (MGPS; Murphy et al. 2007) observations. The ^{13}CO(3-2) line emission delineates the cold dust structure traced in 1.2 mm continuum emission (Fig. 4.3), following the same ring-like structure. These cold gas and dust components wrap the emission generated by hot dust heated by embedded stars, which is observed in the MSX and SPITZER bands (see Fig. 4.4). Cold condensations, regions with ^{13}CO(3-2) line emission or 1.2 mm continuum emission without an infrared counterpart, mainly in 21.34 μm MSX band. These are regions where stars could be eventually formed.

Figure 4.4 shows an image in 35.6 cm continuum emission from MGPS, displaying the HII regions. These HII regions have a counterpart at infrared wavelengths. However, J165920-400424, a 35.5 cm source from MGPS located at RA=16:59:20.73 Dec=-40:04:24.7(J2000), does not have a clear infrared counterpart, being possibly an pulsar produced by a supernova explosion (see Sect. 4.8.1). Other possibilities are an extragalactic source, radio star or planetary nebulae (e.g. Whiteoak et al. 1992). To reveal the nature of this source, we looked for objects at its position in NED (http://ned.ipac.caltech.edu/) and Vizier (http://vizier.u-strasbg.fr/viz-bin/VizieR) databases. No object is found within 2 arcmin in NED, and only stellar objects are found in Vizier within 25 arcsec, approximately half of the beam-size of the MGPS observations. To clarify the nature of this source, we will propose ATCA observations toward J165920-400424 in cm wavelengths.

Features at 7.7 and 8.6 μm attributed to vibrational emission of polycyclic aromatic hydrocarbons (PAHs) excited by UV radiation (e.g. van Dishoeck 2004) are observed in the 8.0 μm SPITZER band, while 4.5 μm SPITZER band contains no PAH features and thereby monitors the continuum emission (Benjamin et al. 2003). However, features shown in 8.0 and 4.5 μm bands toward the ring are roughly similar, where 8.0 μm band delineates better some elongated structures. 3.6 and 5.8 μm SPITZER bands also show structures roughly similar to those displayed by 4.5 and 8.0μm bands.

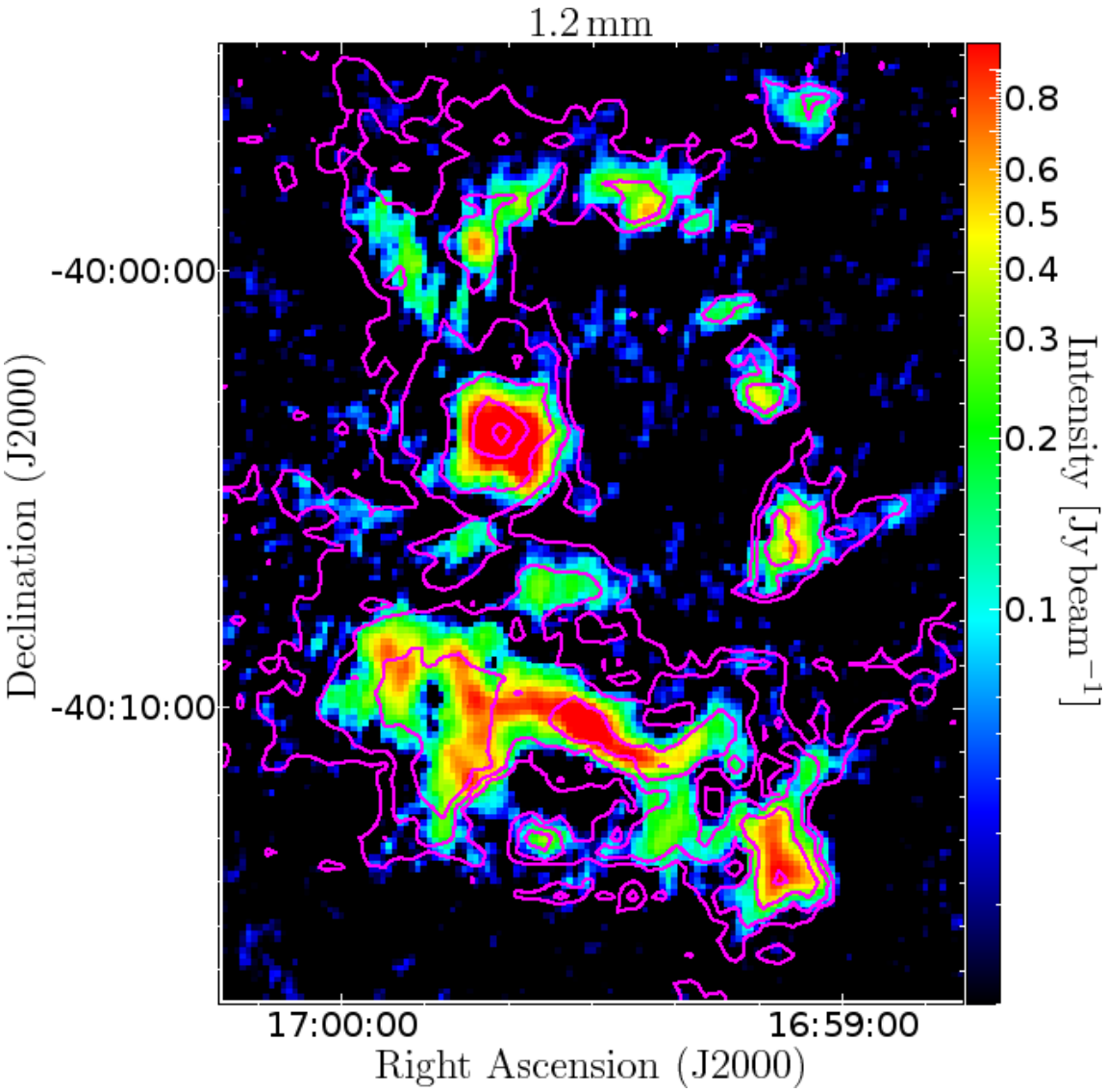

Figure 4.3: 1.2 mm continuum emission of the ring G345.50+1.50, with contours of the ^{13}CO(3-2) line emission integrated between -30 and -2 km s^{-1} (levels: 9, 18, 36, 72 and 144 K km s^{-1}).

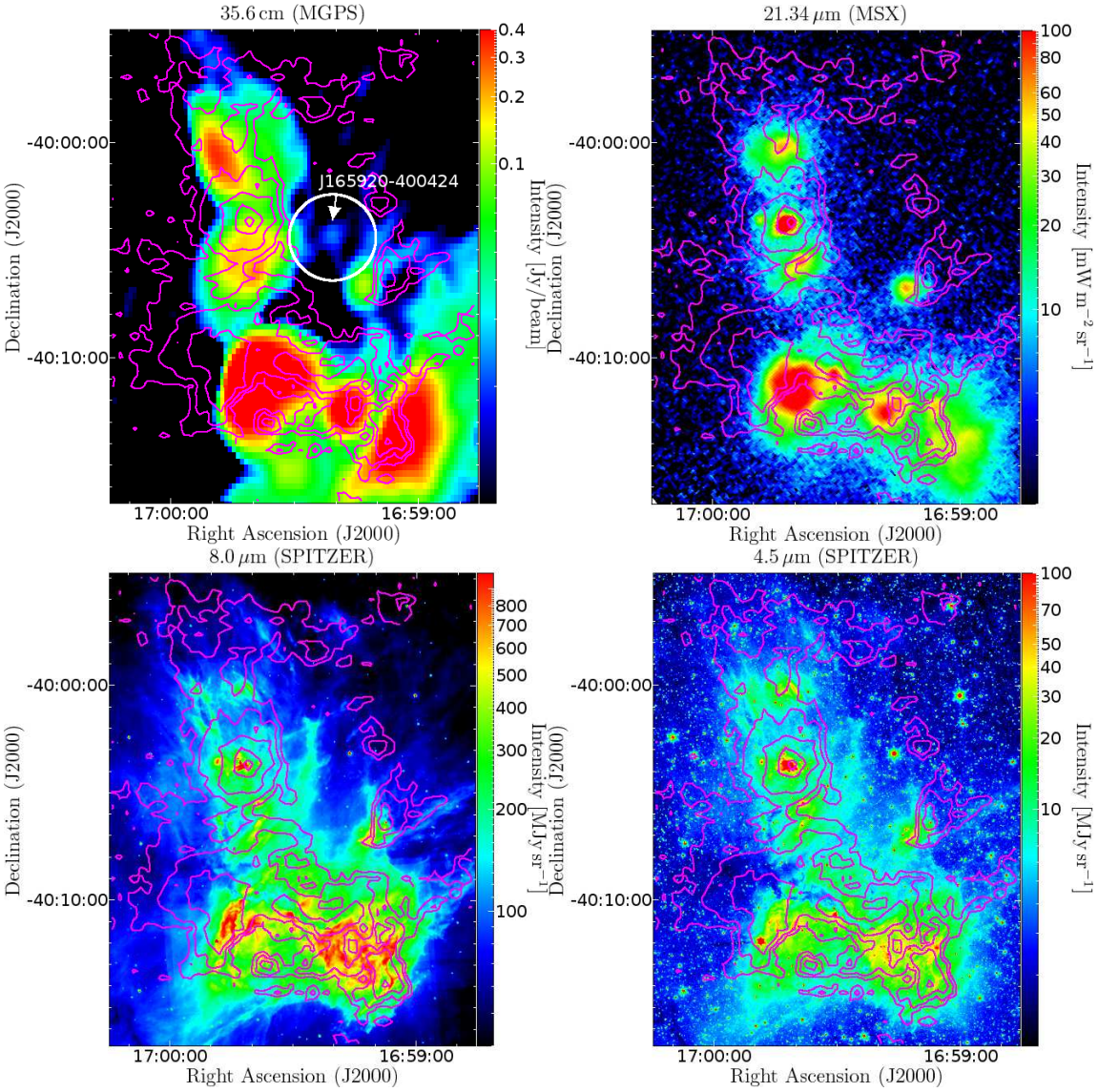

Figure 4.4: Radio and infrared observations in continuum emission toward the ring G345.50+1.50 with contours of the ^{13}CO(3-2) line emission integrated between -30 and -2 km s^{-1} (levels: 9, 18, 36, 72 and 144 K km s^{-1}). Top-left, at 35.6 cm from MGPS (Murphy et al. 2007). The arrow indicates the position of the J165920-400424 source, and the white circle indicates the area where we looked for objects in NED database to know about the nature of this source; this circle is centered at the position of the J165920-400424 source, and has a radius of 2 arcmin. Top-right, at 21.34 μm from MSX. Bottom-left, at 8.0 μm from SPITZER. Bottom-right, at 4.5 μm from SPITZER.

4.2 Gas temperature

Observations in the ^{12}CO(3-2) line allow us to estimate the kinematic gas temperature in the region. Assuming LTE, that the ^{12}CO(3-2) line is optically thick, and approximating the kinematic gas temperature, T_k, to the excitation gas temperature, the peak of the brightness temperature of the ^{12}CO(3-2) line, T_B, is given by

$$T_B = \frac{\nu h}{k} \frac{1}{\exp(\frac{\nu h}{k T_K}) - 1},$$

where ν is the frequency transition, h is the Planck constant, and k is the Boltzmann constant. Assuming that the main beam is filled,

$$f_{BEAM} T_B \sim T_{MB} \sim T_A^*/\eta_{MB},$$

where f_{BEAM} is the beam filling factor, ~1, T_{MB} is the peak of the main beam brightness temperature, T_A^* is the peak of the antenna temperature and η_{MB} is the main beam efficiency, ~0.7. T_A^* varies between 7.2 and 34 K, implying T_K between 17 and 57 K, with an average value of ~30 K (see Table 4.1). This average value is consistent with the dust temperature of ~30 K for MSFRs (Faúndez et al. 2004).

Table 4.1: List of observations in the ^{12}CO(3-2) line in the position switching observing mode toward peaks of the ^{13}CO(3-2) line emission. Columns 1 and 2 show equatorial coordinates, column 3, peaks of antenna temperatures, and column 4, estimated kinematic temperatures.

Equatorial Coordinate (J2000)		$^1T_A^*$	^1T_K
RA	Dec	K	K
16:59:08	-40:13:57	34	57
16:59:41	-40:03:37	32	53
16:59:44	-40:10:17	23	40
16:59:46	-40:11:37	25	43
16:59:20	-40:11:17	20	36
16:59:13	-40:11:17	23	41
16:59:08	-40:05:37	19	35
16:59:32	-40:10:17	15	29
16:59:35	-40:07:37	26	45
16:59:04	-40:11:17	20	36
16:59:23	-40:13:17	16	30
16:59:35	-40:12:57	21	38
16:59:53	-40:08:37	9.7	21
16:59:20	-40:09:37	14	28
16:59:11	-40:02:37	14	27
16:59:28	-39:57:57	13	25
16:59:23	-39:58:37	14	27
16:59:51	-40:00:37	18	34
16:59:44	-39:59:17	12	25
16:59:32	-39:58:17	13	26
16:59:16	-40:00:57	15	29
16:59:18	-39:58:57	13	26
16:59:30	-39:56:37	9.6	21
16:59:06	-39:55:57	11	23
16:58:50	-40:08:16	13	26
16:59:56	-39:58:37	11	23
16:59:49	-39:56:17	7.2	17
16:58:52	-40:09:16	15	29
16:59:58	-40:05:57	7.7	18

[1] The error for T_A^* and T_K values is ~0.2 K.

4.3 Column density and mass of the ring

Column density of the ring is determined by the ^{13}CO(3-2) line emission. Assuming that ^{13}CO(3-2) line emission is optically thin and in local thermal equilibrium (LTE), the column density can be expressed as (see Appendix I):

$$\frac{N_{^{13}CO}}{cm^{-2}} = 8.3\times10^{13}\left[\frac{H_2}{^{13}CO}\right]\frac{2\,\alpha}{\mu} \frac{\exp(15.9K/T_K)}{1-\exp(-15.9K/T_K)}\int T_B\frac{dv}{km\,s^{-1}}, \quad (4.1)$$

where T_K is the kinetic temperature of gas, ~30 K (see Sect. 4.2), $[H_2/^{13}CO]$ is the abundance ratio of H_2 to ^{13}CO molecules, ~7×10^5 (Frerking et al. 1982), μ is the mean mas per particle, ~2.29 for an H_2 cloud with a 25% of Helium (Evans 1999), and α is the H_2 mass correction to include Helium mass, ~1.3. The brightness temperature, T_b, is estimated by $f_{BEAM}T_b \sim T_A^*/\eta_{mb}$, where T_A^* is the antenna temperature, η_{mb} is the main beam efficiency, ~0.73, and f_{BEAM} is the beam filling factor, ~1 assuming main beam filled. Summarizing, the ^{13}CO(3-2) line emission, integrated between −30 and −2 km s^{-1} above 3 σ level, the column density varies between 2×10^{21} and 7×10^{22} cm^{-2}.

We compare $N_{^{13}CO}$ with the column density estimated from 1.2 mm continuum emission, $N_{1.2mm}$. This emission is assumed to be optically thin and produced by dust, thus the column density is given by (Hildebrand 1983)

$$N_{1.2\,mm} = \frac{I_{1.2\,mm}}{\mu\, m_H\, k_{1.2\,mm}\, B_{1.2\,mm(T_{dust})}}\frac{M_{gas}}{M_{dust}}, \quad (4.2)$$

where $I_{1.2\,mm}$ is the intensity, m_H is the hydrogen atom mass, $k_{1.2\,mm}$ is the dust absorption coefficient, ~1 cm^2/g for proto-stellar cores (Ossenkopf & Henning 1994), $B_{1.2\,mm}(T_{dust})$ is the Planck function at dust temperature T_{dust}, ~30 K for regions of massive star formation (Faúndez et al. 2004), and M_{gas}/M_{dust} is the ratio of gas to dust masses, ~100 (Hildebrand 1983).

Figure 4.5 shows the ratio of $N_{1.2\,mm}$ to $N_{^{13}CO}$ with contours of the ^{13}CO(3-2) line integrated between -30 and −2 km s^{-1}. $N_{1.2\,mm}/N_{^{13}CO}$ varies from ~0.1 to 10 with an av-

erage value of ~1.0. $N_{1.2\,mm}$ is higher than $N_{^{13}CO}$ toward sites with high density, while $N_{^{13}CO}$ is higher than $N_{1.2\,mm}$ toward sites with low density. It is possible that 1.2 mm continuum emission is more optically thin than the ^{13}CO(3-2) line toward dense regions, and the ^{13}CO(3-2) line more sensitive than 1.2 mm continuum emission toward regions with low density. The assumed values of the physical parameters can introduce variations in the estimated $N_{1.2\,mm}/N_{^{13}CO}$ ratios. For example, Faúndez et al. (2004) found massive star forming regions with dust temperatures between 18 and 46 K, which produce variations in the ratio by a factor 2. Hildebrand (1983) estimated a ratio of gas to dust masses of 100 with errors within a factor 2-8. Frerking et al. (1982) estimated a [$H_2/^{13}$CO] of 7×10^5 with possible variations of a factor 2-10. Ossenkopf & Henning (1994) computed a dust opacity of ~1 cm^2/g at 1.2 mm, with deviations no more than a factor 2. Beam dilution is other source of error; if there is beam dilution, the ratio $N_{1.2\,mm}/N_{^{13}CO}$ has to be corrected by a factor $\Omega^2_{MB-SEST}/\Omega^2_{MB-APEX}\sim (24'')^2/(18'')^2\sim1.8$, where $\Omega_{MB-SEST}$ is the main beam solid angle for SEST and $\Omega_{MB-APEX}$ for APEX.

Integrating Equations 4.1 and 4.2 over area, it is possible to determine the total mass of the ring from the ^{13}CO(3-2) line and 1.2 mm continuum emission:

$$\frac{M_{^{13}CO}}{M_\odot} = \int m_H\,\mu\,N_{^{13}CO}\,dA \sim 3.1\times10^{-11}\left[\frac{H_2}{^{13}CO}\right] \frac{D}{kpc}^{2}\,\alpha\,\frac{\exp(\frac{15.9K}{T_{ext}})}{1-\exp(\frac{-15.9K}{T_{ext}})}\int T_B\frac{dv}{km\,s^{-1}}\frac{d\Omega}{arcsec^2}, \quad (4.3)$$

and

$$M_{1.2\,mm} = \int m_H\,\mu\,N_{1.2\,mm}\,dA \sim \frac{S_{1.2\,mm}\,D^2}{k_{1.2\,mm}B_{1.2\,mm}(T_{dust})}\frac{M_{gas}}{M_{dust}},$$

where dA is the differential of area ($dA = D^2d\Omega$), D is the distance to the ring, ~1.8 kpc, Ω is the solid angle, and $S_{1.2\,mm}$ is the flux density. The total integrated emission in the ^{13}CO(3-2) line is ~1.8x10^7 K km s^{-1} arcsec^2, thus the ring has a total mass of 6.9×10^3 M$_\odot$. In 1.2 mm continuum emission, the total flux density is ~120 Jy, thus the total mass of ring is ~4.0×10^3 M$_\odot$. Considering the errors of the assumed physical parameters, the estimations of masses are in agreement.

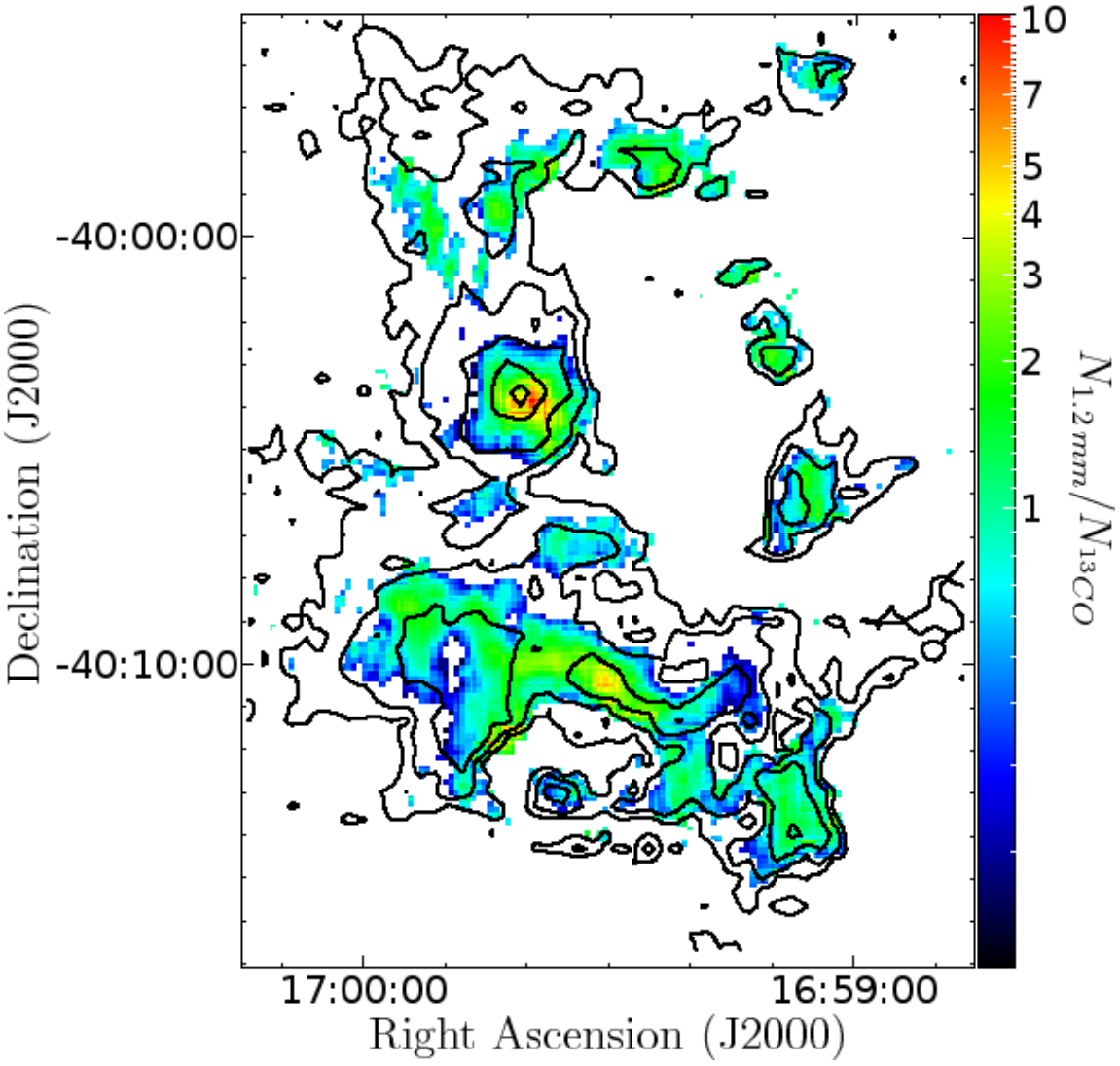

Figure 4.5: Ratio of $N_{1.2mm}$ to $N_{^{13}CO}$, considering emission in the ^{13}CO(3-2) line and 1.2 mm larger than three times rms. Contours represent ^{13}CO(3-2) line emission integrated between -30 and -2 km s^{-1} (levels: 9, 18, 36, 72 and 144 K km s^{-1}).

4.4 ^{13}CO(3-2) clumps

As it is shown in Fig. 4.2, the ^{13}CO(3-2) line emission is fragmented. Using CLUMPFIND (Williams et al. 1994; http://www.ifa.hawaii.edu/users/jpw/clumpfind.shtml), we identified 57 clumps, which contains 78% of the total integrated emission, $\sim 1.4\times10^{7}$ K km s^{-1} arcsec^{2}. CLUMPFIND creates contours over data, searches for peaks of emission to locate clumps, and follows them down to the lower intensity contour. To find these clumps, we integrated the data cube every 20 channels ($\sim$2.22 km s^{-1}), to prevent the algorithm from defining clumps at peaks formed by absorptions in the ^{13}CO(3-2) line. We applied the algorithm with a lower intensity contour of three rms and with a contouring interval equal to twice the rms. Once the algorithm define spatial and spectral areas of clumps, we associate emission of the initial data cube with clumps, recovering the observational spectral resolution ($\sim$0.111 km s^{-1}). We filter out fictitious clumps by two conditions: emission areas $\gtrsim$40×40 arcsec^{2} and emission peaks $\gtrsim$5 rms, $\sim$5 K.

Utilizing Eq. 4.3, the clumps have masses between 7.4 and 8.6×10^{2} M$_{\odot}$, with an average value of 93 M$_{\odot}$.

Clump diameters, D_c, are estimated from the deconvolved FWHM size of their emissions. They are calculated by

$$D_c = d\sqrt{\theta^2_{FWHM} - \theta^2_{beam}},$$

where θ_{bean} is the beam-size, θ_{FWHM} is the observed FWHM and d is the distance to the GMC.

Given masses and diameters, the mean column density, N$_c$, and the mean density, n$_c$, are calculated by

$$N_c = \frac{M_c}{\pi(D_c/2)^2}\frac{1}{\mu\, m_H}$$

and

$$n_c = \frac{M_c}{\frac{4}{3}\pi(D_c/2)^3}\frac{1}{\mu\, m_H},$$

where M_c is the mass. Clumps have column densities between 3×10^{21} and 6×10^{22} cm^{-2}

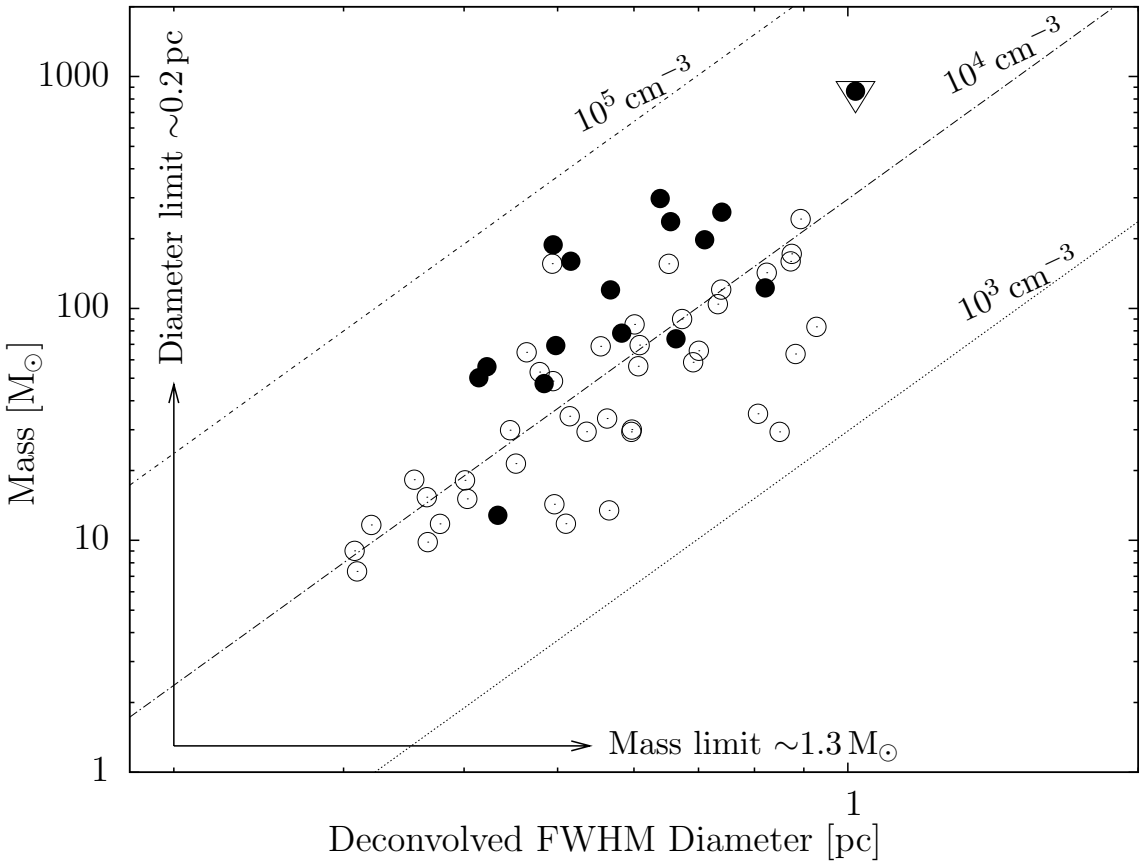

Figure 4.6: Mass versus diameter for the clump detected in the ^{13}CO(3-2) line. Filled circles represent clumps that have an infrared counterpart from MSX and SPITZER observations. Open circles symbolize clumps that are not associated with an infrared source. The triangle indicates the clump associated with the MSFR IRAS 16562-3959. The arrows mark the minimal detectable diameter and mass, ∼0.2 pc and ∼1.3 $M_\odot$, respectively. Dotted lines indicate mean densities at 10^3, 10^4 and 10^5 cm^{-3}.

with an average value of 2×10^{22} cm^{-2}, and densities between 2×10^3 and 5×10^4 cm^{-3} with an average value of 10^4 cm^{-3}. Figure 4.6 shows a plot of mass versus diameter for the detected clumps, with lines to display different mean densities. Clumps are concentrated in 10^4 cm^{-3}.

Figure 4.7 shows line width velocity (FWHM), ΔV_c, versus diameter, D_c, of the clumps. Line widths vary between 1.6 and 5.1 km s^{-1} with an average value of 3.2 km s^{-1}.

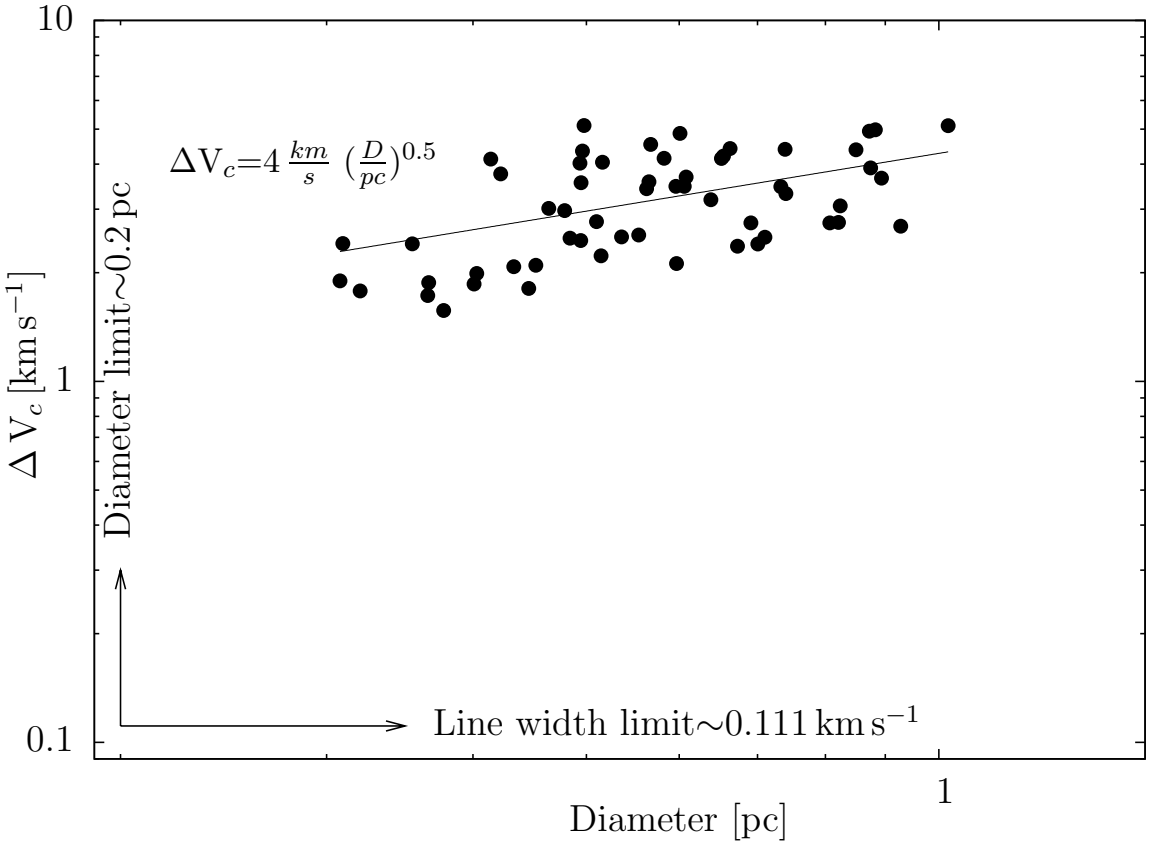

Figure 4.7: Line width velocity versus diameter for the clumps detected in the ^{13}CO(3-2) line. Arrows mark observational detection limits for the line widths and for the diameters, ∼0.111 km s^{-1} and ∼0.2 pc, respectively. The line shows the fit, ΔV=4 km s^{-1} (D pc^{-1})$^{0.5}$.

There is a relationship between the line width and the diameter given by

$$\Delta V_c \sim 4 \frac{km}{s} \left(\frac{D}{pc} \right)^{0.5} ,$$

although the dispersion is high, ∼1 km s^{-1}.

Table 4.2: Summary of the physical properties of the identified clumps.

Parameter	Range	Average value
Diameter	0.3-1.0 pc	0.6 pc
[1]Mass	7.4-8.6×10^2 $M_\odot$	93 $M_\odot$
[2]Density	2×10^3-5×10^4 cm^{-3}	10^4 cm^{-3}
[2]Column density	3×10^{21}-6×10^{22} cm^{-2}	2×10^{22} cm^{-2}
Line width velocity	1.6-5.1 km s^{-1}	3.2 km s^{-1}

[1] The total mass of the clumps is 5.3×10^3 $M_\odot$.

[2] Densities and column densities are estimated assuming a mean molecular weight of μ=2.29.

Table 4.2 shows a summary of the physical properties of the clumps, and Table 4.3, the estimations for each clump.

Physical properties of identified clumps are in accord with observations toward GMCs. For example, clumps within the GMC associated with RCW 106 detected in the ^{13}CO(1-0) line, ^{18}CO(1-0) line and 1.2 mm continuum emission have diameters from 0.3 to 4 pc, masses from 10 to 2×10^4 $M_\odot$, densities from 2×10^3 to 6×10^4 cm^{-3}, and line-width velocities from 0.4 to 3 km s^{-1} (Mookerjea et al. 2004; Bains et al. 2006; Wong et al. 2008). Observations in 1.2 mm continuum emission toward three GMCs found that the clump mass distribution has a spectral mass index between 1.3 and 1.9 (Mookerjea et al. 2004; Muñoz et al. 2007).

Table 4.3: Physical properties of ^{13}CO clumps. Column 1 gives names; columns 2 and 3, equatorial coordinates (J2000); column 4, diameters; column 5, masses; column 6, line widths; column 7, densities; column 8, column densities; and column 9, if clumps have an infrared counterpart from MSX and SPITZER observations.

Name	Equatorial Coordinate (J2000)		Diameter	Mass	Line width	Density	Column density	Infrared
	RA	Dec	pc	$M_\odot$	km s^{-1}	cm^{-3}	cm^{-2}	counterpart
1	16:59:07	-40:13:57	0.6	3.0×10^{2}	3.2	3.9×10^{4}	5.1×10^{22}	Y
2	16:59:41	-40:3:37	1	8.6×10^{2}	5.1	2.8×10^{4}	5.8×10^{22}	Y
3	16:59:20	-40:11:17	0.7	2.4×10^{2}	4.2	2.9×10^{4}	3.8×10^{22}	Y
4	16:59:44	-40:10:37	0.5	1.6×10^{2}	4.1	3.9×10^{4}	4.2×10^{22}	Y
5	16:59:48	-40:11:17	0.5	1.9×10^{2}	3.6	5.2×10^{4}	5.3×10^{22}	Y
6	16:59:07	-40:5:37	0.7	2.0×10^{2}	2.5	1.9×10^{4}	2.7×10^{22}	Y
7	16:59:13	-40:11:17	0.6	1.2×10^{2}	4.5	2.2×10^{4}	2.6×10^{22}	Y
8	16:59:32	-40:10:17	0.7	2.6×10^{2}	3.3	2.2×10^{4}	3.3×10^{22}	Y
9	16:59:43	-40:11:17	0.4	5.0×10^{1}	4.1	2.4×10^{4}	2.0×10^{22}	Y
10	16:59:48	-40:9:37	0.5	1.6×10^{2}	4.0	4.4×10^{4}	4.4×10^{22}	N
11	16:59:04	-40:11:16	0.6	6.9×10^{1}	3.7	1.0×10^{4}	1.3×10^{22}	N

Continued on next page

Table4.3 – continued from previous page

Name	Equatorial Coordinate (J2000)		Diameter pc	Mass $M_\odot$	Line width km s^{-1}	Density cm^{-3}	Column density cm^{-2}	Infrared counterpart
	RA	Dec						
12	16:59:35	-40:12:57	0.4	5.6×10^{1}	3.8	2.5×10^{4}	2.2×10^{22}	Y
13	16:59:37	-40:7:37	0.9	1.6×10^{2}	4.9	8.1×10^{3}	1.5×10^{22}	N
14	16:59:53	-40:8:57	0.9	2.4×10^{2}	3.7	1.2×10^{4}	2.1×10^{22}	N
15	16:59:23	-40:13:17	0.6	8.5×10^{1}	4.9	1.3×10^{4}	1.6×10^{22}	N
16	16:59:53	-40:10:17	0.7	1.6×10^{2}	4.2	1.9×10^{4}	2.5×10^{22}	N
17	16:59:09	-40:2:57	0.5	4.9×10^{1}	2.5	1.4×10^{4}	1.4×10^{22}	N
18	16:59:20	-40:9:37	0.8	1.4×10^{2}	3.1	8.6×10^{3}	1.5×10^{22}	N
19	16:59:43	-40:8:17	0.9	1.7×10^{2}	3.9	8.7×10^{3}	1.6×10^{22}	N
20	16:59:32	-40:7:17	0.7	1.0×10^{2}	3.5	9.0×10^{3}	1.4×10^{22}	N
21	16:59:14	-40:14:17	0.5	5.3×10^{1}	3.0	1.6×10^{4}	1.6×10^{22}	N
22	16:59:23	-39:58:17	0.6	6.9×10^{1}	2.6	1.4×10^{4}	1.6×10^{22}	N
23	16:59:44	-39:59:17	0.5	6.5×10^{1}	3.0	2.2×10^{4}	2.1×10^{22}	N
24	16:59:41	-40:1:37	0.7	1.2×10^{2}	4.4	1.0×10^{4}	1.5×10^{22}	N
25	16:59:49	-40:12:57	0.6	7.8×10^{1}	4.2	1.3×10^{4}	1.6×10^{22}	Y
26	16:59:14	-40:13:17	0.5	6.9×10^{1}	5.1	1.9×10^{4}	1.9×10^{22}	Y
27	16:59:42	-39:58:37	0.7	9.0×10^{1}	2.4	1.0×10^{4}	1.4×10^{22}	N

Continued on next page

Table4.3 – continued from previous page

Name	Equatorial Coordinate (J2000)		Diameter pc	Mass $M_\odot$	Line width km s^{-1}	Density cm^{-3}	Column density cm^{-2}	Infrared counterpart
	RA	Dec						
28	16:58:54	-40:5:16	0.6	3.0×10^{1}	2.1	4.8×10^{3}	5.9×10^{21}	N
29	16:59:18	-39:58:57	0.5	2.1×10^{1}	2.1	7.8×10^{3}	7.3×10^{21}	N
30	16:59:14	-40:0:57	0.4	1.8×10^{1}	2.4	1.4×10^{4}	1.0×10^{22}	N
31	16:59:51	-40:0:37	0.8	1.2×10^{2}	2.8	7.5×10^{3}	1.3×10^{22}	Y
32	16:59:44	-40:0:17	0.5	4.7×10^{1}	2.5	1.4×10^{4}	1.4×10^{22}	Y
33	16:59:07	-40:10:17	0.7	7.4×10^{1}	4.4	8.6×10^{3}	1.2×10^{22}	Y
34	16:59:30	-39:56:37	0.7	5.9×10^{1}	2.8	6.0×10^{3}	8.5×10^{21}	N
35	16:59:06	-39:56:16	0.6	5.6×10^{1}	3.5	8.6×10^{3}	1.1×10^{22}	N
36	16:59:32	-39:58:17	0.5	3.4×10^{1}	2.2	8.5×10^{3}	9.0×10^{21}	N
37	16:59:30	-39:57:37	0.5	3.0×10^{1}	1.8	1.1×10^{4}	1.0×10^{22}	N
38	16:59:01	-40:4:37	0.5	2.9×10^{1}	2.5	6.5×10^{3}	7.1×10^{21}	N
39	16:59:56	-39:58:37	0.7	6.6×10^{1}	2.4	6.5×10^{3}	9.3×10^{21}	N
40	16:59:13	-40:1:57	0.4	1.8×10^{1}	1.9	9.5×10^{3}	7.9×10^{21}	N
41	16:59:32	-40:5:17	0.8	3.5×10^{1}	2.8	2.3×10^{3}	3.8×10^{21}	N
42	16:58:50	-40:8:16	0.4	1.5×10^{1}	2.0	7.8×10^{3}	6.5×10^{21}	N
43	16:58:47	-40:7:56	0.4	9.8×10^{0}	1.9	6.7×10^{3}	5.1×10^{21}	N

Continued on next page

Table4.3 – continued from previous page

Name	Equatorial Coordinate (J2000)		Diameter pc	Mass $M_\odot$	Line width km s^{-1}	Density cm^{-3}	Column density cm^{-2}	Infrared counterpart
	RA	Dec						
44	16:59:49	-39:56:17	0.9	8.3×10^{1}	2.7	3.5×10^{3}	6.7×10^{21}	N
45	16:59:44	-40:13:17	0.4	1.3×10^{1}	2.1	5.3×10^{3}	4.7×10^{21}	Y
46	17:0:00	-40:5:16	0.9	2.9×10^{1}	4.4	1.6×10^{3}	2.8×10^{21}	N
47	16:59:13	-39:57:37	0.3	9.0×10^{0}	1.9	1.0×10^{4}	6.6×10^{21}	N
48	16:58:55	-40:10:16	0.4	1.5×10^{1}	1.7	1.1×10^{4}	8.0×10^{21}	N
49	16:59:56	-40:6:57	0.9	6.4×10^{1}	5.0	3.1×10^{3}	5.7×10^{21}	N
50	17:0:03	-39:57:36	0.6	2.9×10^{1}	3.5	4.7×10^{3}	5.7×10^{21}	N
51	17:0:00	-39:55:37	0.6	3.4×10^{1}	3.4	6.4×10^{3}	7.4×10^{21}	N
52	16:59:25	-40:14:17	0.3	1.2×10^{1}	1.8	1.2×10^{4}	7.9×10^{21}	N
53	16:59:58	-40:5:57	0.5	1.2×10^{1}	2.8	3.0×10^{3}	3.2×10^{21}	N
54	16:59:34	-40:14:17	0.3	7.4×10^{0}	2.4	8.4×10^{3}	5.3×10^{21}	N
55	16:58:50	-40:9:36	0.4	1.2×10^{1}	1.6	7.4×10^{3}	5.7×10^{21}	N
56	16:59:30	-40:13:57	0.5	1.4×10^{1}	4.4	4.0×10^{3}	4.0×10^{21}	N
57	16:58:55	-40:8:56	0.6	1.4×10^{1}	3.6	2.5×10^{3}	2.9×10^{21}	N

4.5 Gravitational stability

To investigate whether clumps are gravitationally bound, we examine their physical properties using two methods. First assuming virial equilibrium (e.g. Bertoldi and McKee 1992), and second, Bonnor-Ebert spheres (Bonnor 1956).

4.5.1 Virial equilibrium

For the gravitational potential, the virial condition is 2T+W=0, where T is the kinetic energy and W is the potential energy. For a clump with homogeneous density distribution, this condition implies

$$M_{vir} = \frac{5\,R_c\,\sigma_v^2}{G},$$

where M_{vir} is the virial mass, R_c is the radius and σ_v is the velocity dispersion, $\sim\Delta V_c/\sqrt{8\ln(2)}$. M_{vir} allows us to define the parameter α_{virial} as

$$\alpha_{virial} = \frac{M_{vir}}{M_c},$$

where M_c is the mass of the clumps. α_{virial} is utilized as an indicator of gravitational stability, since is a measurement of the ratio of the kinetic energy to the gravitational energy (e.g. Wong et al. 2008). For $\alpha_{virial}>>1$, clumps must be confined by an external pressure to be in hydrostatic equilibrium and prevent expansion; for $\alpha\sim1$, clumps are in equilibrium; and for $\alpha<<1$, clumps are unable to support themselves against gravity.

Figure 4.8 shows α_{virial} versus mass for the identified clumps. α_{virial} tends to decrease with mass, however, all clumps have $\alpha_{virial}>1$, thus they must be confined by an external pressure to be in hydrostatic equilibrium.

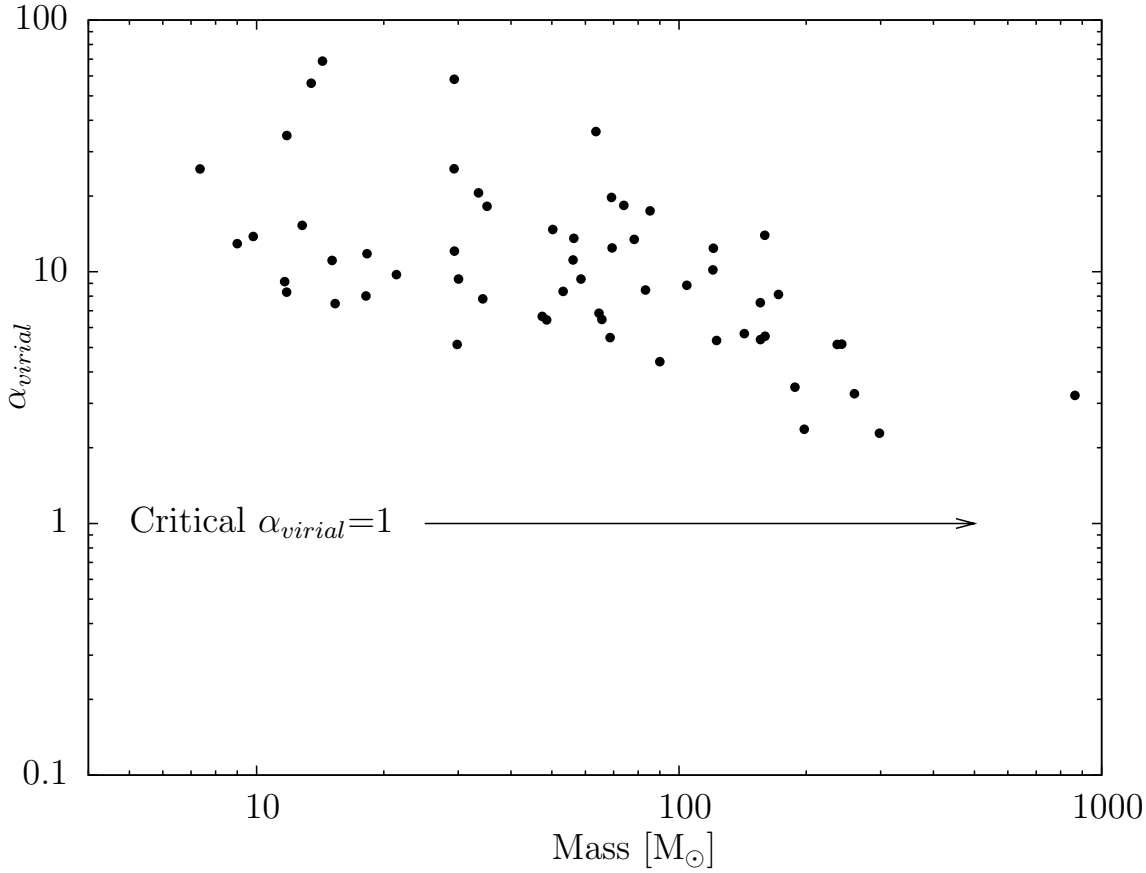

Figure 4.8: α_{virial} versus mass for the identified clumps. Arrow indicates the critical values of α_{virial}, 1.

4.5.2 Bonnor-Ebert sphere

The equation of hydrostatic equilibrium for a gas sphere is

$$-\frac{dp}{dr} = \frac{4\pi G\rho}{r^2}\int_0^r \rho\bar{r}^2 d\bar{r},$$

where p is the pressure, r is the distance to the center and ρ is the density. Considering the equation of state $p = k\rho T_K/(\mu m_H)$, and making the following substitutions $\rho = \rho_c e^{-\psi}$ and $r = \xi C_s/\sqrt{4\pi G}$, the equation of hydrostatic equilibrium becomes

$$\frac{1}{\xi^2}\frac{d}{d\xi}\left(\xi^2\frac{d\psi}{\xi}\right) = e^{-\psi}, \tag{4.4}$$

where ξ is a dimensionless variable, ψ is a dimensionless function, ρ_c is the central density (at r=0), C_s is the isothermal sound speed, i.e., $C_s^2 = kT_k/(\mu m_H)$ with T_K as the kinematic temperature.

Imposing the boundary conditions at r=0: $\rho(r) = \rho_c$ and $d\rho(r)/dr = 0$, i.e., $\psi(\xi) = 0$ and $d\psi(\xi)/d\xi$ at ξ=0, Eq. 4.4 is integrable numerically. If the gas sphere is confined by an external pressure P_{ext} at the boundary defined by the Bonnor-Ebert radius (R_{B-E}), the solution of Eq. 4.4 can be characterized by the dimensionless radius $\xi_{max} = \xi(r = R_{B-E})$, so R_{B-E} can be expressed as

$$R_{B-E} = \xi_{max} C_s/\sqrt{4\pi G\rho_c},$$

the external pressure as

$$P_{ext} = C_s^2\,\rho_c e^{-\psi}\Big|_{\xi_{max}},$$

and the clump mass as

$$M_{BE} = \frac{C_s^2 R_{B-E}}{G}\xi_{max}\left.\frac{d\psi}{d\xi}\right|_{\xi_{max}}$$

The stability of such pressure truncated gas spheres was investigated by Bonnor (1956), who showed that when ξ_{max}> 6.5 the spheres are in a state of unstable equilibrium, susceptible to gravitational collapse. Studies of the density profile toward isolated

molecular clouds (Bok globules) in starless stages show that ξ_{max} is concentrated near the critical value (ξ_{max}= 6.5), suggesting that this gaseous configuration represents the initial condition for star formation in dense cores (Lada et al. 2007).

Theoretically, the supporting mechanism in a Bonnor-Ebert sphere is purely the thermal pressure, but clumps also have non-thermal support (e.g. turbulence). We assume that the non-thermal support can be included in the model by replacing in Eq. 4.4 the isothermal sound speed C_s by an effective speed C_{eff}, where

$$C_{eff}^2 = C_s^2 + C_{NT}^2,$$

with C_{NT} as the non-thermal speed (e.g. Kandori et al. 2005).

Figure 4.9 displays dimensionless radius ξ_{max} versus mass, and Fig. 4.10, external pressure P_{ext} versus mass, where we approximate the effective speed as

$$C_{eff} \sim \frac{\Delta V_c}{\sqrt{8\ln(2)}},$$

and the Bonnor-Ebert radius as

$$R_{B-E} \sim \frac{D_c}{2}.$$

To be in hydrostatic equilibrium, clumps require external pressures between $8{\times}10^5$ and $3{\times}10^7$ K cm^{-3} with an average value of $7{\times}10^6$ K cm^{-3}. This is consistent with α_{virial} being greater than 1 for all clumps, estimated in Sect. 4.5.1.

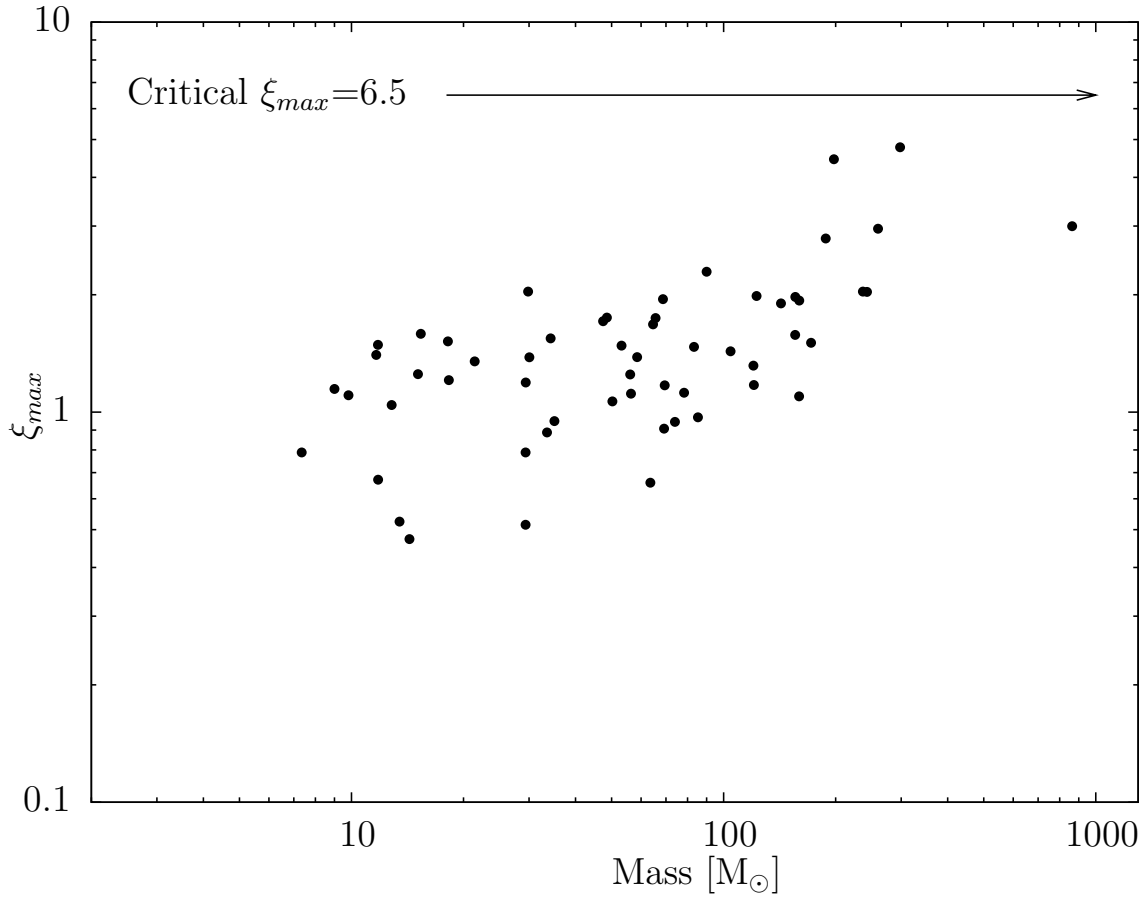

Figure 4.9: Dimensionless radius ξ_{max} versus mass for the clumps detected in the ^{13}CO(3-2) line. The arrow marks the critical state for the Bonnor-Ebert spheres (ξ_{max}=6.5).

ξ varies between 0.5 and 4.8, and seems to have no correlation with the mass, but the external pressure needed to keep the clumps in hydrostatic equilibrium seems to increases with the mass, being larger than the internal pressure of the GMC, P_{GMC}. This pressure is estimated by the pressure required to hold the GMC from collapsing under its own weight in virial equilibrium (e.g. Bertoldi & McKee 1992),

$$P_{GMC} \sim -\frac{W_{GMC}}{3V_{GMC}} = \frac{1}{5}\frac{G\,M_{GMC}^2}{V_{GMC}R_{GMC}} \sim 3\times10^5\,K\,cm^{-3},$$

where V_{GMC}, M_{GMC} and R_{GMC} are the volume (~$4/3\pi R_{GMC}^3$), mass (~6.5×10^5 $M_\odot$) and radius (~34 pc) of the GMC, respectively. This estimation for P_{GMC} is similar to the typical internal pressures of GMCs, ~10^5 K cm^{-3} (e.g. Blitz 1993).

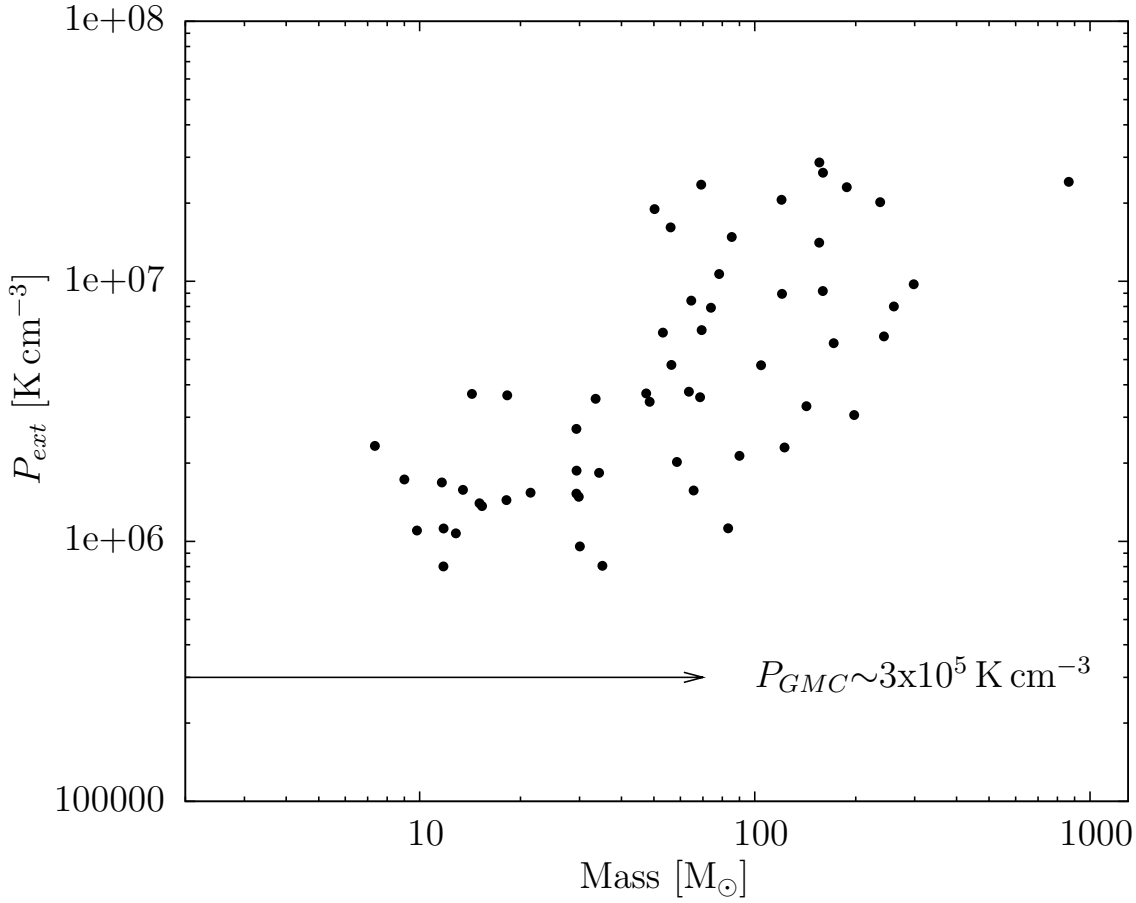

Figure 4.10: External pressure P_{ext} versus mass for the clumps identified in the ^{13}CO(3-2) line. The arrow indicates the internal pressure of the GMC G345.5+1.5, P_{GMC}, ~3×10^5 K cm^{-3}.

4.6 Association of ^{13}CO(3-2) clumps with 1.2 mm continuum emission

Using their emission areas, we associate the clumps identified in 1.2 mm (1.2 mm clumps) with those detected in the ^{13}CO(3-2) line (^{13}CO clumps). 32 ^{13}CO clumps are associated with 54 1.2 mm clumps, where 17 ^{13}CO clumps contains more than one 1.2 mm clump.

Figure 4.11 shows the ratio of mass estimated from 1.2 mm emission to that estimated from ^{13}CO(3-2) line, versus mass estimated from 1.2 mm for the 32 associations. The ratio of masses, $M_{1.2\,mm}/M_{13CO}$, have a range between 0.13 and 1.9 with an average value of ~0.7. Considering the error of the physical parameters assumed, masses estimated from 1.2 mm continuum emission and ^{13}CO(3-2) line are in agreement.

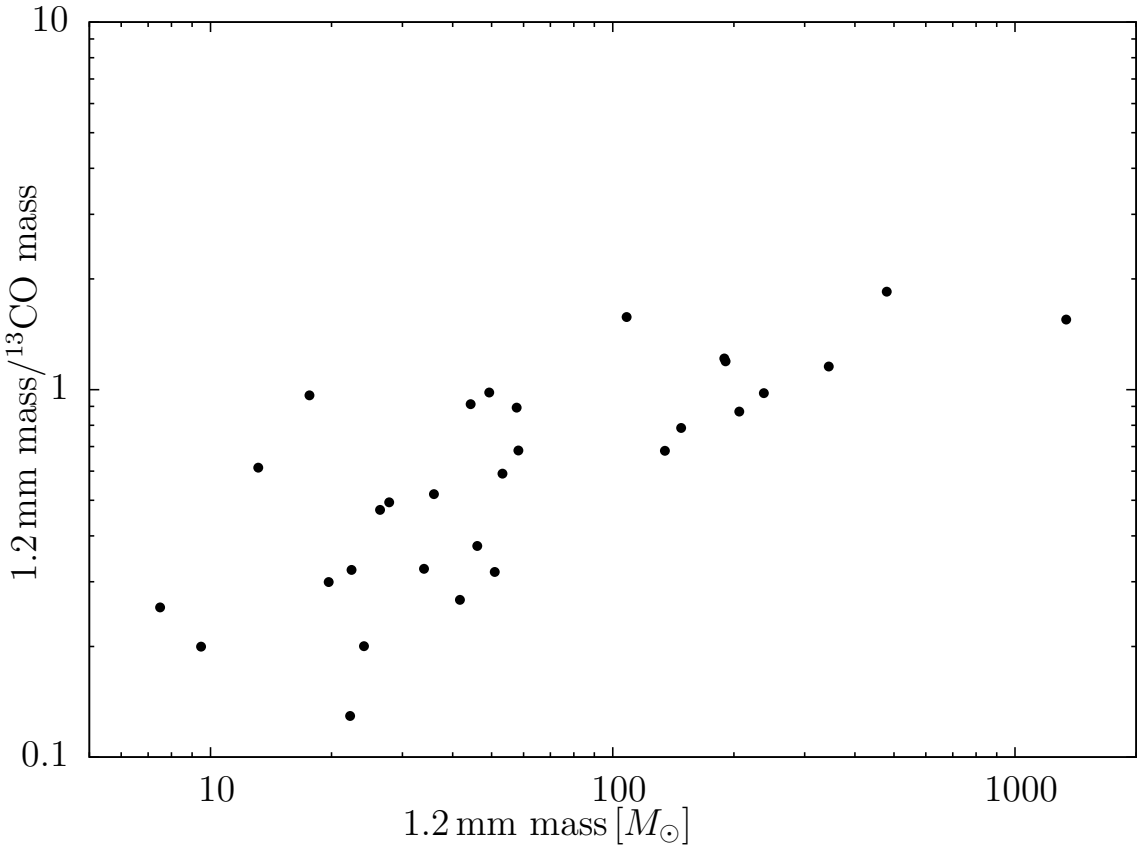

Figure 4.11: Ratio of mass estimated from 1.2 mm continuum emission to that estimated from the ^{13}CO(3-2) line, versus mass estimated from 1.2 mm for the 32 associations between the clumps detected in the 1.2 mm emission and the clumps detected in the ^{13}CO(3-2) line.

4.7 Association with infrared emission (IRAS - MSX - SPITZER)

We associate ^{13}CO clumps with infrared emission using IRAS, MSX and SPITZER observations. 28% of the clumps have an infrared counterpart in all MSX (8, 12, 14 and 21 μm) and SPITZER IRAC bands (3.6, 4.5, 5.8 and 8.0 μm). The rest of clumps, ~72%, are not detected in all MSX and SPITZER bands, mainly at 12.13, 14.65 and 21.34 μm. Since 8.0 μm MSX band and SPITZER IRAC bands are sensitive to the polycyclic aromatic hydrocarbon (PAH) emission and to the photospheric emission from stars (e.g. Chavarría et al. 2008), clump not detected in all MSX and SPITZER bands are considered to have no counterpart at infrared wavelengths. As MSX and SPITZER observations have sensitivity limits, the percentage of detection is a lower limit of the number of clumps that are forming stars, and the percentage of no detection is an upper limit of the number of clumps that are not forming stars.

Clumps with infrared emission do not have restriction in their physical properties, as is shown in Fig. 4.6, although they are more massive than the rest of clumps; clumps with infrared counterpart have an average mass of ~1.8×10^2 $M_\odot$, and the rest of the clumps have an average mass of ~61 $M_\odot$. For example, the clump associated with the MSFR IRAS 16562-3959 is the most massive and dense one, as is indicated in Fig. 4.6.

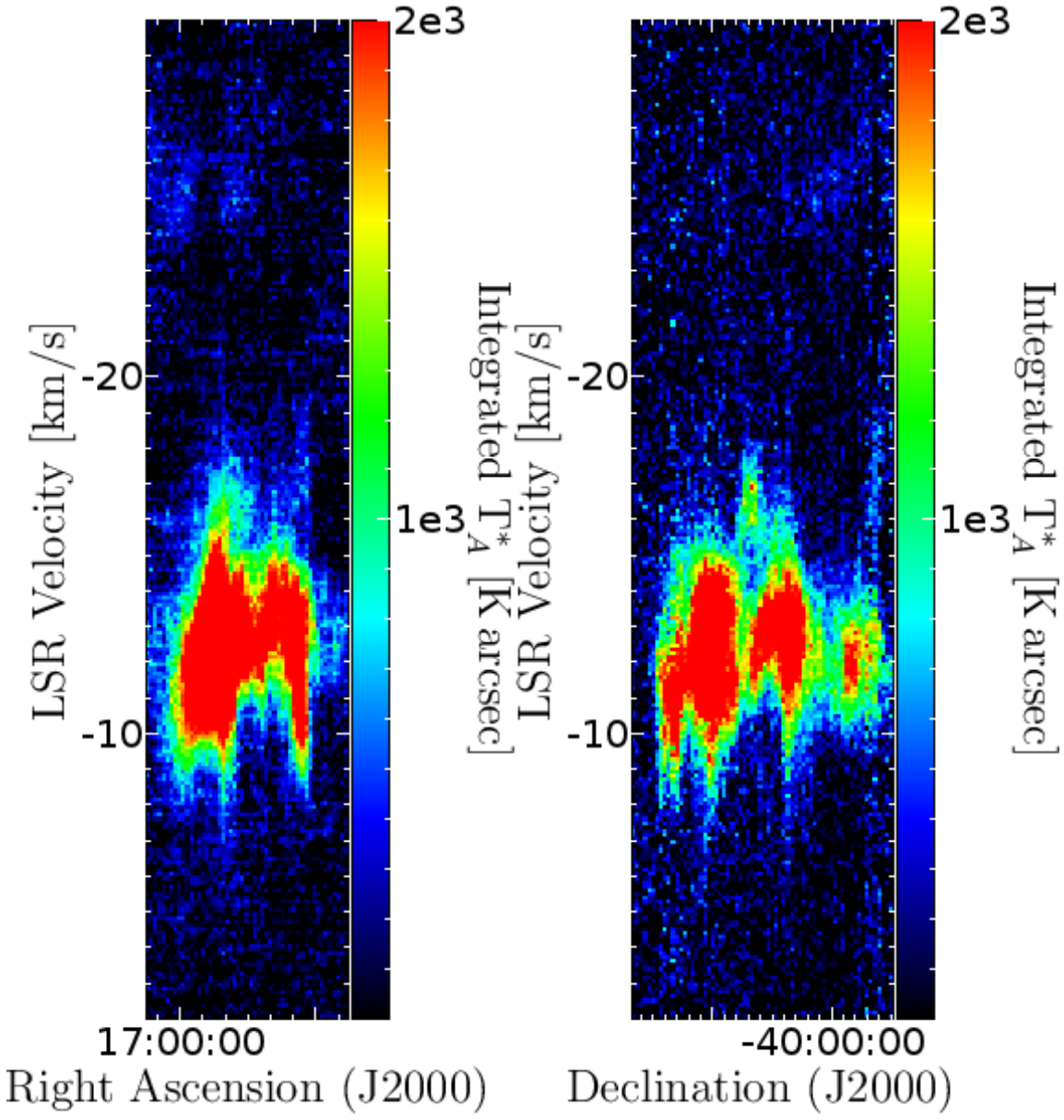

Figure 4.12: ^{13}CO(3-2) line emission integrated over declination (left image) and over right ascension (right image).

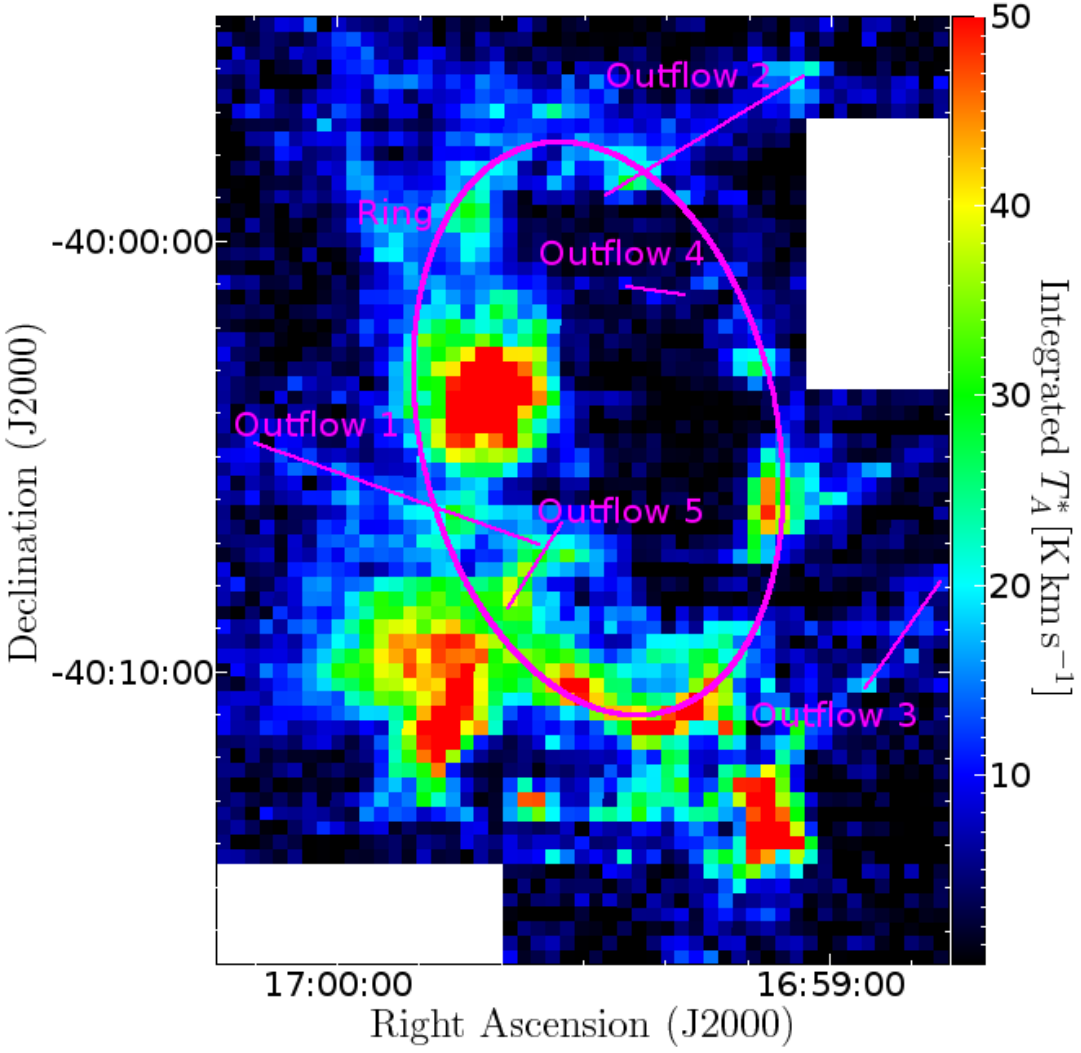

Figure 4.13: ^{13}CO(3-2) line emission integrated between -30 and -2 km s^{-1}, showing the expanding ring and the 5 molecular outflows identified.

4.8 Kinematic structure

G345.45+1.50 has a complex kinematics, which is shown in Fig. 4.12 using the ^{13}CO(3-2) line emission integrated over right ascension and over declination. There, we identify an expanding ring and 5 molecular outflows, which are presented in Fig. 4.13.

4.8.1 Expanding ring

The expanding ring is shown in Fig. 4.15, using the ^{13}CO(3-2) line emission integrated from -30 to -2 km s^{-1}, and the position-velocity diagram, following an ellipse shape that delineates the ring. By the form of the position-velocity diagram, we model the ring in expansion as a function of the polar angle θ:

$$\begin{pmatrix} x(\theta) \\ y(\theta) \\ z(\theta) \end{pmatrix} = \begin{pmatrix} x_0 \\ y_0 \\ z_0 \end{pmatrix} + \begin{pmatrix} \cos\beta & -\sin\beta & 0 \\ \sin\beta & \cos\beta & 0 \\ 0 & 0 & 1 \end{pmatrix} \begin{pmatrix} \cos\alpha & 0 & -\sin\alpha \\ 0 & 1 & 0 \\ \sin\alpha & 0 & \cos\alpha \end{pmatrix} \begin{pmatrix} R\cos\theta \\ R\sin\theta \\ 0 \end{pmatrix},$$

where x(θ) is the axis parallel to the right ascension, but with opposite sense, y(θ) is the axis parallel to the declination with the same sense, z(θ) is the depth ($\hat{z}=\hat{y}\times\hat{x}$), θ is in counter-clockwise from the x axis, varying between 0 and 2π, (x_0,y_0,z_0) is the coordinate of the spatial center, α is the rotating angle between axis x and z, β is the rotating angle between axis x and y, and R is the radius.

Assuming that $R = V\,t$, where V is the expanding velocity and t is the time of expansion, we can derive respected time the equation above, and add a LSR velocity center

Table 4.4: Characteristics of the expanding ring.

Parameter	Value
Spatial center	16:59:28 -40:04:20 (J2000)
LSR velocity	-12.1 km s^{-1}
Radius	3.5 pc
Expanding velocity	1.4 km s^{-1}
Rotating angle β	13 deg
Rotating angle α	-52 deg
Mass	6.9×10^3 M$_\odot$
Energy	1.4×10^{47} erg
Expanding time	2.4×10^6 yr

(v_{x0},v_{y0},v_{z0}), to obtain the LSR velocity of the ring as

$$\begin{pmatrix} v_x(\theta) \\ v_y(\theta) \\ v_z(\theta) \end{pmatrix} = \begin{pmatrix} v_{x0} \\ v_{y0} \\ v_{z0} \end{pmatrix} + \begin{pmatrix} \cos\beta & -\sin\beta & 0 \\ \sin\beta & \cos\beta & 0 \\ 0 & 0 & 1 \end{pmatrix} \begin{pmatrix} \cos\alpha & 0 & -\sin\alpha \\ 0 & 1 & 0 \\ \sin\alpha & 0 & \cos\alpha \end{pmatrix} \begin{pmatrix} V\cos\theta \\ V\sin\theta \\ 0 \end{pmatrix}.$$

To clarify, Fig. 4.14 shows a sketch of the expanding ring model. Our observations give information of $x(\theta)$, $y(\theta)$ and $v_z(\theta)$, which allow us to determine x_0, y_0, v_{z0}, α, β, R and V. The best fit is with center at 16:59:28 -40:04:20 (J2000), LSR velocity at -12.1 km s^{-1}, β ~13°, α ~−52°, radius ~3.5 pc, and expanding velocity ~1.4 km s^{-1}. Considering a total mass of 6.9×10^3 M$_\odot$, the total energy of the ring is ~1.4×10^{47} erg (E=M V^2/2). The expanding time scale is estimated to be ~2.4×10^6 yr (t=R/V). Table 4.4 shows estimated parameters.

The 35.6 cm source J165920-400424 is near to the center of the ring, ~90 arcsec, without an infrared counterpart, thus it is possible to explain this expansion by a supernova explosion. J165920-400424 can be a pulsar, resulting from the gravitational collapse of a massive star.

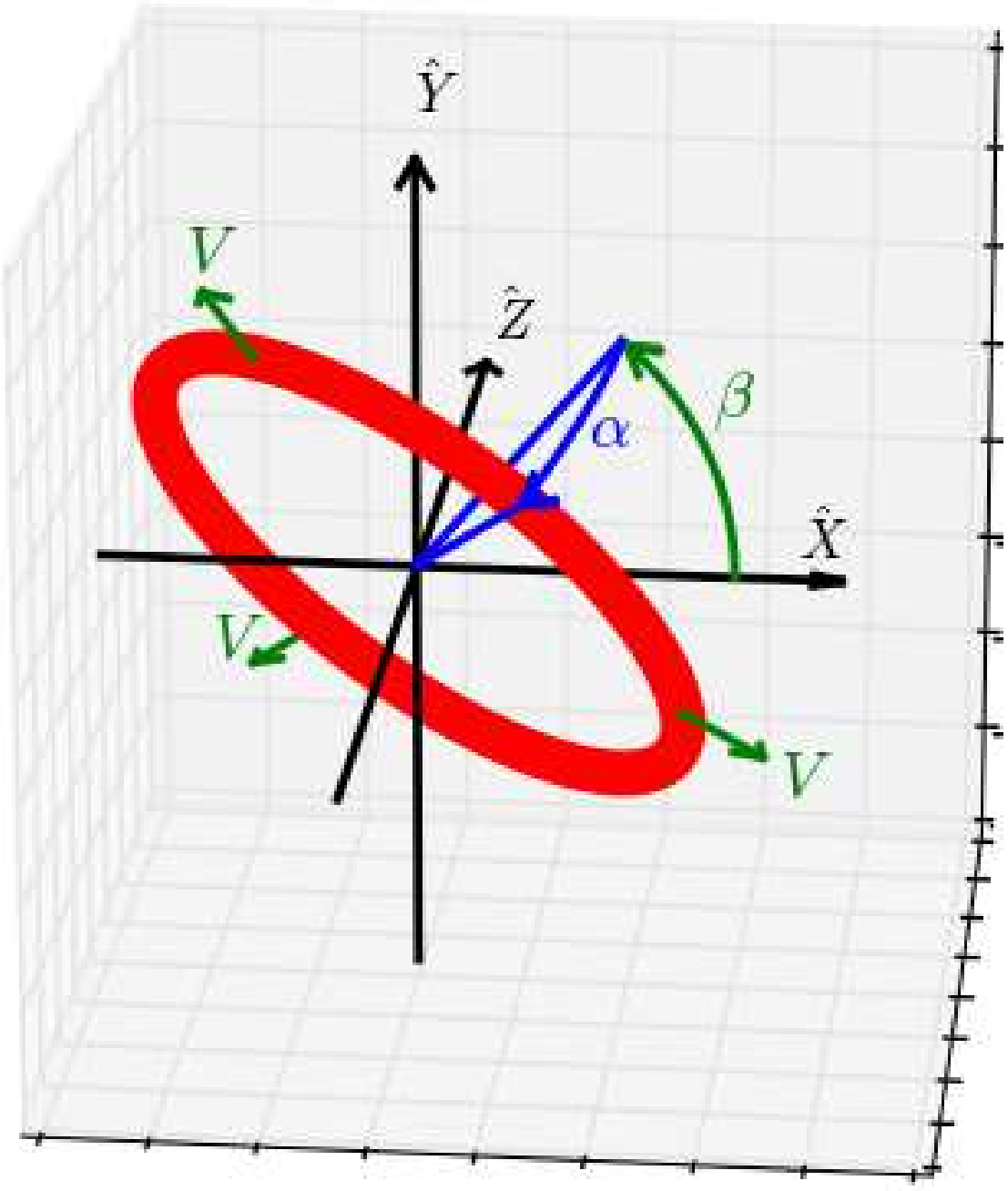

Figure 4.14: Sketch of the expanding ring model in 3D. The model is shown with $\alpha = -50$ deg and $\beta = 50$ deg.

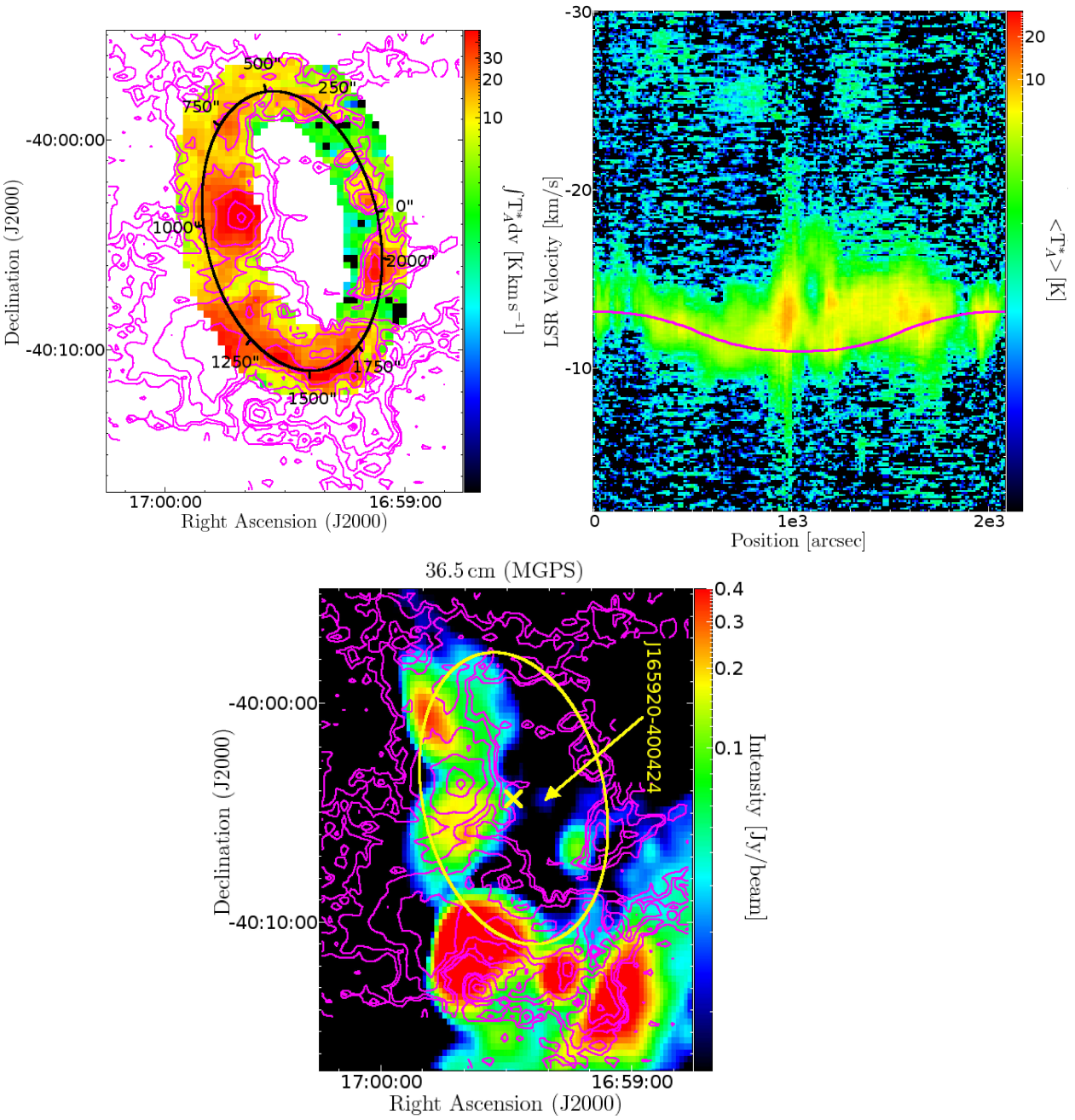

Figure 4.15: The expanding ring. Top-left, the ^{13}CO(3-2) line emission integrated between -16 and -9 km s^{-1}. The black ellipse shows the spatial distribution of the ring. Top-right, the position-velocity diagram of the average ^{13}CO(3-2) line emission following the spatial distribution of the ring, which is displayed in the left image; the magenta line shows the position-velocity distribution of the ring model. Bottom, 36.5 cm emission from MGPS data. The arrow marks the position of MGPS source J165920-400424; the yellow ellipse and the cross indicate, respectively, the spatial distribution and the spatial center of the ring. Contours are the ^{13}CO(3-2) line integrated between -30 and −2 km s^{-1} (5.4, 9.0, 18, 36, 72 and 144 K km s^{-1}).

4.8.2 Molecular outflows

Molecular outflows are identified by their elongated structures and by their velocity gradients along of their spatial distributions. They are shown in Figs. 4.17 and 4.18. We model their spatial distributions as a function of the parameter r:

$$\begin{pmatrix} x(r) \\ y(r) \end{pmatrix} = \begin{pmatrix} x_0 \\ y_0 \end{pmatrix} + \begin{pmatrix} \cos\beta & -\sin\beta \\ \sin\beta & \cos\beta \end{pmatrix} \begin{pmatrix} r \\ 0 \end{pmatrix},$$

where x(r) is the axis parallel to right ascension, but with opposite sense, y(r) is the axis parallel to declination with the same sense, (x_0,y_0) is the initial spatial coordinate, the place where is assumed that the molecular ejection starts, r is the distance to (x_0,y_0), varying between 0 and S_p, S_p is the projected size, and β is the rotating angle between axes x and y.

The projected velocity detected in z axis, perpendicular to x-y plane ($\hat{y}\times\hat{x}$), is modeled as

$$v_z(r) = v_{z0} + r\nabla V_p,$$

where v_{z0} is the initial LSR velocity and ∇V_p is the projected velocity gradient. To clarify, Fig. 4.16 shows a sketch of the outflow model.

The projected sizes of the outflows range from 0.7 to 3.7 pc with an average value of 2.0 pc. The projected speed gradients range between 0.26 and 3.7 $\mathrm{km\,s^{-1}\,pc^{-1}}$, with an average value of 1.7 $\mathrm{km\,s^{-1}\,pc^{-1}}$.

Masses of outflows are estimated by integrating their observed emission and using Eq. 4.3. Masses range between 18 and 1.9×10^2 $M_\odot$ with an average value of 10^2 $M_\odot$.

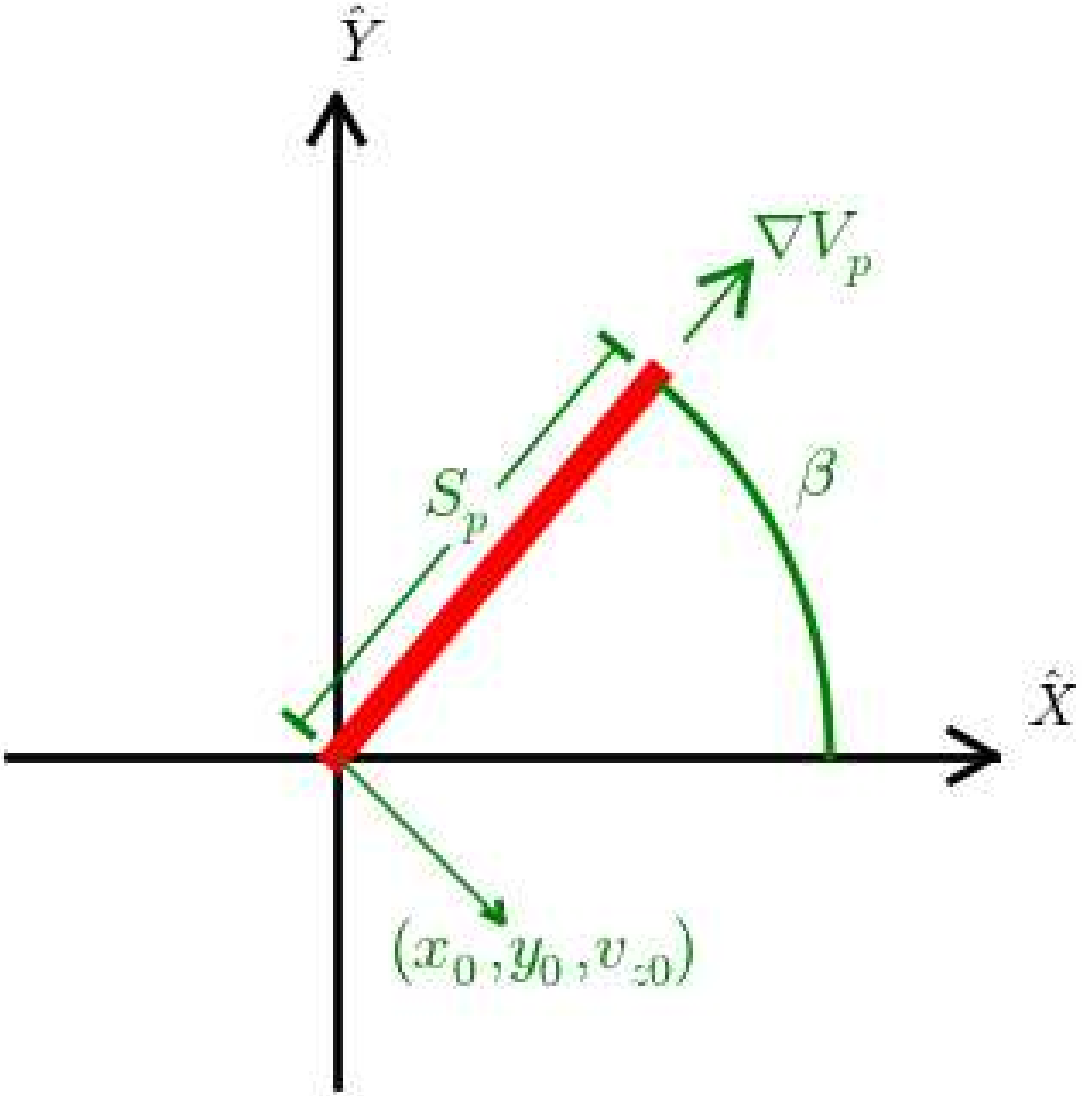

Figure 4.16: Sketch of the outflow model. The model is shown with β = 50 deg.

To estimate energies, we integrate the differential element of mass from Eq. 4.3 as

$$E_p = \frac{1}{2}\int dM(\Omega, v)(v - v_{z0})^2 dv d\Omega,$$

where E_p is a "projected energy", because it is estimated with the velocity projected in the z axis. Projected energies vary between 7.5×10^{44} and 2.8×10^{46} erg with an average value of 8×10^{45} erg.

Considering that the projected flow velocity at the head of the outflow (r=S_p) has remained constant in time, we estimate expanding times for outflows, t, as

$$t = \frac{1}{|\nabla V_p|}.$$

Expanding times range between 2.6×10^5 and 3.8×10^6 yr, with an average value of 7×10^5 yr.

Comparing with MSX and SPITZER data, we have identified infrared sources good candidates to drive tree of the observed molecular outflows. Figures 4.17 and 4.18 show SPITZER images for each outflow.

Mass outflow rates, $\dot{M}$, are estimated by

$$\dot{M} = \frac{M_{outflow}}{t},$$

where $M_{outflow}$ is the outflow mass. We estimate $\dot{M}$ between 3×10^{-5} and 4×10^{-4} $M_\odot$ yr^{-1} with an average value of 2×10^{-4} $M_\odot$ yr^{-1}. Comparing $\dot{M}$ estimated by Shepherd & Churchwell (1996), and assuming that detected molecular outflows are formed in the star formation process, possible motor sources have luminosities between 10 and 10^3 $L_\odot$.

We will propose ALMA observations toward this outflows to study their morphologies and kinematics with a higher resolution.

Table 4.5 shows the characteristics estimated for each outflow.

Table 4.5: Characteristics of the 5 outflows found. Column 1 shows outflow names; Columns 2 and 3, equatorial coordinates of the spatial centers; Column 4, initial LSR velocities ; Column 5, projected spatial sizes; Column 6, projected velocity gradients; Column 7, directions of ejections; Column 8, expansion times; Column 9, projected energies; Column 10, mass outflow rates; and Column 11, infrared sources that are good candidates to drive the outflow.

Outflow name	Spatial center (J2000)		v_{z0}	S_p	∇V	β	t	Mass	E_p	$\dot{M}$	Possible motor source
	RA	DEC	km s^{-1}	pc	km s^{-1} pc^{-1}	deg	yr	M$_\odot$	erg	$M_\odot$yr^{-1}	
1	16:58:56	-40:10:18	-11.6	1.6	-0.9	55	1.1×10^{6}	45	7.5×10^{44}	4×10^{-5}	G345.3133+01.4688
2	16:59:39	-40:08:29	-12.4	1.2	-3.7	58	2.6×10^{5}	10^{2}	1.9×10^{45}	4×10^{-4}	G345.4166+01.4092
3	16:59:35	-40:06:59	-16.7	3.7	0.26	161	3.8×10^{6}	1.7×10^{2}	3.2×10^{45}	4×10^{-5}	G345.4460+01.4389 G345.4496+01.4457
4	16:59:18	-40:01:11	-13.3	0.7	1.5	173	6.6×10^{5}	18	4.6×10^{45}	3×10^{-5}	-
5	16:59:27	-39:58:52	-11.9	2.8	-2.2	31	4.5×10^{5}	1.9×10^{2}	2.8×10^{46}	4×10^{-4}	-
Average values				2.0	[1]1.7		10^{6}	10^{2}	8×10^{45}	2×10^{-4}	

[1] Average gradient speed.

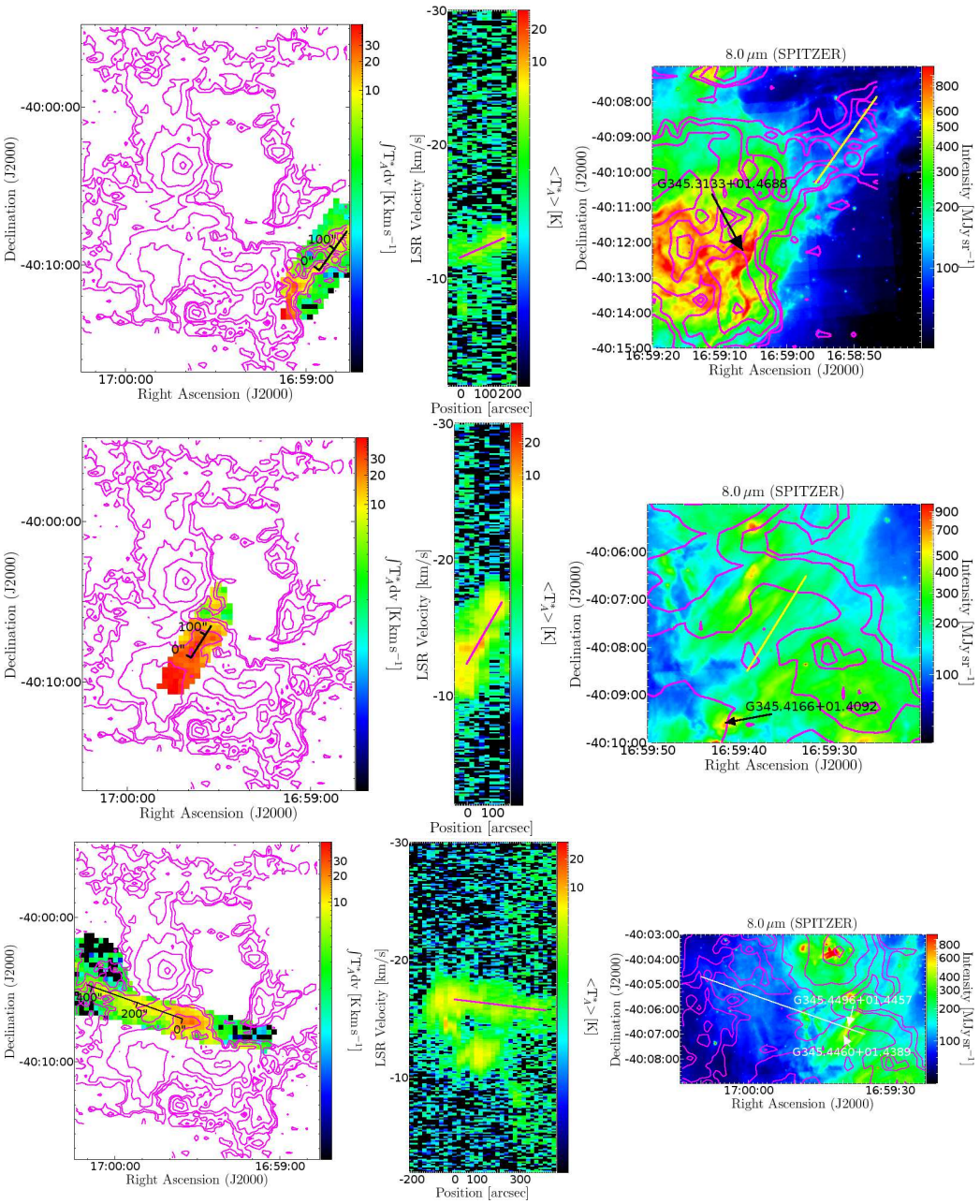

Figure 4.17: Observations toward the three southern outflows: above, toward the outflow 1; middle, toward the outflow 2; bottom, toward the outflow 3. Left images show the ^{13}CO(3-2) line emission integrated between -14 and −10 km s^{-1} for the outflow 1, between -20 and -10 km s^{-1} for the outflow 2, and between -20 and -14 km s^{-1} for the outflow 3. Middle images show the position-velocity diagrams of the average ^{13}CO(3-2) line emission following the fitted spatial distributions of the outflows displayed in the left images (black lines). Magenta lines show the fitted position-velocity distributions of the outflows. Right images show the 8 μm emission from SPITZER data. Arrows mark the position of MSX sources good candidates to drive the outflows. Lines indicate the fitted spatial distributions of the outflows. In the left and right images, contours display the ^{13}CO(3-2) line emission integrated between -30 and -2 km s^{-1} (levels: 5.4, 9.0, 18, 36, 72 and 144 K km s^{-1}).

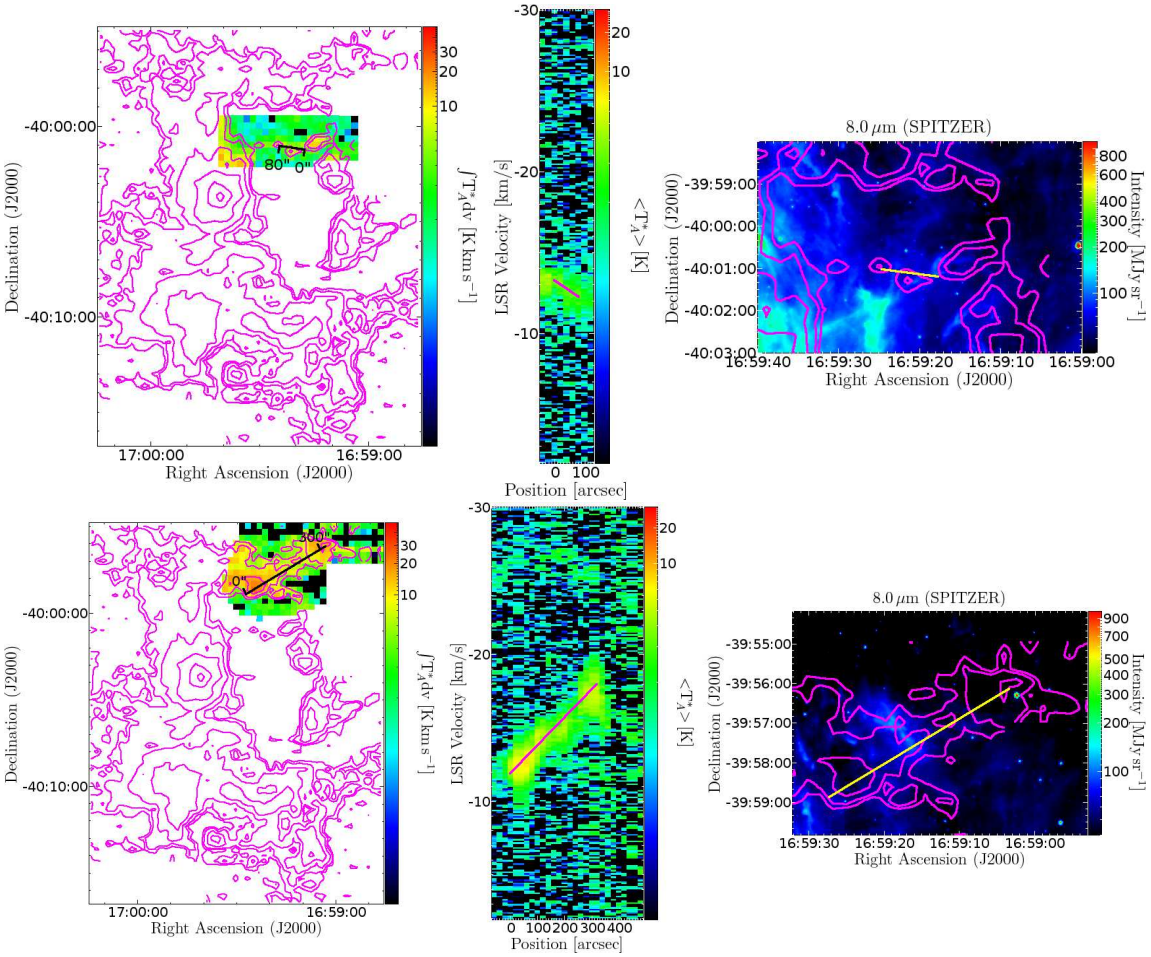

Figure 4.18: Observations toward the two northern outflows: above, toward the outflow 4; bottom, toward the outflow 5. Left images show the ^{13}CO(3-2) line emission integrated between -14 and -11 km s^{-1} for the outflow 4, and between -20 and -10 km s^{-1} for the outflow 5. Middle images show the position-velocity diagrams of the average ^{13}CO(3-2) line emission following the fitted spatial distributions of the outflows displayed in the left images (black lines). Magenta lines show the fitted position-velocity distributions of the outflows. Right images show the 8 μm emission from SPITZER data. Lines indicate the fitted spatial distributions of the outflows. In the left and right images, contours display the ^{13}CO(3-2) line emission integrated between -30 and -2 km s^{-1} (levels: 5.4, 9.0, 18, 36, 72 and 144 K km s^{-1}).

Chapter 5

Summary

5.1 Massive star formation in the GMC G345.5+1.0: Spatial distribution of the dust emission

We have robustly detected the whole of the GMC G345.5+1.0 in 1.2 mm continuum emission at a spatial resolution of 0.2 pc, and conclude that:

- The GMC is fragmented. We have identified 201 clumps, which have beam-corrected diameters between 0.2 and 0.6 pc, masses between 3.0 and 1.3×10^3 $M_\odot$, and densities between 5×10^3 and 4×10^5 cm^{-3}.

- The total mass of the clumps is $\sim1.2\times10^4$ $M_\odot$, and after comparing with the total mass of the GMC of $\sim6.5\times10^5$ $M_\odot$, we inferred that the efficiency in forming these clumps is ~0.02.

- The clump mass distribution is well-fitted by a power law $dN/dM \propto M^{-\alpha}$, where the spectral mass index α is 1.7±0.1. The total mass is dominated by massive clumps,

but the population is dominated by clumps with low masses.

- The spectral mass index of the clump mass distribution is different from that of the stellar IMF. Thus our detected clumps are probably not the direct progenitors of single stars.

- Comparing with MSX and SPITZER (IRAC-bands) observations, 20% of the clumps have an infrared counterpart in all MSX and SPITZER bands. The remaining clumps, ~80%, are considered to have no counterpart at infrared wavelengths. The percentage of detection is a lower limit to the number of clumps forming stars, while the percentage of no detections is an upper limit to the number of clumps that are not forming stars.

- Regions of massive-star formation within the cloud, associated with IRAS point sources, have SEDs that can be modeled with two dust components at different mean temperatures of 28±5 and 200±10 K.

5.2 G345.45+1.50: An expanding ring-like structure with massive star formation

We observed the ring G345.45+1.50 in the ^{13}CO(3-2) line, and conclude that:

- The ring contains a total mass of 6.9×10^3 $M_\odot$, in agreement with previous observations in 1.2 mm continuum emission.

- The ratio of the column density estimated from the 1.2 mm continuum emission to that estimated from the ^{13}CO(3-2) line varies between 0.1 and 10, with an averaged value of ~1.0. The column density estimated from the 1.2 mm continuum emission

is higher than that estimated from the ^{13}CO(3-2) line toward sites with high density. It is possible that the 1.2 mm continuum emission is more optically thin than the ^{13}CO(3-2) line toward dense regions.

- The ring is expanding with a velocity of 1.4 km s^{-1}, and has an expansion time scale of 2.4×10^{6} yr and a total energy of 1.4×10^{47} erg. This expansion could be produced by a supernova explosion. This hypothesis is supported by the presence of a 35.6 cm source, J165920-400424, near to the center of the ring, ∼90 arcsec, without an infrared counterpart. This source can be a pulsar, resulting from the gravitational collapse of a massive star.

- From the ^{13}CO(3-2) line, we identify 57 clumps with diameters between 0.3 and 1.0 pc, masses between 7.4 and 8.6×10^{2} M$_{\odot}$, and densities between 2×10^{3} and 5×10^{4} cm^{-3}.

- Assuming that clumps can be modeled as Bonnor-Ebert spheres, the clumps require an averaged external pressures of 7×10^{6} K cm^{-3} to be in hydrostatic equilibrium.

- In the region, we identify 5 outflows with projected sizes between 0.3 and 1.4 pc, the projected speed gradients between 0.26 and 3.7 km s^{-1} pc^{-1}, and projected energies between 7.5×10^{44} and 2.8×10^{46} erg. We have identified infrared sources good candidates to drive three of the observed molecular outflows.

Appendix A

LTE column density estimated from the ^{13}CO(3-2) line

Considering the rotational transition of a linear molecule from the upper level “u” to the lower level “l”, the column density of the lower level is (Wilson, Rohlfs & Hüttemeister 2009):

$$N_l = 93.5\, cm^{-2}\, \frac{g_l(\nu/GHz)^3}{g_\mu(A_{\mu l}/s^{-1})}\, \frac{1}{1-exp(h\nu/k\,T_K)} \int \tau(dv/km\,s^{-1}),$$

where T_{ex} is the excitation temperature, which is approximated to the kinematic temperature T_K, ν is the frequency of transition, τ is the optical depth, A_{mul} is the Einstein A coefficient between the transition of the upper and lower levels, v is de Doppler velocity, g_l and g_μ are the statistical weights of the states. Assuming that $h\nu/k << T_K$, $\tau << 1$ and the source observed fills the main beam, we approximate $T_K\,\tau \sim T_{MB} \sim T_b$, where T_{MB} is the main beam brightness temperature, and T_b is the brightness temperature. Thus

$$N_l = 93.5\, cm^{-2}\, \frac{g_l(\nu/GHz)^3}{g_\mu(A_{\mu l}/s^{-1})}\, \frac{1}{1-exp(h\,\nu/k\,T_K)}\, \frac{1}{T_K} \int T_b(dv/km\,s^{-1}).$$

Assuming that all energy levels are populated under LTE conditions, i.e, under an equilibrium of the radiation with its surrounding, the fraction of the total population in a

particular state, J, is given by:

$$N(J)/N(total) \sim (2J+1)\exp\left(-\frac{hB_eJ(J+1)}{kT_K}\right)\frac{h\,B_e}{k\,T_K},$$

for $h\,B_e << k\,T_K$, where B_e is the rotation constant. Thus, the total density is given by

$$N(total) = 93.5\,cm^{-2}\,\frac{g_l}{g_u}\frac{(\nu/GHz)^3}{(A_{ul}/s^{-1})}\frac{k}{hB_e}\frac{1}{2J+1}\exp\left(\frac{hBe}{k}\frac{J(J+1)}{T_K}\right)\frac{1}{1-\exp(h\,\nu/k\,T_K)}\int T_B(dv/km\,s^{-1}).$$

For the emission transition J+1 to J, $A_{\mu l}$ is given by:

$$A_{\mu l} = A_J = 1.165\times10^{-11}\,s^{-1}(\mu/Debyes)^2(\nu/GHz)^3\frac{J+1}{2J+3},$$

$g_l = 2J+1$ and $g_u = 2J+3$. Thus

$$N(total) = 80.3\times10^{11}\,cm^{-2}\,\frac{1}{(\mu/Debyes)^2}\frac{k}{hB_e}\frac{1}{J+1}\exp\left(\frac{hBe}{k}\frac{J(J+1)}{T_K}\right)\frac{1}{1-\exp(h\,\nu/k\,T_K)}\int T_B(dv/km\,s^{-1}).$$

The ^{13}CO(3-2) line has a transition at 330.587960 GHz, with B_e=5.5101×10^4 MHz and μ=0.11046 Debyes (http://www.splatalogue.net/). Thus the total column density from this transition is:

$$N(total) = 8.30\times10^{13}\,cm^{-2}\frac{\exp(15.9\,K/T_K)}{1-\exp(-15.9\,K\,T_K)}\int T_B(dv/km\,s^{-1}).$$

Bibliography

Alvarez, H., May, J., & Bronfman, L. 1990, ApJ, 348, 495.

Bains, I., Wong, T., Cunningham, M. et al. 2006, MNRAS, 367, 1609.

Ballesteros-Paredes, J., Gazol, A., Kim, J. et al. 2006, ApJ, 637, 384.

Ballesteros-Paredes, J., Klessen, R. S., Mac Low, M.-M. & Vázquez-Semadeni, E. 2007, Protostars and Planets V, p. 63. Edited by Reipurth, B., Jewitt, D. & Keil, K. Published by University of Arizona Press.

Beltrán, M. T., Brand, J., Cesaroni, R. et al. 2006, A&A, 447, 221.

Benjamin, R. A., Churchwell, E., Babler, B. L. et al. 2003, PASP, 115, 953.

Bertoldi, F. & McKee, C. F. 1992, ApJ, 395, 140.

Blitz, L. 1993, Protostars and Planets III, p125. Edited by Levy, E. & Lunine, J. I. Published by University of Arizona Press.

Bohlin, R. C., Savage, B. D., & Drake, J. F. 1978, ApJ, 224, 132.

Bonnell, I. A., Larson, R. B., & Zinnecker, H. 2007, Protostars and Planets V, p. 149. Edited by Reipurth, B., Jewitt, D. & Keil, K. Published by University of Arizona Press.

Bonnor, W. B. 1956, MNRAS, 116, 351.

Bronfman, L., Alvarez, H., Cohen, R. S., & Thaddeus, P. 1989, ApJ, 71, 481.

Bronfman, L., Nyman, L.-Å., & May, J. 1996, A&A, 115, 81.

Bronfman, L., Casassus, S., May, J., & Nyman, L.-Å. 2000, A&A, 358, 521.

Chavarría, L. A., Allen, L. E., Hora, J. L., Brunt, C. M., & Fazio, G. G. 2008, ApJ, 682, 445.

Churchwell, E. 2008, ASPC, 390, 63.

Dame, T. M., Elmegreen, B. G., Cohen, R. S., & Thaddeus, P. 1986, ApJ, 305, 892.

Draine, B. T., & Lee, H. M. 1984, ApJ, 285, 89.

Evans, N. J. 1999, ARA&A, 37, 311.

Faúndez, S., Bronfman, L., Garay, G. et al. 2004, A&A, 426, 97.

Fazio, G. G., Hora, J. L., Allen, L. E. et al. 2004, ApJS, 154, 10.

Frerking, M. A., Langer, W. D., & Wilson, R. W. 1982, ApJ, 262, 590.

Garay, G., Faúndez, S., Mardones, D. et al. 2004, ApJ, 610, 313.

Grabelsky, D. A., Cohen, R. S., Bronfman, L., & Thaddeus, P. 1988, ApJ, 331, 181.

Güsten, R., Nyman, L.-Å., Shilke, P., Menten, K., Cesarsky, C., & Booth, R. 2006, A&A, 454, 13.

Heiles, C. 1979, ApJ, 229, 533.

Hildebrand, R. H. 1983, QJRAS, 24, 267.

Hill, T., Burton, M. G., Minier, V. et al. 2005, MNRAS, 363, 405.

Hunter, S. D., Bertsch, D. L., Catelli, J. R. et al. 1997, ApJ, 481, 205.

Kandori, R., Nakajima, Y., Tamura, M. et al. 2005, AJ, 130, 2166.

Klessen, R. S., Burkert, A., & Bate, M. R. 1998, ApJ, 501, 205.

Kroupa, P. 2002, Science, 295, 82.

Lada, C. J., Alves, J. F., & Lombardi, M. 2007, Protostars and Planets V, p. 3. Edited by Reipurth, B., Jewitt, D. & Keil, K. Published by University of Arizona Press.

Li, Y., Mac Low, M.-M., & Klessen, R.S. 2005, ApJ, 626, 823.

Lumsden, S. L., Hoare, M. G., Oudmaijer, R. D., & Richards, D. 2002, MNRAS, 336, 621.

Martín-Pintado, J., Gaume, R. A., Rodríguez-Fernández, N., et al. 1999, ApJ, 519, 667.

Molinari, S., Brand, J., Cesaroni, R., & Palla, F. 2000, A&A, 355, 617.

Molinari, S., Pezzuto, S., Cesaroni, R. et al. 2008, A&A, 481, 345.

Morales, E. F. E., Mardones, D., Garay, G. et al. 2009, ApJ, 698, 488.

Mookerjea, B., Kramer, C., Nielbock, M., & Nyman, L.-Å. 2004, A&A, 426, 119.

Motte, F., André, P., & Neri, R. 1998, A&A, 336, 150.

Motte, F., Bontemps, S., Schilke, P. et al. 2007, A&A, 476, 1243.

Muñoz, D.J., Mardones, D., Garay, G., & Rebolledo, D. 2007, ApJ, 668, 906.

Murphy, T., Mauch, T., Green, A. et al. 2007, MNRAS, 382, 382.

Nutter, D., & Ward-Thompson, D. 2007, MNRAS, 374, 1413.

Oka, T., Hasegawa, T., Sato, F., et al. 1998, ApJS, 118, 455.

Ossenkopf, V., & Henning, Th. 1994, A&A, 291, 943.

Panagia, N. 1973, ApJ, 78, 929.

Sanders, D. B., Scoville, N. Z., & Solomon, P. M. 1985, ApJ, 289, 373.

Solomon, P. M., Rivolo, A. R., Barrett, J., & Yahil, A. 1987, ApJ, 319, 730.

Schuller, F., Menten, K. M., Contreras, Y. et al. 2009, A&A, 504, 415.

Shepherd, D. S., & Churchwell, E. 1996, ApJ, 472, 225.

Tenorio-Table, G., & Bodenheimer, P. 1988, ARA&A, 26, 145.

van Dishoeck 2004, ARA&A, 42, 119.

Whiteoak, J. B. Z. 1992, A&A, 262, 251.

Williams, J. P., De Geus, E. J., & Blitz, L. 1994, ApJ, 428, 693.

Williams, J. P., & McKee, C. F. 1997, ApJ, 476, 166.

Williams, J. P., Blitz, L., & McKee, C. F. 2000, Protostars and Planets IV, p 97. Edited by Mannings, V., Boss, A. P., & Russell, S. S. Published by University of Arizona Press.

Wilson, T. L., Rohlfs, K. & Hüttemeister, S. 2009, Tools of Radio Astronomy, Fifth Edition. Edited by G. Börger, A. Burkert, W. B. Burton et al. Published by Springer-Verlag, Berlin, Germany.

Wong, T., Ladd, E. F., Brisbin, D. et al. 2008, MNRAS, 386, 1069.

Wood, D. O. S., & Churchwell, E. 1989, ApJ, 340, 265.

Zinnecker, H. & York, H. 2007, ARA&A, 45, 481.